E.O. Paton Electric Welding Institute of the National Academy of Science of Ukraine
International Association «Welding»
LLC «Scientific Journals»

The Paton Welding Journal

04
2022

International Scientific-Technical and Production Journal ◊ Founded in January 2000 (12 Issues Per Year)

Address of Editorial Board
E.O. Paton Electric Welding Institute, 11 Kazymyr Malevych Str. (former Bozhenko), 03150, Kyiv, Ukraine
Tel./Fax: (38044) 205 23 90, E-mail: journal@paton.kiev.ua
https://patonpublishinghouse.com/eng/journals/tpwj

State Registration Certificate 24933-14873 ПР from 13.08.2021
ISSN 0957-798X, DOI: http://dx.doi.org/10.37434/tpwj

Subscriptions, 12 issues per year:
$384 — annual subscription for the printed (hard copy) version, air postage and packaging included;
$312 — annual subscription for the electronic version (sending issues in pdf format or providing access to IP addresses).

Representative Office of «The Paton Welding Journal» in China:
China-Ukraine Institute of Welding, Guangdong Academy of Sciences
Address: Room 210, No. 363 Changxing Road, Tianhe, Guangzhou, 510650, China.
Zhang Yupeng, Tel: +86-20-61086791, E-mail: patonjournal@gwi.gd.cn

The content of the journal includes articles received from authors from around the world in the field of welding, metallurgy, material science and selectively includes translations into English of articles from the following journals, published by PWI in Ukrainian:
- Automatic Welding (https://patonpublishinghouse.com/eng/journals/as);
- Technical Diagnostics & Nondestructive Testing (https://patonpublishinghouse.com/eng/journals/tdnk);
- Electrometallurgy Today (https://patonpublishinghouse.com/eng/journals/sem).

CONTENTS

ORIGINAL ARTICLES

*Translated Article(s) from «Automatic Welding», No. 4, 2022.

**Translated Article(s) from «Electrometallurgy Today», No. 1. 2022.

***Translated Article(s) from «Technical Diagnostics & Nondestructive Testing», No. 1, 2022.

https://doi.org/10.37434/tpwj2022.04.01

ELECTRODYNAMIC TREATMENT OF WELDED JOINTS OF ALUMINIUM AMg6 ALLOY IN THE PROCESS OF HEATING THE WELD METAL

L.M. Lobanov[1], **M.O. Pashchyn**[1], **O.L. Mikhodui**[1], **P.V. Goncharov**[1], **A.V. Zavdoveev**[1], **P.R. Ustymenko**[2]

[1]E.O. Paton Electric Welding Institute of the NASU
11 Kazymyr Malevych Str., 03150, Kyiv, Ukraine
[2]National Technical University of Ukraine «Igor Sikorsky Kyiv Polytechnic Institute»
37 Peremohy Ave., 03056, Kyiv, Ukraine

ABSTRACT

The effect of thermal action in the process of electrodynamic treatment (EDT) of welded joints of AMg6 alloy on their stress-strain states was investigated. Based on the Prandtl–Reuss ratio for the movement of elastic-plastic environment at elevated temperatures, a mathematical model of evaluation of stress state of metal materials as a result of their interaction with the electrode-indenter at EDT was developed. On the basis of the developed model, a calculated evaluation of the effect of elevated temperatures on residual stresses of a preliminary strained plate of AMg6 alloy as a result of EDT was carried out. The verification of the results of the calculation with the use of welded plates of AMg6 alloy of 2 mm thickness was carried out. Thermal action was carried out with the help of the accompanying EDT preheating of the weld metal. To evaluate the effect of the thermal potential of EDT on residual stresses, TIG welding of butt joint specimens was performed. EDT of specimens at the temperature T_{EDT} = 20 and 100 °C was performed. Applying the method of electron speckle-interferometry, the values of the longitudinal component (along the longitudinal axis of the weld) of residual welding stresses in the central cross-section of the specimens before and after EDT were measured. The thermal impact on EDT was provided with the use of a heat gun, and the heating temperature was controlled by an infrared thermometer. It was revealed that heating of the weld in the process of its EDT along the longitudinal axis of a butt joint provides greater values of residual compressive stresses in the weld centre as compared to the treatment at T = 20 °C.

KEYWORDS: electrodynamic treatment, welded joints, accompanying heating, residual welding stresses, aluminium alloys

INTRODUCTION

The use of energy of pulsed electromagnetic fields (PEMF) for regulating residual stresses in the technologies for treatment of structural materials is relevant for the modern industry. One of such methods, characterized by energy efficiency and ease of realization, is electrodynamic treatment (EDT) of welded joints [1].

The modern trend in engineering practice is the study of measures aimed at improving the efficiency of EDT. One of them is the combination of the EDT process with preheating of the treatment zone. Scientific principles of using thermal potential at EDT are based on the results of the work [2], where it is shown that heating of preliminary tensioned thin rods of low-carbon steel facilitates an increase in the efficiency of their treatment by PEMF to reduce the level of residual stresses. Considering that EDT efficiency is determined by an electric pulsed component of electrodynamic action [3], the thermal action can intensify mechanisms of relaxation of residual welding stresses. This should have a positive effect on regulation of stress-strain states of metals, alloys and welded joints during their EDT.

The aim of the work is to study the effect of preheating the weld metal in the process of EDT on residual stresses of welded joints of aluminium AMg6 alloy.

According to the results of studies with the use of EDT of preliminary loaded plane specimens of aluminium AMg6 alloy applying longitudinal tension σ_x, it was found that the maximum indices of treatment efficiency were achieved at a value of σ_x, which is close to the yield strength $\sigma_{0.2}$ of the metal [4]. As an efficiency criterion, a discrete decrease in the tensile stresses σ_x of the specimen as a result of EDT was taken. Under the conditions, where the stresses σ_x did not reach or exceeded the level $\sigma_{0.2}$, a decrease in EDT efficiency as compared to the treatment of the specimen at $\sigma_x = \sigma_{0.2}$ was determined. The presence of residual tensile stresses in the active zone of the welded joint of AMg6 alloy, which is close to $\sigma_{0.2}$, creates the preconditions for effective use of EDT to relax the latter [1]. Investigations of stress states of welded joints of AMg6 alloy after EDT at different T_{EDT} allowed evaluating thermal potential as an increase in treatment efficiency factor.

MODELING OF STRESS STATES IN THE PLATES OF AMg6 ALLOY FROM THE IMPACT ACTION OF THE ELECTRODE-INDENTER AT EDT IN THE CONDITIONS OF THEIR HEATING

Taken into account the abovementioned, it should be noted that EDT with a compatible heating of the treatment zone can be effective as compared to EDT with-

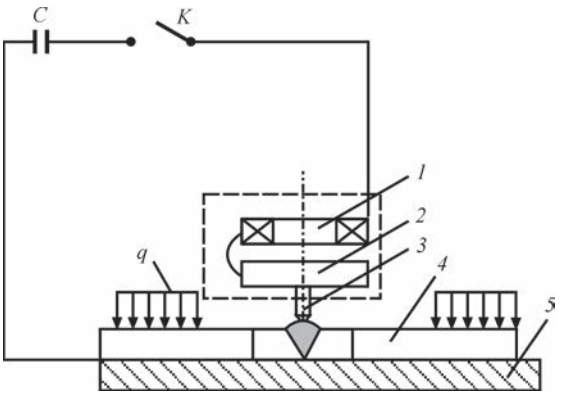

Figure 1. Scheme of EDT of plates: *1* — inductor; *2* — disc; *3* — movable electrode-indenter; *4* — specimen being treated; *5* — working table; *q* — load fixing the specimen [5]

out heating to reduce residual welding stresses. The search for the optimal EDT mode is associated with an experimental evaluation of a large number of process parameters. An alternative solution is the mathematical modeling of the EDT process, which allows evaluating the change in the stress-strain state of welded joints after the treatment in the conditions of elevated temperatures that have not been conducted so far.

On the basis of the work [5], mathematical modeling of the effect of temperature T_{EDT} was carried out on the stress states of welded plates of aluminium AMg6 alloy as a result of the impact action of the electrode-indenter. The creation of dynamic pressure on the surfaces of EDT-treated plates was carried out according to the scheme (Figure 1). The EDT-treated specimen *4* in the form of a welded plate is located on the working table *5*. After starting the contactor *K* of the discharge cycle of the capacitance *C* on the inductor *1*, the latter generates a magnetic field of appropriate power, under the action of which the disc *2* of nonferromagnetic material together with the electrode-indenter *3* obtain different values of the initial speed V_0 in the direction of the working table *5*. The values V_0 were found on the basis of previous studies. The impact interaction of the EDT electrode-indenter with the surface of the plates leads to the formation of

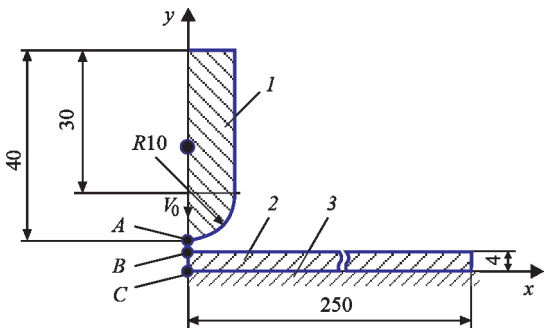

Figure 2. Design scheme of the process of dynamic loading of EDT-treated plates: *1* — electrode-indenter; *2* — specimen being treated; *3* — absolutely rigid base; *A* is the point on the outer surface of the electrode-indenter; *B* is the point on the outer surface of the plate; *C* is the point on the back surface of the plate [5]

different levels of residual stresses and strains in them depending on the value V_0.

Creation of a mathematical model of the dynamic component of EDT in the conditions of elevated temperatures was carried out using a simplified two-dimensional (2D) plane production. The design scheme of the problem of the process of impact interaction of the electrode-indenter with the plates [5, 6] is presented in Figure 2. The presence of the abovementioned geometric symmetry of the bodies being in impact interaction allows considering only half of their cross-section with the simultaneous imposition of appropriate boundary conditions on it. These conditions include the imposition of a ban on the movement of nodes of a finite element mesh (FEM) of the bodies, located on the axis of the symmetry, in the horizontal direction "*X*". The presence of the plates of the working table 5 in the scheme of electrodynamic treatment (Figure 1) is advisable to be replaced with resting on an absolutely rigid base *3* (Figure 2), which in the mathematical definition will be equivalent to the imposition of a ban on moving in the vertical direction "*Y*" of the FEM nodes, belonging to the lower surface of the plate contacting the working table.

For numerical modeling, a continuum model of the environment was used. This made it possible to record the laws of conservation of mass, quantity of movement and energy in the form of differential equations in partial derivatives [5]. In the mathematical definition, the behaviour of materials of the plate (aluminium AMg6 alloy) and electrode-indenter (copper M1) under the action of external pulse load was described using the ideal elastic-plastic rheological model of the material, which in the library of materials of the program ANSYS/LS-DYNA is called "PLASTIC-KINEMATIC". The effect of elevated (above the room) temperatures T_{EDT} was set by the values of the modulus of elasticity *E* and the yield strength $\sigma_{0.2}$ at T_{EDT} = 20 and 100 °C.

Residual welding stresses were modeled by setting the longitudinal (along the axis *X* in Figure 2) component of tensile stresses σ_x, the values of which were taken equal to $\sigma_{0.2}$ of AMg6 alloy at appropriate temperatures. The normal contact interaction of the hemispherical cylindrical electrode-indenter of 15 mm diameter (diameter of the sphere is 30 mm) weighing 102.5 g of copper M1 alloy with a plate of AMg6 alloy of 250×250×2 mm was modelled. The mechanical characteristics of the plate and indenter, being in a contact interaction, are given in Table 1. The electrode-indenter receives the value V_0 = 5 m/s, which was determined on the basis of the previous studies [5]. The final calculated distribution of residual stresses σ_x component in the plates was determined along the impact line (direction V_0 in Figure 2).

Figure 3 shows the results of modeling the residual distributions of a longitudinal (along the weld) component of stresses σ_x along the impact line in the plates $\delta = 2$ mm. It can be seen that the compressive stresses σ_x along the impact line on the contact and reverse surfaces of the plates reach 0.3 σ_y of AMg6 alloy at $T = 20$ °C (*α*) and are close to σ_y at $T = 100$ °C (*b*).

EQUIPMENT AND PROCEDURE OF EXPERIMENTAL INVESTIGATIONS

In order to verify the results of mathematical modeling, EDT of the specimens of butt welded joints the size of 250×250×2 mm with a central weld was carried out. Before welding, the specimens were rigidly fixed on the assembly table by clamping straps along the longitudinal welded edges at a distance of 20 mm from them according to the scheme in Figure 1. Welded joints were produced by automatic TIG welding at the values of voltage, current and speed of the process, respectively, $U_a = 20.1$ V, $I_a = 115$ A and $v_w = 5$ mm/s. As an additive, the wire of grade ER5356 ESAB with a diameter of 1.6 mm, fed into the arc zone at a rate $v_{wf} = 33$ mm/s was used.

After welding and complete cooling of the specimens by the method of electron speckle-interferometry [7] before and after EDT, the values σ_x of residual welding stresses in the weld centre, along the fusion line and at a distance of 10 mm from the weld centre were determined.

EDT of specimens in manual mode at the charge voltage and capacitance of the capacitor, respectively $U_w = 500$ V and $C = 5140$ μF, was carried out along the longitudinal axis of the weld (Figure 4).

At the first stage of the studies, the evaluation of the initial residual stress state of the welded plate No. 1 was performed, which was subsequently subjected to EDT at $T_{EDT} = 20$ °C. At the second stage after evaluation of the initial residual stress state of the plate No. 2, it was subjected to EDT at $T_{EDT} = 100$ °C.

The thermal effect on the specimens was performed by the technological heat gun BOSCH 660 LCD and the temperature T_{EDT} was controlled by the infrared thermometer GT-810. The EDT scheme in the conditions of accompanying heating is shown in Figure 4, *a*, the process of EDT and the treatment zone of welded joints at $T_{EDT} = 100$ °C are respectively in Figure 4, *b*, *c*.

Table 1. Mechanical characteristics of plate of AMg6 alloy and indenter of M1 alloy

Number	Material	*T*, °C	Density ρ, kg/m³	Modulus of elasticity *E*, GPa	Poisson's ratio μ	Yield strength $\sigma_{0.2}$, MPa
1	AMg6	20	2640	71	0,34	150
2	AMg6	100	2640	65	0,34	130
3	M1	20	8940	128	0,35	300

DISCUSSION OF THE EXPERIMENTAL RESULTS

The distribution of σ_x in the central cross-section of the specimens of butt joints without EDT and after its application at $T_{EDT} = 20$ and 100 °C is shown in Figure 5. It can be seen that EDT has a positive effect on the distribution of stresses σ_x in the experimental specimens, changing them from tensile to compressive stresses in the weld centre and along the fusion line. Therefore, the peak values of tensile stresses σ_x in the initial state (before EDT) in the weld centre, along the fusion line and at a distance of 10 mm from the weld centre reached 60, 90 and 50 MPa (Figure 5, *a*).

After EDT at $T_{EDT} = 20$ °C (Figure 5, *b*), the stresses σ_x were transformed into compressive stresses, and their peak values in the weld centre, along the fusion line and at a distance of 10 mm from the weld centre reached –35, –25 and –5 MPa, respectively.

After EDT at $T_{EDT} = 100$ °C (Figure 5, *c*), the compressive stresses σ_x in the weld centre and along the fusion line did not exceed –80 and –1 MPa. At a distance of 10 mm from the weld centre, the tensile stresses σ_x reached 40 MPa, i.e., they did not change significantly as compared to the initial state, which can be seen when comparing columns *3*, respectively in Figure 5, *a*, *c*.

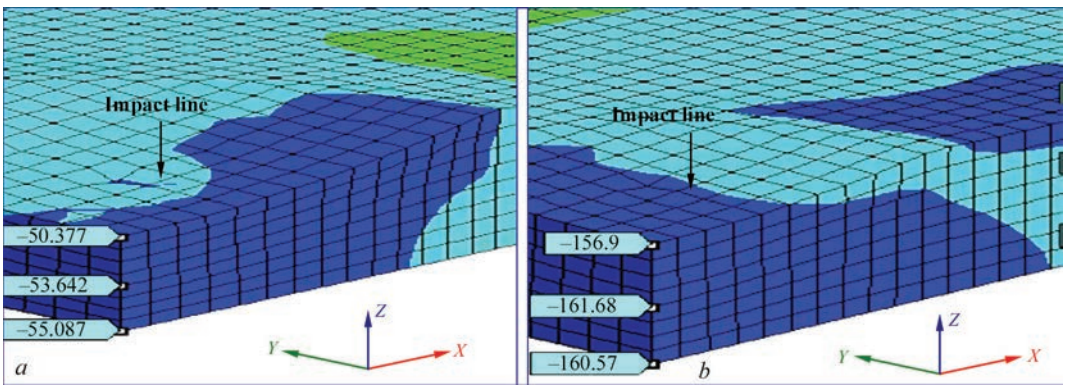

Figure 3. Final calculated distribution of residual stresses σ_x, MPa along the impact line in the plate from AMg6 alloy $\delta = 2$ mm after EDT at different values of T_{EDT}: *a* — 20; *b* — 100 °C

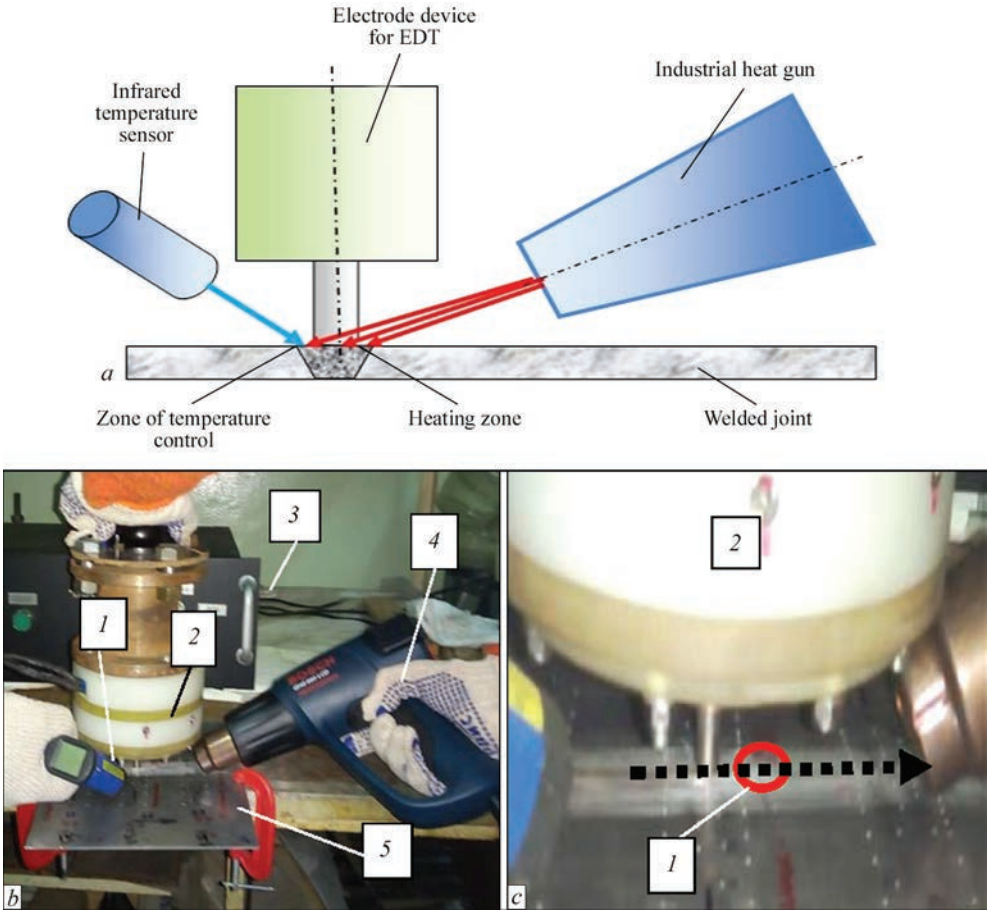

Figure 4. Procedure of verification of the effect of accompanying heating on the efficiency of EDT of welded joints: *a* — scheme of investigations; *b* — EDT process of welded joints in the conditions of elevated temperature (*1* — temperature sensor; *2* — electrode device for EDT; *3* — EDT power supply; *4* — industrial heat gun; *5* — welded joint specimen); *c* — location of the electrode device *2* relative to the treatment zone *1*, where the arrow indicates the direction of treatment along the weld line

Based on the abovementioned, it can be noted that preheating of the weld metal in the process of EDT contributes to an increase in the gradient of σ_x distribution in the cross-section of the specimen and a growth in values of the compressive stresses σ_x in the weld centre (column 1 in Figure 5, *a–c*).

Heating of the weld to the temperature T_{EDT} = = 100 °C provides thermoelastic deformation $\varepsilon_т$ of the elongation of AMg6 alloy in the weld zone, at which the metal reaches the yield strength $\sigma_{0.2}$, the value of

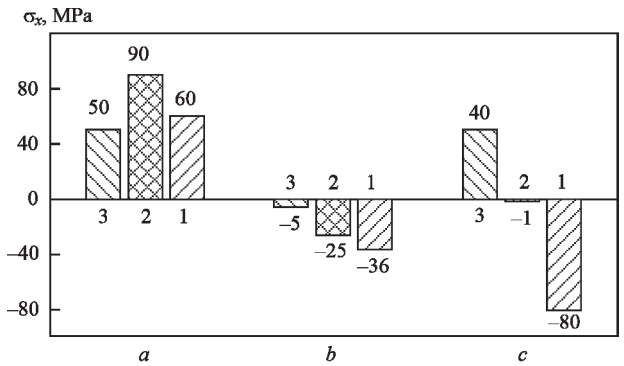

Figure 5. Distribution of σ_x in the central cross-section of the specimens of butt joints: *a* — without using EDT; *b* — after EDT at T_{EDT} = 20 °C; *c* — after EDT at T_{EDT} = 100 °C (*1* — weld centre; *2* — fusion line; *3* — at a distance of 10 mm from the weld centre)

which is lower than $\sigma_{0.2}$ at T_{EDT} = 20 °C. A decrease in $\sigma_{0.2}$ at T_{EDT} = 100 °C, causes a decrease in residual stresses due to an increase in plastic tensile deformation of the weld metal, which is the result of electroplastic deformation of the latter according to the mechanism shown in [1, 3, 4]. Also an increase in ductility of AMg6 alloy occurs during heating, which is characterized by an increase in the value of relative elongation δ respectively from 22 % at T_{EDT} = = 20 °C to 34 % at T_{EDT} = 100 °C [8]. This facilitates an increase in the density of electric contact of the pair "indenter-metal" at their interaction at T = 100 °C as compared to EDT at T_{EDT} = 20 °C. This results in a more intensive (as compared to EDT at T_{EDT} = 20 °C) plastic deformation of the metal in the contact zone due to the electroplastic effect [9]. This contributes to the formation of local plastic tensile deformations, resulting in an increase in the compressive stresses in the treatment zone.

The higher gradient of σ_x distribution under the heating conditions is confirmed by the comparison of $\Delta\sigma$ values at T_{EDT} = 150 and 20 °C. The value of $\Delta\sigma$ was determined as the absolute difference of stresses between the values of σ_x in the weld centre and

Table 2. Values of Δσ in the weld centre and along the fusion line of specimens of welded joints from AMg6 alloy

Number	T_{EDT}, °C	Δσ, MPa	
		Weld centre	Fusion line
1	20	95	115
2	100	140	91

along the fusion line of the specimens in the initial state (without EDT) and after the treatment at different T_{EDT}. The obtained values of Δσ in different areas of the weld at a variation of T_{EDT} are given in Table 2.

From the data in Table 2, it can be seen that EDT at T_{EDT} = 100 °C is more effective (as compared to EDT at T_{EDT} = 20 °C) to increase the level of compressive stresses in the weld centre. But for the fusion line, the opposite is true. Thus, EDT at elevated temperatures promotes an increase in the gradient of distribution of electrodynamic effect on the residual stress states of welded joints. Let us note that under cyclic loading, where the effect of residual stresses is more significant than under static one, the fracture of welded joints mostly takes place along the fusion line. Therefore, as the optimal scheme of EDT, the treatment along the fusion line at T_{EDT} = 150 °C should be considered, but this requires further investigations.

Taken into account the abovementioned, it should be noted that the thermal potential is one of the important factors in optimizing the stress states of welded joints of AMg6 alloy at EDT, but the optimization of the scheme and parameters of electrodynamic actions requires further investigations.

CONCLUSIONS

1. The rationality of using accompanying heating of a welded joint of AMg6 alloy during its electrodynamic treatment is substantiated. It is shown that thermal action in general has a positive effect on the efficiency of EDT of welded joints as compared to their treatment at a room temperature.

2. An experimental procedure was developed, on the basis of which investigations were conducted to evaluate the effect of EDT-compatible preheating of the treatment zone on the stress state of welded plates at EDT.

3. It was found that EDT of the welded joint centre in the conditions of its accompanying heating is more effective for regulating residual stresses in the weld centre and less effective along the fusion line as compared to EDT without preheating.

REFERENCES

1. Lobanov, L., Kondratenko, I., Zhiltsov, A. et al. (2018) Development of post-weld electrodynamic treatment using electric current pulses for control of stress-strain states and improvement of life of welded structures. *Mater. Performance and Characterization*, 7(**4**), 941–955. DOI: https://doi.org/10.1520/MPC20170092. ISSN 2379-1365.
2. Stepanov, G.V., Babutsky, A.I., Mameev, I.A. (2004) Nonstationary stress-strain state in long rod caused by pulses of high density electric current. *Problemy Prochnosti*, **4**, 60–67 [in Russian].
3. Lobanov, L.M., Pashin, N.A., Mikhodui, O.L., Sidorenko, Yu.M. (2018) Electric pulse component effect on the stress state of AMg6 aluminum alloy welded joints under electrodynamic treatment. *Strength of Materials*, *March*, 50(**2**), 246–253. DOI: https://doi.org/10.1007/s11223-018-9965-x
4. Lobanov, L.M., Pashin, N.A., Mikhodui, O.L. (2012) Influence of the loading conditions on the deformation resistance of AMg6 alloy during electrodynamic treatment. *Strength of Materials*, **44**, 472–479. DOI: https://doi.org/10.1007/s11223-012-9401-6
5. Lobanov, L.M., Pashin, N.A., Mikhodui, O.L., Sidorenko, Yu.M. (2017) Effect of the indenting electrode impact on the stress-strain state of an AMg6 alloy on electrodynamic treatment. *Strength of Materials*, May, 49(**3**), 369–380.
6. Lobanov, L.M., Pashchyn, M.O., Mikhodui, O.L. et al. (2021) Modeling of stress-strain states of AMg6 alloy due to impact action of electrode-indenter in electrodynamic treatment. *The Paton Welding J.*, **6**, 2–11. DOI: https://doi.org/10.37434/tpwj2021.06.01
7. Lobanov, L.M., Pashin, N.A., Mihoduy, O.L., Khokhlova, J.A. (2016) Investigation of residual stress in welded joints of heat-resistant magnesium alloy ML10 after electrodynamic treatment. *J. of Magnesium and Alloys*, **4**, 77–82.
8. Fridlyander, I.N. (1974) *Aluminium alloys: Structure and properties of semi-finished products from aluminium alloys.* Moscow, Metallurgiya [in Russian].
9. Strizhalo, V.A., Novogrudskyi, L.S., Vorobiov, E.V. (2008) *Strength of materials at cryogenic temperatures taking into account the impact of electromagnetic fields.* Kyiv, IPS [in Russian].

ORCID

L.M. Lobanov: 0000-0001-9296-2335,
M.O. Pashchyn: 0000-0002-2201-5137,
O.L. Mikhodui: 0000-0001-6660-7540

CONFLICT OF INTEREST

The Authors declare no conflict of interest

CORRESPONDING AUTHOR

M.O. Pashchyn
E.O. Paton Electric Welding Institute of the NASU
11 Kazymyr Malevych Str., 03150, Kyiv, Ukraine
E-mail: svarka2000@ukr.net

SUGGESTED CITATION

L.M. Lobanov, M.O. Pashchyn, O.L. Mikhodui, P.V. Goncharov, A.V. Zavdoveev, P.R. Ustymenko (2022) Electrodynamic treatment of welded joints of aluminium AMg6 alloy in the process of heating the weld metal. *The Paton Welding J.*, **4**, 3–7.

JOURNAL HOME PAGE

https://pwj.com.ua/en

Received: 22.02.2022
Accepted: 30.06.2022

https://doi.org/10.37434/tpwj2022.04.02

FEATURES OF THE STRUCTURE AND PROPERTIES OF METAL LAYERS DEPOSITED WITH PRE-APPLICATION OF TITANIUM AND BORON CARBIDES

V.V. Peremitko, I.V. Kolomoyets, V.I. Sukhomlyn

Dnipro State Technical University
2 Dniprobudivska Str., 51900, Kamianske, 2, Ukraine

ABSTRACT

Uneven wearing of working surfaces of parts, operating under friction, is a common cause for beginning of renovation and replacement times. One of the methods to avoid this problem is formation of surfaces of a variable composition and properties by arc surfacing. The work presents comparative analysis of the hardness and structure of the metal, deposited with pre-application of titanium and boron carbides on the processed surfaces. These materials were selected, proceeding from their impact on the deposited metal mechanical properties. The hardness, structure and composition of the deposited metal were studied. Hardness dependence on the heat input and material consumption in individual zones of the bead cross-section was analyzed. Regularities were established between accumulation in the formed beads of material pre-applied on the processed surface and the significance of structural transformations. A similar influence of both the carbides on the deposited metal structure was found. Bead metal hardness is 1.5 times higher at B_4C application, than when TiC is used. X-Ray spectral microanalysis revealed the influence of free carbon, formed as a result of compound decomposition, on structural transformation in the deposited metal. It was found that the largest accumulations of bainite are characteristic for zones with the highest carbon content. It was determined that pre-application of carbides, using the most common surfacing materials, allows producing deposited metal, matching by its properties the metal deposited with PP-Np-152 wire.

KEYWORDS: arc surfacing, solid wire, fused flux, titanium carbide, boron carbide, pre-application, local fixation, hardness, structure

INTRODUCTION

A common method to eliminate the nonuniformity of wear of contact surfaces, operating under the conditions of loads unevenly distributed over the area, is formation of surface layers of variable composition and properties, in compliance with the degree of loss of the initial weld geometry in different sections [1–5]. Such parts, in particular, are ball rolling mill rolls, roller conveyor rolls, supercharger blades, shafts, etc.

The positive effect from pre-deposition or addition of different alloying components during surfacing is known from published data [6–10]. Studying the possibilities of metal microalloying at surfacing with different materials [11] showed that addition of hardening elements or their compounds with carbon and nitrogen in the quantities of up to 0.2 % leads to producing a fine-grained, uniform structure of metal and more uniform distribution of alloying elements. The latter has a positive effect on the metal mechanical characteristics.

In particular, the positive effect of carbide compounds on wear resistance of the deposited layers should be noted, considering the direct dependence between carbide hardness and wear resistance [11–13].

One of the successful examples of realization of surfacing with an essential influence of carbide compounds in the deposited layers is the technology of producing metal by arc surfacing with formation of carbides of the elements, included into the flux-cored wire charge [12]. The above-mentioned method, however, envisages deposition of metal with the same carbide content over the entire surface, and the process of surface layer formation in such a way will be essentially more complicated. In work [12] metal deposition was performed by PP-AN 192 wire. The structure of such a metal consists of martensite with residual austenite and fine carbide inclusions. The hardness of such a metal is equal to at least *HB* 555.

More over, confirmation of the positive influence of carbide addition on the mechanical properties of the welded joints was obtained [14]. In this work, welding was performed by Sv-08 wire with addition of different modifiers, in particular, also TiC. As a result, weld metal with the continuous bainitic structure was obtained, without preservation of the carbide particles. It was established that titanium carbide increases the endurance limit of the layers by 35 MPa (in 1.08). Also known is application of tungsten carbide as the hardening component [13]. In particular, positive effect of this material on the properties of surface layers, operating under the conditions of gas-abrasive wear was found [14]. In the above-mentioned case, carbides formed from titanium, which is present in the composition of the flux-cored wire charge.

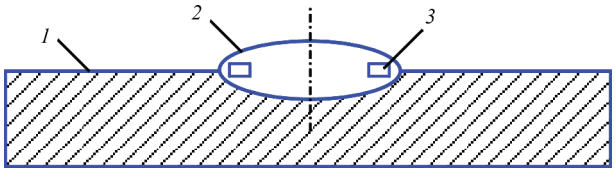

Figure 1. Scheme of additional material application: *1* — sample; *2* — deposited bead; *3* — points of prior fixation of boron or titanium carbides

Considering the high degree of preservation of the components, which can be further added, as well as the possibility of fixation of such materials selectively, in compliance with the real wear pattern, their pre-deposition on the treated surface looks promising [6–8]. Such a scheme also allows performing surfacing with application of widely used electrode wires and fluxes.

Earlier performed investigations showed the positive influence of prior fixation of layers of TiC mixture by GF-021 primer in the form of 2 mm wide bands along the edges of the planned beads [15]. Layers of a variable composition and properties form, and addition of the hardener by the above method allows reaching mechanical inhomogeneity of formation within each bead of zones, differing by their structure and properties from the surfaced base. During performance of the above studies, surface layers were obtained, within which zones of higher and lower hardness alternate with 1.6 times difference of its values. The latter led to a change of the nature of wear and at local increase of hardness the losses surface layer material can be even smaller, than in the case of continuous formation of the deposited layer of homogeneous composition and properties.

The objective of the work was to reveal the significance of the changes in the structure and strength characteristics of individual zones of the deposited layers by their comparative analysis, formed with prior local fixation of the hardeners in the form of carbides.

CONDITIONS OF RESEARCH PERFORMANCE

In view of the above-mentioned influence of carbides on the deposited metal properties, titanium (TiC) and boron carbides (B_4C) were selected for the laboratory study, the hardness of which is equal to 32000 and 36000 MPa, respectively.

Materials were deposited similar to work [15]. Plates from steel 20 of 10 mm thick, 100 mm wide and 100 mm long were used as experimental samples. Deposition was performed by 3 mm Sv-08A wire using AN-348A flux in ADC-1000 welding unit in the following mode: surfacing current — 500±1 A, arc voltage — 30±1 V, surfacing speed — 25–35 m/h,

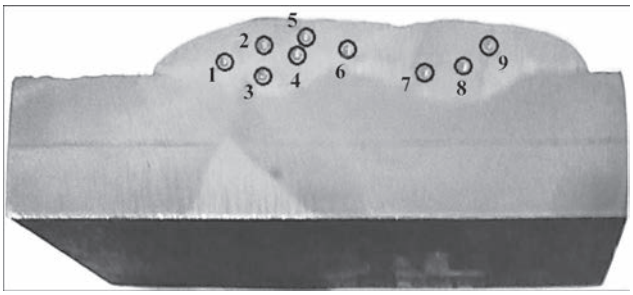

Figure 2. Sample for hardness measurement

eccentricity of material layer deposition — 5–8 mm. The scheme of additional material deposition is given in Figure 1.

Deposition was performed in one layer, overlapping of single beads was equal to 7 mm, deposited layer thickness was 2.5–3.0 mm, overlapping beads were deposited in pairs. Each pair of the beads was applied at a fixed value of heat input.

During experiment preparation a central compositional plan of the second order for two factors was used. Heat input q_h, J/mm and specific material consumption (m_s), g/run. mm were chosen as the influence factors. Hardness in three different areas was selected as the experiment response: along the deposited bead edges, in their lower part and in bead overlapping point. To measure the hardness the samples were cut across into 20 mm wide templates. Measurements were conducted in TK-2 hardness meter in seven points (Figure 2). Metallographic analysis was performed using photomicroscope Neophot 21 and scanning microscope REM-106i. X-ray microspectral analysis was conducted, using electron probe microanalyzer EPMA-1720. The size of the material area, from which the spectral component of X-ray radiation was obtained for chemical element identification, was equal on average to 70–90 nm on the bead edges and 50–70 nm in bead overlapping zone.

Treatment of experimental results was performed in STATISTICA 7.0 program. Results of metal hardness measurement with addition of TiC and B_4C are given in Table 1.

One can see from the Table that at B_4C addition metal hardness in overlapping area is 1.7 times higher, than in the same area at TiC addition (*HB* 506 at B_4C addition against *HB* 302 at TiC addition) under the condition of constant heat input, 1314 J/mm. This is attributable to higher stability of B_4C under the conditions of moderate thermal impact, higher intrinsic hardness and, consequently, greater presence of carbide particles in the metal.

Figure 3 gives the dependence of hardness change in overlap zone (area of adding different carbides).

One can see from Figure 3 that maximum increase of hardness in the bead overlap zone at TiC addi-

Table 1. Results of hardness measurement in bead deposition zones

Sample number	Heat input q_{run}, J/mm	Specific consumption m, g/$_{run}$, mm	$HB_{on\ bead\ periphery}$ (TiC)	$HB_{in\ overlap\ zone}$ (TiC)	$HB_{lower\ part}$ (TiC)	$HB_{on\ bead\ periphery}$ (B_4C)	$HB_{in\ overlap\ zone}$ (B_4C)	$HB_{lower\ part}$ (B_4C)
1	1848	0.032	255	293	241	298	333	269
2	1848	0	192	187	187	192	187	187
3	1314	0.032	293	302	262	432	506	403
4	1314	0	192	187	187	192	187	187
5	1536	0.032	248	255	277	325	354	373
6	1536	0	192	187	187	192	187	187
7	1848	0.016	293	302	262	285	306	255
8	1314	0.016	241	262	241	432	420	255
9	1536	0.016	192	269	255	246	373	246

tion, is observed at heat input values in the range of 1600–1800 J/mm and at specific hardener consumption of $3.2 \cdot 10^{-2}$ g/mm. At B_4C application hardness increase is recorded at somewhat smaller heat input values — 1400–1700 J/mm, and at the same losses of the hardener. When 1700 J/mm is exceeded, a lowering of hardness is observed. At the same time, addition of titanium carbide allows increasing the heat input to a maximum, assigned for the experiment (1848 J/mm) without causing any lowering of hardness. This is attributable to a higher melting temperature of TiC (3100 °C), as well as carbon saturation due to carbide decomposition. The influence of heat input on hardness is characterized by that the heat input is reduced at reduction of energy input, and, consequently, material burnout becomes smaller that promotes hardness increase.

Proceeding from the conducted studies, the influence of local addition of carbides on metal properties directly in the points of their addition, does exist. Owing to a short time of liquid pool existence and imperfect mixing of the melt, the hardener particles are predominantly preserved in the points of their previous fixation, causing 2.7 times increase of hardness there in case of boron carbide addition, compared to the central zone of the beads (*HB* 506 against *HB* 187) and 1.5 times on the edge, at a similar comparison (*HB* 432 against *HB* 293). At TiC addition in the overlapping area the difference is 1.6 times (*HB* 302 against *HB* 187), and 1.5 times on the edges (*HB* 293 against *HB* 192).

Thus, local addition of TiC to the periphery of the beads at maximum distance from the arc, allowed increasing the hardness in the area of addition by *HB* 115, whereas in work [13] hardness increased by *HB* 7.

Maximum value of hardness obtained in the overlap zone at B_4C addition (*HB* 506) is close to that of metal deposited with PP-AN 192 wire (*HB* 555) [12]. It confirms the possibility of formation of a high-strength metal with local addition of carbides without application of costly surfacing materials and potentially with smaller consumption of the hardener.

Metallographic analysis of the deposited metal revealed a structure in the overlap zones and on bead edges, which is characteristic for the case of higher carbon content (Figure 4). Maximum changes are observed in overlap zones, that is accounted for by the fact of the greatest presence of the hardener. In case of TiC addition the structure consists of bainite, martensite and ferrite. Considering the fact that ferrite forms the deposited metal base, presence of bainite, most probably, points to ferrite saturation by carbon from added carbide, as a result of thermodynamic decomposition of the latter. Now martensite, in its turn, may be the consequence of carbon decomposition in iron and additional alloying with manganese from

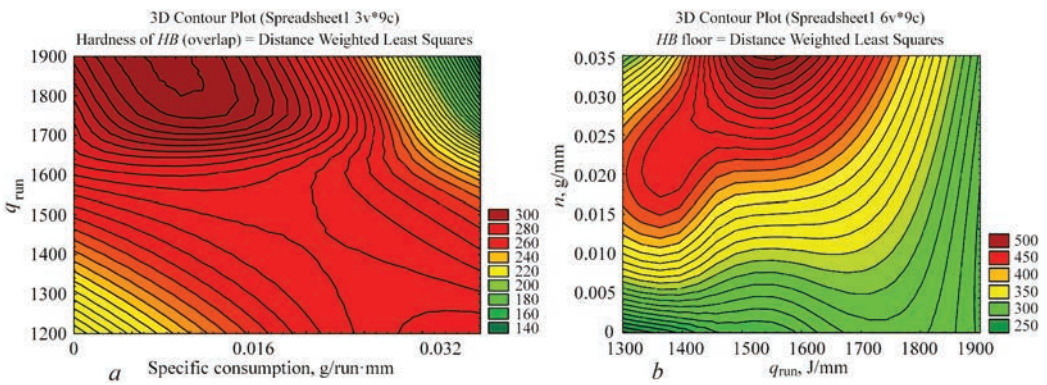

Figure 3. Dependence of metal hardness in bead overlap area on the heat input and specific consumption: *a* — at TiC addition; *b* — at B_4C addition

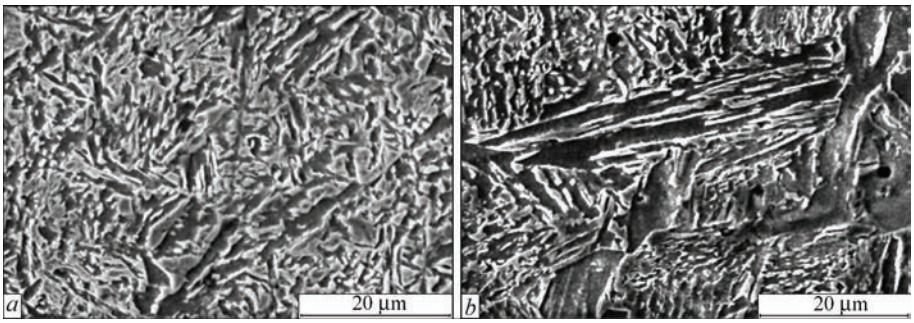

Figure 4. Metal microstructure in areas of separate bead overlapping: *a* — with TiC addition; *b* — with B_4C addition

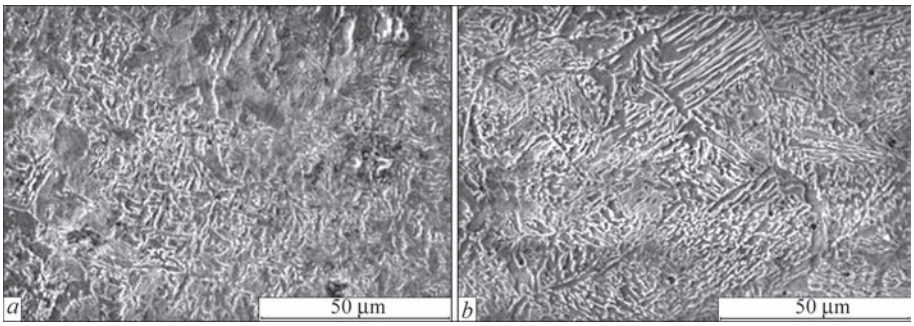

Figure 5. Metal microstructure on bead edge: *a* — with TiC addition; *b* — with B_4C addition

AN-348A flux that enhances the overall stabilization of austenite. Bainite is presented by compact in size and densely located areas within the austenite grains (Figure 4). This way, local TiC addition promotes less decomposition of the compound that is confirmed by single unsaturated areas of ferrite, while the structure produced in work [13] is continuous bainite.

The structure in the point of bead overlapping at B_4C addition (Figure 4) also is a combination of ferrite and bainite with carbide particle clusters, predominantly in ferrite areas. Bainite areas, in their turn, are much less in quantity in the case of B_4C addition, compared to a similar case with TiC. This observation, as well as an accumulation of boron carbides, is attributable to a different kinetics of formation of morphological features of the final structures, compared to TiC addition.

An increase of the number of ferrite areas with reduction of bainite presence is observed at the edge of the bead, deposited with TiC addition (Figure 5, *a*) without overlapping (where there is less hardener than in the overlap zones). This may be an indication of less significant saturation of ferrite by carbon. In a similar area, at B_4C addition (Figure 5, *b*), much less carbide particles, compared to the overlap zone, increase in bainite areas, and reduction of ferrite, are found. The latter, apparently, is attributable to greater decomposition of added material in this zone.

X-ray microspectral analysis of samples with TiC deposition was performed for a more detailed study of the influence of titanium carbide on the deposited metal structure and properties.

All the three variants of deposition of layers with hardener are given in Figure 6. One can see that on side beads the area of ferrite sections is greater than that of ferrite sections in the bead overlap zone. Bainite structures in bead overlap zone have a greater dispersion and signs of rapid crystallization: compact zones with uniform orientation of the bainite components are recorded. On side beads the bainite structure corresponds to longer time and lower rate of the solidification process.

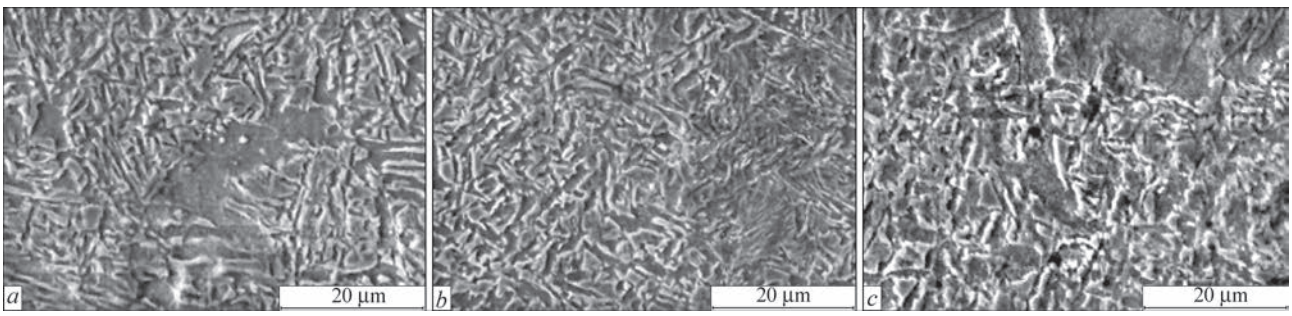

Figure 6. Metal microstructure in the cross-section of the beads, deposited with TiC addition: *a* — bead left edge; *b* — bead overlap zone; *c* — bead right edge

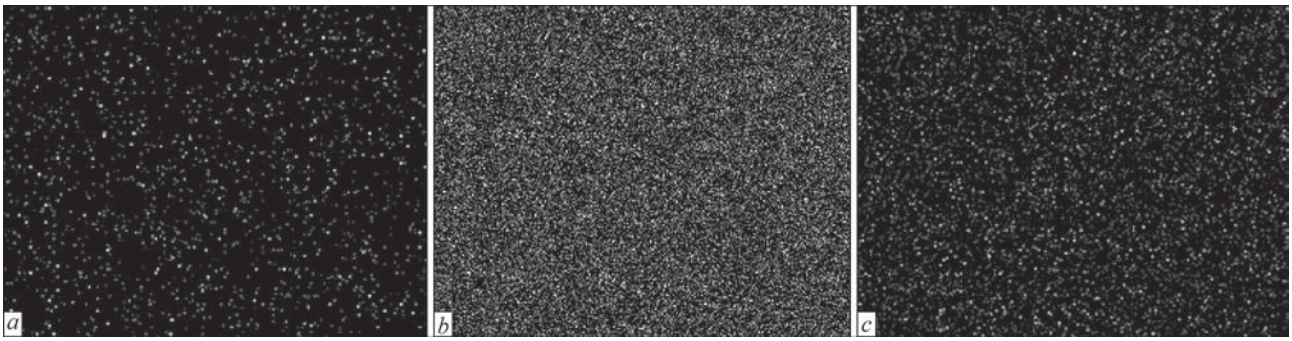

Figure 7. Ti distribution over the deposited bead cross-section: *a* — bead left edge; *b* — bead overlap zone; *c* — bead right edge

Table 2. Weight fraction of elements in the metal of different zones of surfacing with titanium carbide, %

Chemical element	Left bead		Overlap zone		Right bead	
	Ferrite	Bainite	Ferrite	Bainite	Ferrite	Bainite
Si	0.81–0.93	0.75–0.90	0.60–0.79	0.72–0.75	0.77–0.85	0.91–0.94
Mn	1.48–1.75	1.29–1.56	1.66–1.75	1.61–1.72	1.63–1.90	1.50–1.91

Figure 7 shows titanium distribution in the metal, deposited using titanium carbide. Arrangement of distribution patterns corresponds to structure patterns in Figure 6. One can see that in all the studied zones titanium distribution is relatively uniform. On bead edges, however, the overall quantity of titanium is smaller, and the dimensions of individual particles are larger.

Considering that titanium has a higher affinity to carbon, compared to iron (and other metals from the melt composition), as well as a high temperature of carbide formation in the surfacing pool, we can assume that the titanium carbide nuclei are exactly the centers of austenite crystallization, and later on, at austenite decomposition they are the centers of bainite and ferrite crystallization. Thus, titanium is exactly the main element of structure formation in different locations in the beads.

Distribution of the main chemical elements in the deposited metal composition is shown in Table 2.

Si and Mn concentration is rather high due to their presence in the base metal of the samples, in the surfacing wire and in the composition of AN-348A flux. Manganese improves austenite stability, and, thus, also the probability of shear structure formation. Silicon in the composition of ferrite and bainite enhances the hardness of these structural components. An almost the same Mn and Si concentration in ferrite and bainite structure is attributable to a feature of bainite transformation. During the latter, just carbon redistribution occurs and no redistribution of alloying elements takes place.

Thus, from the two considered carbides B_4C can be regarded more efficient in terms of metal hardness increase. This is due to the fact that despite the lower thermodynamic stability of the compound, B_4C ensures hardness values on average 1.4 times higher than TiC does.

CONCLUSIONS

1. A greater effectiveness of local pre-deposition of B_4C on the surface for arc surfacing, compared to TiC, was experimentally established: at 1314 J/mm heat input and B_4C specific consumption of $3.2 \cdot 10^{-2}$ g/mm, 2.7 times higher metal hardness is recorded. For metal with B_4C addition at heat input increase up to 1848 J/mm, the hardness is on average 1.4 times higher than with TiC participation.

2. Under the same heat input conditions and quantity of added hardener, the structure of metal of the deposited layers does not essentially differ. In layers with different hardeners, a ferrite structure with bainite areas is observed, that develops due to saturation with carbon, which forms as a result of carbide decomposition. In the case of B_4C hardening, a carbide cluster is recorded, predominantly in ferrite areas. Under the conditions of moderate heat input, boron carbide is more stable, than titanium carbide.

3. X-ray microspectral analysis of metal, deposited with TiC addition, confirmed an essential influence of free carbon on structural transformations in the deposited metal. In particular, it was found that in the bead overlapping zone TiC carbides of the size of several tens of nanometers serve as nuclei for crystallization and growth of a more dispersed bainite, compared with other zones of the beads.

4. Hardness of metal deposited with Sv-08A solid wire with further addition of boron carbide, is close to the values, characteristic for the case of application of PP-AN 192 flux-cored wire (*HB* 506 against *HB* 555) that confirms the good prospects for application of the

proposed scheme of further addition of carbides into the deposited metal layer.

REFERENCES

1. Leshchinskiy, L.K., Gulakov, S.V., Stepnov, K.K., Nosovskiy, B.I. (1985) *Newly designed hardfaced rolls improve rolling mill efficiency*. Ed. by P.V. Gladkiy. Kyiv, Ukraine [in Russian].
2. Ivanov, V.P. (2019) *Theoretical and technological bases of increasing the efficiency of electric arc surfacing on the basis of modeling of formation of welding pool*: Syn. of Thesis for Dr. of Tech. Sci. Degree. PDTU, Mariupol, Ukraine [in Russian].
3. Yaryza-Stetsenko A.V. (2012) *Increasing of arc hardfacing technology with variable chemical composition by its alloying from flux*: Syn. of Thesis for Cand. of Tech. Sci. Degree. DMA, Kramatorsk, Ukraine [in Russian].
4. Kragelskiy, I.V. (1968) *Friction and wear*. Moscow, Mashinostroenie [in Russian].
5. Chigarev, V.V., Ivanov, V.P., Psaryova, I.S. (2003) Increasing of details and parts performance by hardfacing of heterogeneous layer. *Zakhyst Metalurgiynykh Mashyn vid Polomok*, **7**, 234–237 [in Russian].
6. Schenfeld, V.Y. (2014) *Increasing of wear resistance of steel parts by surfacing with the use of carbon fiber materials*: Syn. of Thesis for Cand. of Tech. Sci. Degree. VDTU, Vinnytsya, Ukraine [in Russian].
7. Peremitko, V.V. (2014) Wear resistant arc surfacing over the layer of alloying charge. *The Paton Welding J*., **8**, 54–57.
8. Peremitko, V.V., Panfilov, A.I. (2017) Arc surfacing of layers of metal of varying composition and hardness. *The Paton Welding J*., **7**, 38–42. DOI: https://doi.org/10.15407/tpwj2017.07.08
9. Kuznetsov, V.D., Stepanov, D.V. (2015) Structure and properties of welded joint's metal modificated by nanooxides. *The Paton Welding J*., **11**, 10–16.
10. Kuznetsov, V.V., Stepanov, D.V. (2015) Wear resistant surfacing with feeding of nanopowders to weld pool. *The Paton Welding J*., **5–6**, 52–56.
11. Babinets A.A., Ryabtsev I.O. (2021) Influence of modification and microalloying on deposited metal structure and properties (Review). *The Paton Welding J*., **10**, 3–10. DOI: https://doi.org/10.37434/tpwj2021.10.01
12. Ryabtsev, I.A., Panfilov, A.I., Babinets, A.A. et al. (2015) Structure and abrasive wear resistance of deposited metal hardened with carbides of different types. *The Paton Welding J*., **5–6**, 78–82.
13. Zhudra, A.P. (2014) Investigation of wear resistance of composite alloys under the conditions of gas-abrasive wear at elevated temperatures. *The Paton Welding J*., **11**, 28–31.
14. Peremitko, V.V., Kolomoyets, I.V., Sukhomlin, V.I. (2019) Effect of preliminary application of alloying powders on the structure and hardness of deposited metal. *The Paton Welding J*., **9**, 30–33. DOI: https://doi.org/10.15407/tpwj2019.09.05
15. Peremitko, V.V., Kolomoyets, I.V. (2021) Influence of orientation of zones of higher hardness of composite layers on their resistance to wear. *Archives of Materials Science and Engineering*, **110**, 59–71.

CONFLICT OF INTEREST

The Authors declare no conflict of interest

CORRESPONDING AUTHOR

V.V. Peremitko
Dnipro State Technical University
2 Dniprobudivska Str., 51900, Kamianske, 2,
Ukraine. E-mail: vperemitko1965@gmail.com

SUGGESTED CITATION

V.V. Peremitko, I.V. Kolomoyets, V.I. Sukhomlyn (2022) Features of the structure and properties of metal layers deposited with pre-application of titanium and boron carbides. *The Paton Welding J*., **4**, 8–13.

JOURNAL HOME PAGE

https://pwj.com.ua/en

Received: 19.04.2022
Accepted: 30.06.2022

https://doi.org/10.37434/tpwj2022.04.03

CENTRIFUGAL PLASMA SURFACING OF DRILL PUMP BUSHINGS

O.I. Som

Plasma-Master Co. Ltd.
3 Akademik Krzhizhanovskii Str., 03142, Kyiv, Ukraine

ABSTRACT

Features of centrifugal plasma surfacing using powders of three different alloying systems based on iron and nickel were studied. It is found that at centrifugal plasma surfacing the iron-based test powder has the best welding-technological properties. It allows producing deposited metal of 200Kh15D2MS2R type. The layer deposited with this powder, has a microstructure of uniform height and ensures increase of the sleeve wear resistance 5–6 times, compared to batch-produced ones, which are made from steel 70 and quenched by HFC. A design of the bushing component is proposed with replaceable surfaced sleeve, which is more adaptable to fabrication and allows repairing it by simple replacement of the worn sleeve.

KEYWORDS: centrifugal plasma surfacing, surfacing alloys, deposited metal, metal structure, wear resistance, carbides, hardness, layer thickness

INTRODUCTION

Drilling pumps are used in oil and gas industry for well washing during drilling [1]. Maintaining the high pressure and required flow rate of the solution for washing in the well depends predominantly on reliable operation of the cylindrical bushing-piston pair. Unfortunately, because of the high content of abrasive particles in the solution, the cylindrical bushings quickly wear and fail.

Bushings are made from 70, 95Kh18, Kh12MF tool steels. Steel 70 is the most common as the most accessible and inexpensive. However, bushings made from this steel only last 150–200 h before they go out of service, which is obviously not enough. Different methods are used to strengthen the bushing working surface, in order to increase the bushing wear resistance. Hardening with high frequency currents (HFC) is the most widely used in practice [2, 3].

Bimetal bushings are also used, which were produced by centrifugal casting. The working layer from high-chromium cast iron ChKh28 15–20 mm thick, which is formed at pouring, is hardened by HFC to hardness *HRC* 62–65. The service life of such bushings reaches 600–800 h that is quite acceptable in most cases [4].

Also known is application of bushings with a ceramic insert, which ensures the operating time of up to 3000 h. They, however, are very expensive and are very seldom applied [5].

PWI proposed application of the method of centrifugal plasma surfacing (CPS) to increase the bushing wear resistance [6, 7]. The essence of this method consists in surface melting of a layer of filler powder, which is predeposited on the surface of the processed part by the direct plasma arc, burning in argon between the nonconsumable tungsten electrode and the item. During surfacing the part rotates at a certain speed in the upgraded lathe chuck (Figure 1).

The main advantage of CPS is the possibility of deposition of relatively thin (2.5–3.0 mm) layers of wear- and corrosion-resistant material with a high productivity and smooth surface that allows minimizing the machining. However, at CPS a structural heterogeneity by height (thickness) of the deposited layer can develop as a result of the possible different specific density of the structural components of the deposited metal. Such a structural heterogeneity can have a negative effect on the deposited metal service properties.

The objective of the work consists in selection of wear-resistant powders, suitable for centrifugal plasma surfacing of the bushings, studying their welding-technological properties, microstructure and wear resistance of the deposited layers. It was also necessary to develop the design of the bimetal bushings, perform their surfacing and subsequent experimental-industrial testing under different climatic conditions.

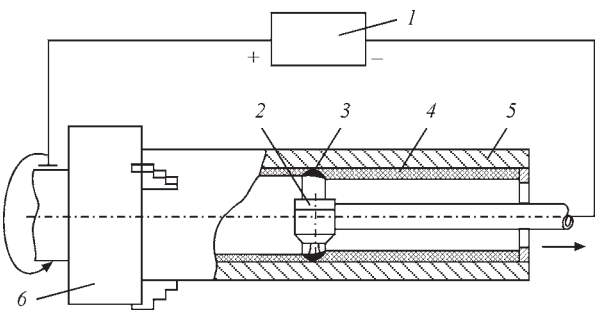

Figure 1. CPS diagram: *1* — power source; *2* — plasmatron; *3* — circular weld pool; *4* — filler powder; *5* — part; *6* — lathe chuck

Chemical composition of the studied types of the deposited metal

Number	Type of deposited metal (powder grade)	Weight fraction of elements, %							
		C	Si	B	Cr	Ni	Fe	Mo	Others
1	N75Kh15S4R4(PG-SR4)*	0.74	3.25	3.74	16.2	Base	2.1	–	–
2	250Kh30S2R(PG-AN1)*	2.21	2.15	1.61	29.6		Base	Base	2.08 Mn
3	200Kh15D2MS2R (test)	2.24	2.43	1.31	14.9			1.15	2.12 Cu0, 0.48 Al–Ce

*Made to GOST 21448–75 [8].

MATERIALS AND PROCEDURES FOR CONDUCTING EXPERIMENTS AND INVESTIGATIONS

Selection of powders for surfacing was based on the technological features of CPS method, and requirements made of the deposited layer of the bushings. The deposited metal meeting these requirements, should be resistant to abrasive and hydroabrasive wear, cavitation, and should have high enough corrosion resistance and casting properties.

Three powders were selected for studying and surfacing the test bushings, which ensure producing wear-resistant nickel- and iron-based alloys (see Table).

Alloy No. 1 is a well-known self-fluxing nickel-based alloy. It has a high wear-resistance, low melting temperature (1050–1100 °C) and excellent casting properties.

Alloy No. 2 is a high-chromium cast iron, which is additionally alloyed by boron to improve the wear resistance and casting properties.

Alloy No. 3 is an iron-based experimental alloy, specially developed for CPS, taking into account the technological features of this surfacing method. It is additionally alloyed by 0.5 % alumocerium for refining its structure.

The welding-technological properties of the powders were studied at surfacing samples in the form of thick-walled bushings, which simulate the real parts. Bushing dimensions are as follows: inner diameter of 100 mm, outer diameter of 160 mm and length of 200 mm. Surfacing modes were selected, taking into account the investigation results [6, 9]. The evaluation criterion was the number of cracks in the deposited layer, presence of unevenness, slagging and pores on its surface, as well as a metallurgical bond between the main and deposited metal. The samples cut out of these bushings were used for investigation of the microstructure, hardness and wear resistance of the deposited metal.

INVESTIGATION RESULTS AND THEIR DISCUSSION

Investigations of the surfaced samples showed that all the three powders ensure good formation of the deposited metal. The deposited layer surface is quite smooth with a slight oxide film build-up which can be easily removed. Pores and slagging are absent.

However, longitudinal cracks were detected in the deposited metal of all the three types. Their greatest number (3) of them was in deposited metal No. 2. They could not be avoided, either by increase of surfacing heat input, or preheating application. Appearance of cracks could be completely avoided only due to reduction of the bushing wall thickness to 15 mm. In this case they are more uniformly preheated and become less rigid.

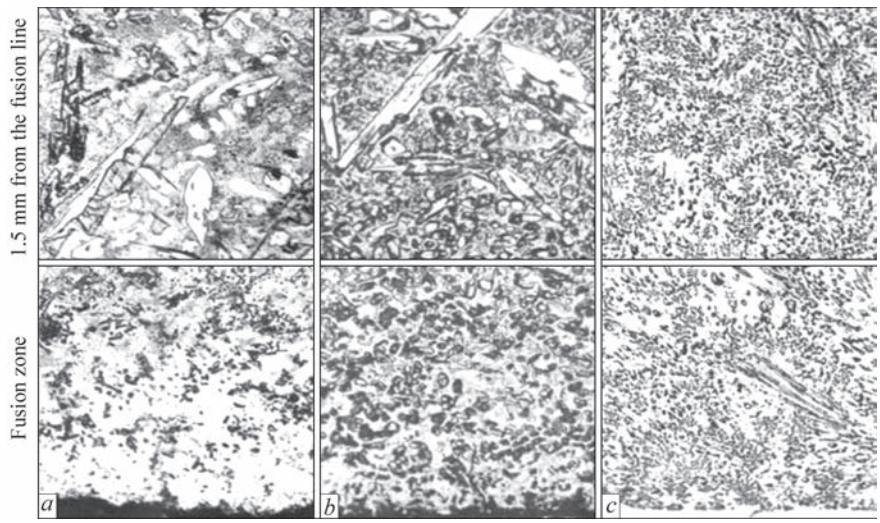

Figure 2. Microstructure (×320) of metal deposited by centrifugal plasma method: *a* — deposited metal N75Kh15S4R4; *b* — deposited metal 250Kh30S2R; *c* — test deposited metal 200Kh15D2MS2R

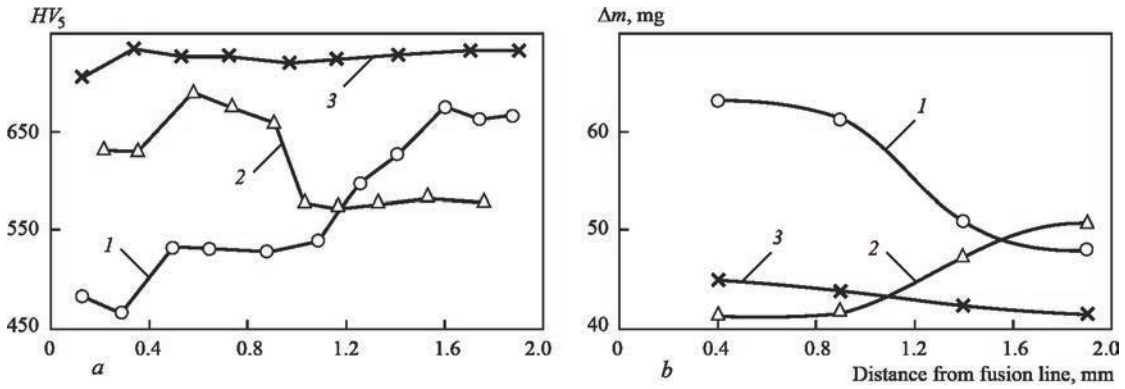

Figure 3. Hardness (*a*) and wear resistance (*b*) distribution by the thickness of the layer deposited by the centrifugal method by PG-SR4 (*1*), PG-AN1 (*2*) powders and test powder (*3*)

At CPS, formation of the deposited metal structure has its features. The deposited metal layer forms at slow cooling and under the conditions of the action of considerable centrifugal forces (up to 50 g), which may lead to structural heterogeneity by deposited layer thickness, as a result phases liquation, because of their different density.

Microstructural studies of deposited metal No. 1 and No. 2 showed that two zones can be distinguished in them: a eutectic one of 0.3–0.4 mm length at the fusion line and hypereutectic one with large primary carbides and chromium carboborides in the middle and upper zones of the deposited layer (Figure 2, *a*, *b*). These carbides as lighter ones, are driven upwards and are located in the direction of heat removal. No noticeable structural heterogeneity was revealed in deposited metal No. 3 (Figure 2, *c*). The microstructure is of a eutectic nature along the entire thickness of the layer without any large primary carbides or chromium carboborides.

The eutectic and hypereutectic zones of deposited metals No. 1 and No. 2 differ also by their hardness. In deposited metal No. 1 it increases in the direction towards the surface, and in the deposited metal No. 2, it, contrarily, decreases (Figure 3, *a*, curve *1* and *2*). Unlike that, hardness across the thickness of deposited layer No. 3 is stable (Figure 3, *a*, curve *3*). It is equal to *HV*5 700–720.

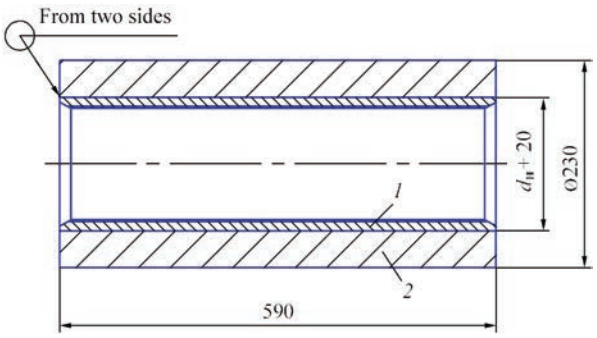

Figure 4. Design of the composite bushing of U8-6MA2 drill pump with the surfaced sleeve: *1* — surfaced thin-walled sleeve; *2* — case

Considering the structural heterogeneity of the deposited metal across the deposited metal thickness, the wear resistance of each of its zones was studied separately. For this purpose the layer was ground to different depth with a step of 0.5 mm. Testing conditions were selected so that linear wear of the sample in the studied zone did not exceed the above-given value. Testing was conducted in NK-M machine [10]. Testing parameters were as follows: sliding speed of samples of 0.6 m/s; mean specific pressure per sample of 0.5 MPa, friction path of 400 m. Quartz sand was used as abrasive. Test results are given in Figure 3, *b*.

As we can see, wear resistance of deposited metal Nos 1 and 2 differs in different zones, although insignificantly (15–20 %). It is in a certain correlation with hardness, i.e. with hardness increase in the hypereutectic zone for alloy No.1 the wear resistance becomes higher, and with its decrease for (alloy No. 2) it also decreases.

Wear resistance of the studied deposited metal No. 3, similar to its hardness, is at a very high level across the layer thickness, and changes only slightly, making this type of deposited metal a highly promising material for CPS of bushings.

EXPERIMENTAL-INDUSTRIAL VERIFICATION OF INVESTIGATION RESULTS

Proceeding from the conducted studies, powders Nos 1 and 3 were selected for surfacing the test parts, which showed the best results as to wear resistance. When manufacturing the bushings, the design of a composite bushing was realized, which consists of a thick-walled case and thin-walled surfaced sleeve, which is put into it by a hot fit (Figure 4).

The case and sleeve material is steel 20. The bushing components, despite the higher labour content of their manufacturing, have several advantages, compared to monolithic ones:

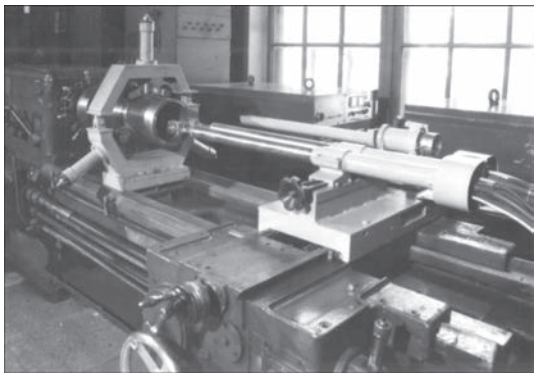

Figure 5. UD-251 experimental unit for CPS

● surfacing a thin-walled sleeve (10–12 mm) is less energy-consuming, simpler in terms of prevention of cracks in the deposited layer and more efficient;

● compressive stresses, developing in the deposited metal at sleeve pressing, are favourable for its serviceability, as they lower the tensile stresses, arising at bushing operation under the impact of inner working pressure;

● composite bushings are repairable due to the possibility of replacement of the worn bimetal sleeve by a new one, while preserving the old thick-walled case that allows saving a lot of metal and lowers the labour cost.

Surfacing the test sleeve billets was performed in UD-251 machine, which is based on a lathe, with two plasmatrons simultaneously (Figure 5).

The deposited layer thickness was selected, proceeding from the extent of admissible wear, machining allowance and billet shrinkage, resulting from their heating at surfacing. Average thickness of the deposited layer was in the range of 2.5–3.0 mm, after grinding it was 1.5–2.0 mm.

At the first stage 10 bushings for U8-6MA2 pump were made, of which 4 bushings of 180 mm diameter were surfaced by powder of alloy No. 1, and 6 bushings of 160 mm diameter — by powder of alloy No. 3. A sample of the surfaced bushing with partial grinding is shown in Figure 6.

Figure 6. Appearance of a surfaced bushing of 160 mm diameter

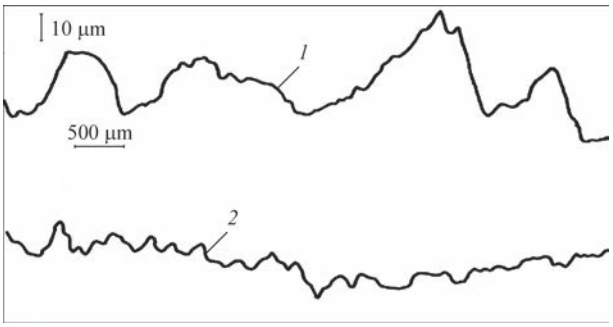

Figure 7. Profilograms of worn surfaces of drill pump bushings, surfaced by powders of N75Kh15S4R4 (*1*) and 200Kh15D2MS2R (*2*)

Trials of the test bushings were conducted in West Ukraine at turbine drilling. Testing conditions were as follows: drilling depth — up to 2500 m, pressure in the pump — 11–14 MPa, solution density of 1.11–1.18 t/cm^3, static shear stress (SSS)-5/10, abrasive content in the solution — 3–5 %. Test procedure envisaged test bushing operation in the same pump in a pair with batch-produced one, which was made from steel 70 and strengthened by HFC hardening. In those cases, when batch-produced bushings failed earlier than the test ones, they were replaced by new ones. Pistons with rubber collars of "Neftemashremont" Plant, Baku, TU 26-02-1059–87 were used at testing.

Comparative testing of the surfaced and batch-produced bushings showed that the nickel-based deposited metal No.1 (N75Kh15S4R4), despite its rather high hardness *HRC* 59, has low resistance, particularly at higher pressure of the washing solution. After 100 h of operation at turbine drilling the bushing wear was 0.6 mm per side. Deep longitudinal scratches were detected on the deposited layer surface (Figure 7, *a*), as well as cavitation damage centers.

More over, the piston rubber collars failed very quickly at operation in a pair with this alloy (Figure 8).

The pistons had to be replaced every 20 h of operation, whereas in a pair with batch-produced bushings they last 70–80 h. The cause for such a phenomenon

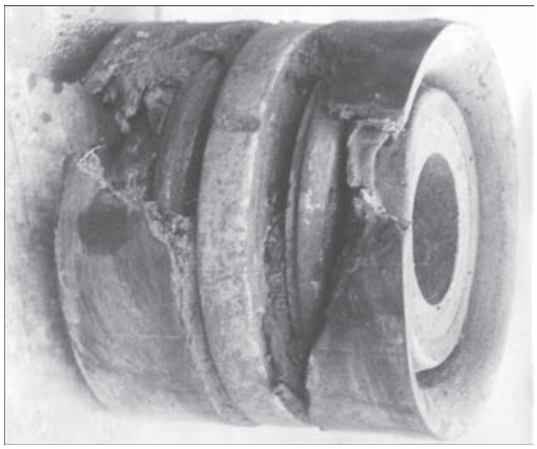

Figure 8. Appearance of the piston with rubber collars after studying a bushing deposited with powder of N75Kh15S4R4 alloy

can be the low heat conductivity of the nickel alloy, causing poor heat removal from the friction zone of the rubber collar and deposited working layer of the bushing. Under these conditions, the rubber has enough time to heat up to destruction temperature and fail.

Bushings, which were surfaced by powder of iron-based test alloy (200Kh15D2MS2R) showed quite high resistance. Average operating life is equal to 1150–1200 h that is 5–6 times higher that the resistance of batch-produced parts under these conditions. Some of the parts after 1200 h of operation did not exhaust their expected useful life and were removed from testing, due to completion of drilling operations.

Investigation of working surfaces of the bushings after testing showed that they also have longitudinal scratches. However, the microroughness height is much smaller than in the two previous cases (Figure 7, *b*). No "flushing", characteristic for batch-produced bushings, was observed on any of the surfaced bushings. It should be also noted that the service life of the pistons in a pair with bushings, surfaced by powder of test alloy No. 3, is 1.5–2.0 times higher, compared to batch-produced bushings, that is, probably, attributable to more favourable microrelief of the working surface and higher heat conductivity of the working layer.

Several more batches of the bushings surfaced by the test alloy powder, were manufactured and tested which also confirmed their high serviceability.

CONCLUSIONS

1. Centrifugal plasma surfacing is an efficient method to improve the pump bushing wear resistance. Optimum thickness of the deposited layer, proceeding from the service conditions and machining allowances, is 2.5–3. 0 mm.

2. Test powder 200Kh15D2MS2R was proposed, which completely meets the needs of centrifugal plasma surfacing and ensures high wear resistance of the metal deposited with this powder. Drill pump bushings, surfaced with this powder, during performance of work in West Ukraine, demonstrated 5–6 times higher resistance, than batch-produced ones, made of steel 70 and strengthened by HFC hardening. Increase of resistance of pistons with rubber collars 1.5–2.0 times was also noted here.

3. The developed design of a composite bushing with a replaceable sleeve is quite efficient technologically and ensures a high performance of the drill pump. Owing to repair possibilities it allows saving a considerable quantity of the deficit metal.

REFERENCES

1. Nikolich, A.S. (1973) *Drill piston pumps*. Moscow, Nedra [in Russian].
2. Mkrtychyan, Ya.S. (1984) *Improvement of efficiency of drill pump units*. Moscow, Nedra [in Russian].
3. Samoilovich, Yu.A. (2017) Increase of operating life of drill pump barrel by thermocyclic treatment of barrel material. *Stal*, **4**, 44–49 [in Russian].
4. *Site* LLC Bursnab. http://www.bursnab.com, Moscow [in Russian].
5. *Site* LLC RosPrombur. http://www.rosprombur.ru, Moscow [in Russian].
6. Gladky, P.V., Som, A.I., Pereplyotchikov, E.F. (1984) Centrifugal surfacing. In: *New processes of surfacing, properties of deposited metal and transition zone*. Kyiv, PWI, 31–34 [in Russian].
7. Yushchenko, K.A., Gladky, P.V., Som, A.I. et al. (1991) *Method of centrifugal surfacing*. USSR author's cert. 1636151. Publ. 23.03.1991 [in Russian].
8. (1979) *Surfacing materials of countries-members of CMEA*. Catalog. MTsNTI [in Russian].
9. Som, A.I., Zelnichenko, A.T. (2010) Numerical calculation of thermal processes in centrifugal plasma powder cladding. *The Paton Welding J.*, **6**, 13–18.
10. Yuzvenko, Yu.A., Gavrish, V.A., Marienko, V.O. (1979) Laboratory units for evaluation of wear resistance of deposited metal. *In: Theoretical and technological principles of surfacing. Properties and tests of deposited metal*. Kyiv, PWI, 23–27 [in Russian].

CORRESPONDING AUTHOR

O.I. Som
Plasma-Master Co. Ltd.
3 Akademik Krzhizhanovskii Str., 03142, Kyiv, Ukraine. E-mail: info@plasma-master.com

SUGGESTED CITATION

O.I. Som (2022) Centrifugal plasma surfacing of drill pump bushings. *The Paton Welding J.*, **4**, 14–18.

JOURNAL HOME PAGE

https://pwj.com.ua/en

Received: 19.04.2022
Accepted: 30.06.2022

APRIL 7, 1947 Henry Ford (1863–1947) died. He was an US industrialist, owner of car factories all over the world, author of 161 US patents. Henry Ford organized mass production of cars on an assembly line, and focused on application of resistance, arc and gas welding instead of forge welding and riveting. The design of the chassis, bodies, exhaust pipes, tanks and a number of other assemblies and parts was created already taking into account the welding technology capabilities. Chassi in the form of a frame was welded by oxyacetylene flame at first, and then by consumable electrode arc. A significant part of the joints were made by resistance butt, seam and spot welding.

https://doi.org/10.37434/tpwj2022.04.04

FIBRE LASER WELDING OF ALUMINIUM ALLOYS OF 7xxx SERIES (Al–Zn–Mg–Cu) BY NONTHROUGH THICKNESS WELDS

V.M. Korzhyk[1,2], V.Yu. Khaskin[1,2], A.A. Grynyuk[2], S.I. Peleshenko[3], Yao Yuhui[4], S.G. Hrygorenko[2], V.O. Shcheretskyi[2], O.S. Kushnareva[2]

[1]China-Ukraine E.O. Paton Institute of Welding of Guangdong Academy of Sciences.
Guandong Provincial Key Laboratory of Advanced Welding Technology
Guangzhou, 510650, China
[2]E.O. Paton Electric Welding Institute of the NASU
11 Kazymyr Malevych Str., 03150, Kyiv, Ukraine
[3]National Technical University of Ukraine «Igor Sikorsky Kyiv Polytechnic Institute»
37 Peremohy Ave., 03056, Kyiv, Ukraine
[4]Shenzhen Hanzhizi Technology Co., Ltd.
6th Floor. Building B, Bantian International Center, 5 Huancheng South Road, Longgang District, Shenzhen, Guangdong, China

ABSTRACT

The paper deals with the features of laser welding with incomplete (nonthrough thickness) penetration of high-strength aluminium alloys of 7xxx series. It was found that at joining of 1.5 mm sheets by fibre laser welding to the depth of 0.5–0.7 mm there arises the risk of formation of pores, in particular, in the root zone, streaks of oxide film in the weld lower part, as well as hot cracks. The latter can be eliminated by reducing the welding heat input below 25–30 J/mm. The weld metal is characterized by an equiaxed finely dispersed structure with grain size of 10–15 μm for 7005 alloy and 15–25 μm for 7075 alloy. In the fusion zone, the grains are of an elongated shape with 2.5–3.0 coefficient for 7005 alloy and 2–5 for 7075 alloy. In the HAZ the grain length is reduced, the shape coefficient becomes 3–5 and 3.0–3.5 for 7005 and 7075 alloys, respectively. At performance of laser welding with small (~5 J/mm) values of the heat input, microhardness of the welds and HAZ is rather uniform, and close to that of the base metal. For 7075 alloy microhardness drop to 20 % was observed in the fusion zone region that is due to formation of grains of an elongated shape with shape coefficient of 2–5. The found drawbacks can be eliminated through reduction of pulsations of the vapour-gas channel with simultaneous increase of the stability of its existence and introduction of cathode breaking of the oxide film.

KEYWORDS: aluminium alloys of 7xxx series, laser welding, weld formation, graininess, defects, ways to eliminate

INTRODUCTION

Alloys of 7xxx series (Al–Zn–Mg–Cu system) have the highest strength among aluminium alloys. After heat treatment this value is more than 500 MPa [1]. Owing to a combination of high strength with low density, they are quite attractive for application in manufacture of modern transportation systems [2]. However, the weldability of such alloys is poor, because of the high susceptibility to hot cracking, high coefficient of thermal expansion and low temperature of evaporation of some alloying elements, in particular Zn and Mg [3]. The above drawbacks promote formation of some welding defects, such as cracks and pores, particularly, in the case of laser welding with incomplete (or partial) penetration [4].

Incomplete penetration welds are used for sealing the flanges or some structures with voids, where electronic equipment is located. The welding operation is here performed as an element of finish mounting, and in the case of full penetration, there is the danger of complete damage of the interior fittings. Here, laser welding is used to minimize or completely eliminate residual deformations. Such structures are used, in particular, in rocket engineering. Their welded joints should ensure tightness and certain strength, but because of relatively short life, the question of cyclic load resistance is not considered. Therefore, consideration of the features of formation of welded joints of aluminium alloys of 7xxx series, in particular, with incomplete penetration, is urgent.

In modern industry, laser welding is ever wider applied. It is used not only in the aerospace industry, but also in car building, in automotive industry and in many other areas of activity [5]. However, this process is still being studied, and it is applied predominantly to produce nondetachable structures from aluminium alloys of 2xxx, 5xxx and 6xxx series [6]. The question of the features of laser welding application to produce a nondetachable structure from 7xxx series alloys has already been considered to some extent in works [6,

Table 1. Element content (wt.%) in high-strength 7005 and 7075 aluminium alloys

Alloy	Definition type	Al	Si	Fe	Cu	Mn
7005	Alloy grader	Base	Up to 0.35	Up to 0.40	Up to 0.10	0.2–0.7
	General analysis	93.12–93.37	0.43–0.72	–	0.18–0.19	0.25–0.33
	Analysis in the grain volume	88.93–92.78	0.51–0.69	–	0.16	0.62–0.64
	Inclusions in the grain volume	–	0.86–1.60	10.81–28.74	0.2–0.3	2.41–3.09
7075	Alloy grader	Base	Up to 0.40	Up to 0.50	1.2–2.0	Up to 0.30
	General analysis	89.84–90.66	0.45–0.62	–	1.53–1.86	0.13–0.27
	Analysis in the grain volume	89.97–90.41	0.55–0.56	–	1.46–1.63	0.12–0.23
	Inclusions in the grain volume	–	0.32–39.51	6.75–29.86	0.94–7.18	0.08–2.83

Table 1 (cont.)

Alloy	Definition type	Mg	Cr	Zn	Ti	Other
7005	Alloy grader	1.0–1.8	0.06–0.20	4–5	0.01–0.06	Zr 0.08–0.20 Other up to 0.15
	General analysis	0.56–0.75	–	5.01–5.37	–	–
	Analysis in the grain volume	0.76–0.80	–	5.1–8.89	–	–
	Inclusions in the grain volume	0.24–0.54	–	2.02–3.57	–	–
7075	Alloy grader	2.1–2.9	0.18–0.28	5.1–6.1	Up to 0.20	Up to 0.15
	General analysis	0.91–1.10	–	6.02–6.45	–	–
	Analysis in the grain volume	1.04–1.12	–	6.41–6.74	–	–
	Inclusions in the grain volume	0.17–30.64	5.32–6.23	1.03–6.91	–	–

7]. So, the basic physical processes of laser radiation interaction with aluminium alloys were considered in work [6], and in work [7] laser welding of 7075 alloy was compared with microplasma and laser-microplasma. It was determined that in laser welding there is the risk of formation of inner pores and hot cracks, in particular those associated with internal inclusions and weld defects.

In work [8] the influence of heat input in laser welding of 7075 alloy on the change of element concentration in the weld and, consequently, on their hot cracking susceptibility was considered. It is rational to consider investigations in this direction, in particular, for the case of making welds with incomplete penetration of the butt. Available research results do not completely disclose a range of important issues, concerning formation of particular structures at application of certain parameters of laser welding mode, formation of characteristic defects (primarily pores and cracks), and determination of the ways to eliminate them.

The objective of this work is formation of characteristic structures of the joints and the risk of appearance of defects of the type of pores and cracks at laser welding of aluminium alloys of 7xxx series, made with partial (nonthrough thickness) penetration.

The following problems were solved to achieve this goal:

- performance of laser welding of samples of 7xxx series alloys, determination of mode parameters by the criteria of sound formation of the upper bead at fixed penetration depth;
- making sections, studying the structural features of the produced welded joints;
- determination of characteristic defects and possible causes for their formation;
- checking the possibility of elimination of the defined defects by using a hybrid laser-microplasma welding process.

Samples from high-strength 7005 and 7075 alloys were prepared to conduct experiments on determination of laser welding mode parameters. Sample size was 50×50×δ, where δ = 1.5 and 3.0 mm. During the experiments laser welding of fillet joints was performed, focusing on penetration depth of approximately 0.5–0.7 mm. Table 1 gives both the published data on chemical composition of these alloys, and our own. The latter are individual element measurements, made by the method of analytical-scanning microscopy. This method was used to determine both the integral content of individual selected elements of the alloy, and their content in the bulk of individual grains. The size of the latter was as follows: for 7005 alloy $Dg = h \times l$ = (4–7)×(20–35) μm, for 7075 alloy $Dg = h \times l$ = (5–15)×(30–70) μm, where h is the height, and l is the length of the grain (Figure 1). The grain shape coefficient was: for 7005 alloy l/h = 5, for 7075 l/h = 4.5–6.0. *HV* microhardness at 100 g load was: for 7075 alloy 624–636 MPa, and for 7075 alloy it was 1050–1240 MPa.

Experiments were performed using fiberoptic laser of up to 2000 W power (MFSC-2000W model, Max Photonics Company, PRC), as well as a set of plasma welding equipment, which consisted of CEBORA TIG

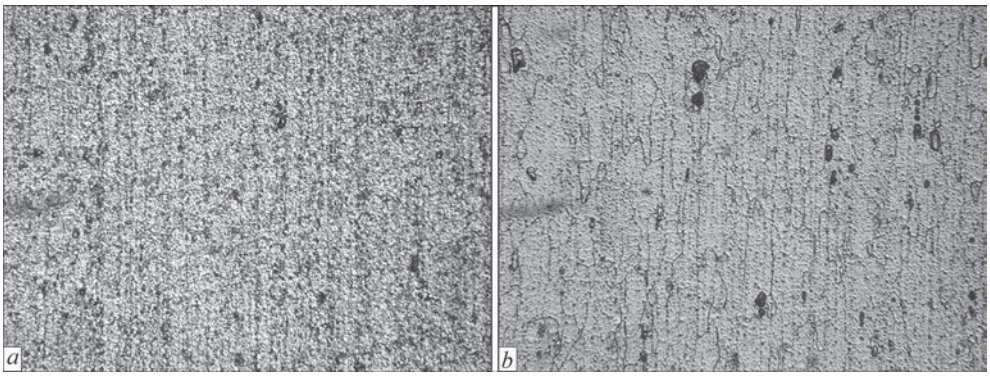

Figure 1. Base metal microstructure (×500): *a* — 7005 alloy; *b* — 7075

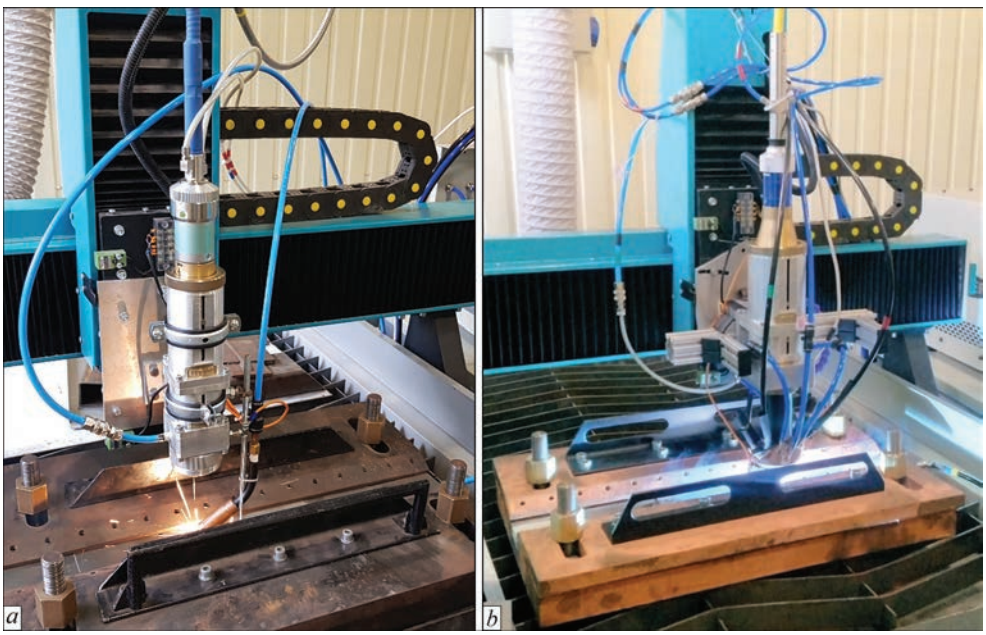

Figure 2. Appearance of a laboratory stand for welding: *a* — laser; *b* — laser- microplasma

AC-DC EVO 450T Robot source and PW30 plasma module (Cebore Company, Italy). A proprietary laboratory stand with replaceable burners was used for laser and laser-microplasma welding (Figure 2). Welding mode parameters were selected by such criteria of sound formation, as absence of caverns and pores, cracks, undercuts on the weld surface that can be recorded visually. The main parameters of the mode are given in Table 2.

To conduct metallographic analysis transverse templates were cut out of the produced joints and microsections were prepared. Here, ion-vacuum etching was used to reveal the microstructure. Results on the made joints were investigated by the methods of optical (Versamet-2 and Neohpot-31 microscopes) and analytical scanning (SEM-515 microscope of PHILIPS Company, Holland) microscopy. Investigations were conducted sequentially in the following sections of the samples: remelted weld metal → fusion line → HAZ → base metal. Optical microscopy was used to study the structural changes in these sections at up to 500× magnifications. Microhardness was measured, using LM-400 microhardness meter (LECO) series). Analytical scanning electron microscopy was used to determine the chemical composition of weld sections (general and local point analysis).

Laser welding by nonthrough thickness welds can be used to produce tight joints, for instance, to weld flanges. Therefore, technological studies were performed by welding simulators in the form of fil-

Table 2. Main welding mode parameters of 7005 and 7075 alloy samples

Welding	Laser radiation power, W	Microplasma power, W		Welding speed V, mm/s	Gas flow rate (Ar), l/min	
		Straight polarity	Reverse polarity		Plasma gas	Shielding gas
Laser	400	–	–	66.7	–	8
Microplasma	–	900	500	5	0.3	18
Laser-microplasma	200	1300	600	66.7	10	30

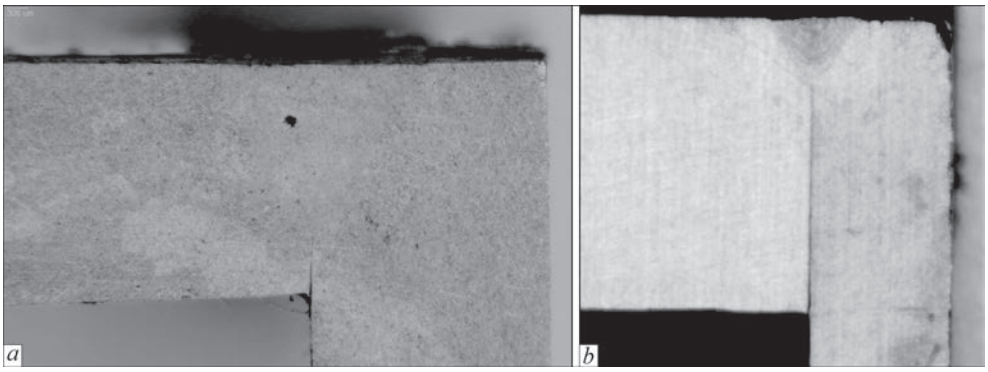

Figure 3. Transverse sections of fillet joints of 7075 alloy, made by laser welding: *a* — at 800 W power and 41.7 ms/s speed; *b* — at 400 W power and 66.7 mm/s speed

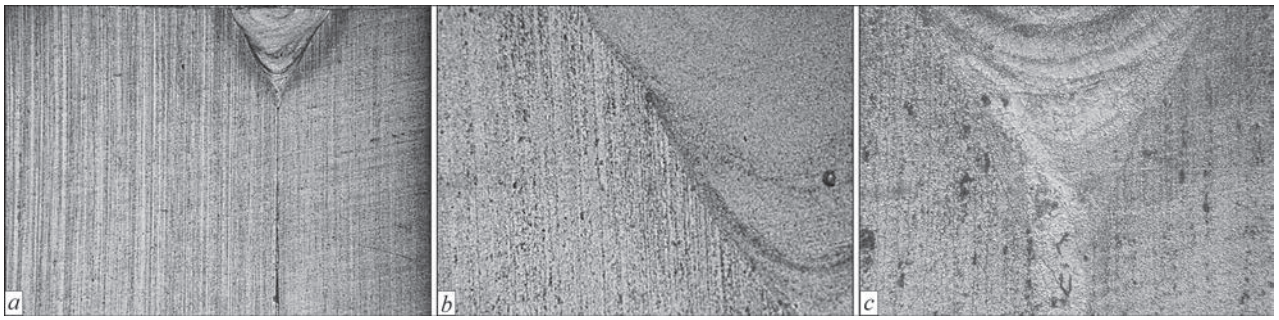

Figure 4. Microstructures of 7005 alloy joints produced by laser welding: *a* — general view of penetration, ×50; *b* — fusion zone; ×250; *c* — stringer precipitates of oxide type in the root zone, ×500

let joints. Preliminary studies on selection of welding mode parameters showed that in order to satisfy the condition of weld formation without caverns (pores), cracks or undercuts on the surface, greater power at lower speed can be used (Figure 3, *a*). This, however, leads to noncompliance with the penetration depth criterion. To meet this criterion, the mode was corrected in combination with the above-mentioned conditions (Figure 3, *b*).

At laser welding of 7005 alloy samples welds of about 0.6 mm (Figure 4, *a*) width and depth were produced. Individual pores of 10–15 μm size were detected in the weld (Figure 4, *b*). The total volume fraction of the defects (V_D) in the weld metal is equal to about 2 %. In the center of weld metal the structure consists of grains of an equiaxed shape of size D_g = 10–15 μm. Closer to the fusion line elongated grains of size D_g = = (5–10)×(15–25) μm (shape coefficient of 2.5–3.0) are observed. Metal stringer precipitates of oxide type of size $l_{Al_2O_3}$ = 15–20 μm were detected in the root part of the weld (Figure 4, *c*). The size of the HAZ is of the order of 225 μm. The size of grains in the HAZ is equal to D_g = (5–10)×(15–50) μm (shape coefficient of 3–5). Below the weld in the welded plate material the graininess is equal to D_g = (4–5)×(10–12) μm on the one side and D_g = (5–6)×(15–20) μm on the other side (shape coefficient of 2.5–3).

HV microhardness in the weld center is equal to 613–624 MPa, in the fusion zone it is ~602 MPa, in the HAZ it rises up to 631–648 MPa (Figure 5).

Results of chemical element distribution in the joint zones are given in Table 3. It is found that a certain redistribution of elements took place in the weld and HAZ metal within the grain volume and in the overall volume of these zones. No alloying element loss was recorded.

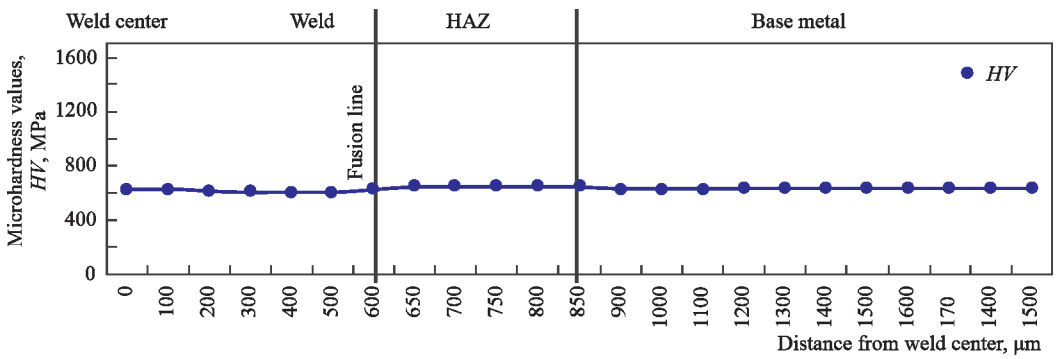

Figure 5. Distribution of *HV* microhardness (100 g load) from the weld axis towards the base metal in 7005 alloy

Table 3. Results of determination of the content of the main elements by the method of analytical scanning electron microscopy in laser-welded joints of 7005 alloy

Investigation zone	Analysis type	Element content, wt.%					
		Al	Mg	Si	Mn	Cu	Zn
Weld metal	General analysis	92.4–96.22	0.5–0.64	0.13–0.52	0.51–0.88	0.01–0.13	2.4–4.38
	Analysis in the grain volume	91.98–95.91	0.02–0.47	0.4–0.7	0.55–0.87	0.17–0.23	3.02–6.53
HAZ	General analysis	94.0–94.72	0.55–0.74	0.53–0.61	0.41–0.54	0.43	3.55–4.81
	Analysis in the grain volume	93.01–93.17	0.69–0.7	0.45–0.48	0.58–0.63	0.07–0.23	4.85–5.13
Base metal	General analysis	94.66–95.02	0.63–0.66	0.43–0.72	0.27–0.35	0.18–0.29	4.05–4.36
	Analysis in the grain volume	90.41–94.79	0.56–0.92	0.51–0.69	0.49–0.95	0.16	3.38–4.17

Welds approximately 0.64 mm wide and approximately 0.74 mm deep were produced at laser welding of 7075 alloy samples (Figure 6, *a*). Individual pores of size d_p = 10–30 μm were detected in the weld. The overall total volume fraction of defects (V_d) in the weld metal is close to 3 %. The structure in the weld metal center is characterized by equiaxed grains of size D_g = 15–25 μm. Closer to the fusion line in the weld metal elongated grains of size D_g = = (5–10)×(20–50) μm (shape coefficient of 2–5) are observed. In the root part of the weld metal, stringer precipitates of oxide type of size $l_{Al_2O_3}$ = 5–15 μm were detected, the arrangement of which follow the shape of the root part (Figure 6, *c*). The width of the HAZ in this joint is equal to 200–240 μm (Figure 6, *a*). Grain size in the HAZ is D_g = (10–15)×(30–50) μm (shape coefficient of 3–3.5). Below the weld in the welded plate material, the graininess is equal to D_g = = (10–25)×(45–50) μm (shape coefficient of 3–3.5). Below the weld in the welded plate material the graininess is D_g = (10–25)×(45–50) μm on the one side and D_g = (5–25)×(20–75) μm on the other.

HV microhardness of the weld metal is equal to 958–980 MPa, in the fusion zone it is 829–936 MPa, in the HAZ it rises on average by 20 % relative to the weld metal and is equal to 1030–1070 MPa (Figure 7).

Results of chemical element distribution in the joint zones are given in Table 4. It was established that a certain redistribution of elements in the grain volume and in the overall volume of these zones occurred in the weld and HAZ metal. No alloying element loss was recorded.

In case of welding 7005 alloy, liquid metal flowing into the slot of the butt being welded is observed in the root part of the weld (Figure 4, *a*). It is attributable to the high fluidity of this alloy, as well as the known effect of formation of spiked structure in the root zone (see, for instance, work [9]). Presence of fine pores in the root part of the weld (Figure 6, *b*) in the case

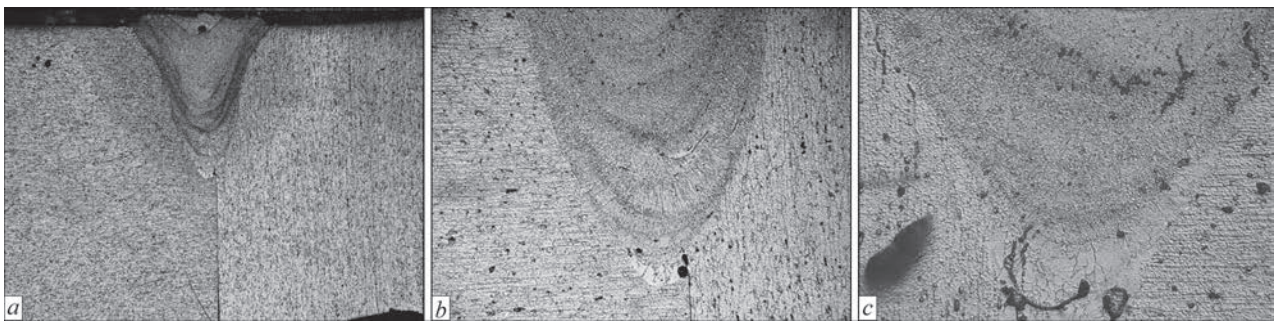

Figure 6. Microstructure of 7075 alloy joints produced by laser welding: *a* — general view of penetration, ×20; *b* — pores in the root zone, ×250; *c* — stringer precipitates of oxide type in the root zone, ×500

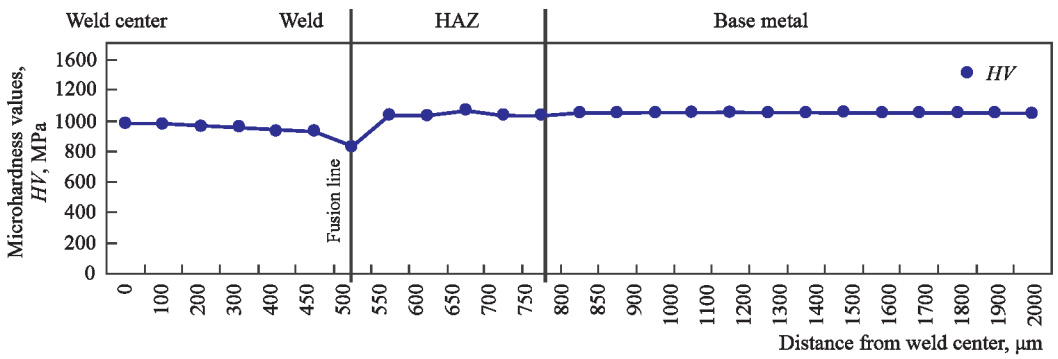

Figure 7. *HV* microhardness distribution (100 g load) from weld axis towards base metal in the joint of 7075 alloy

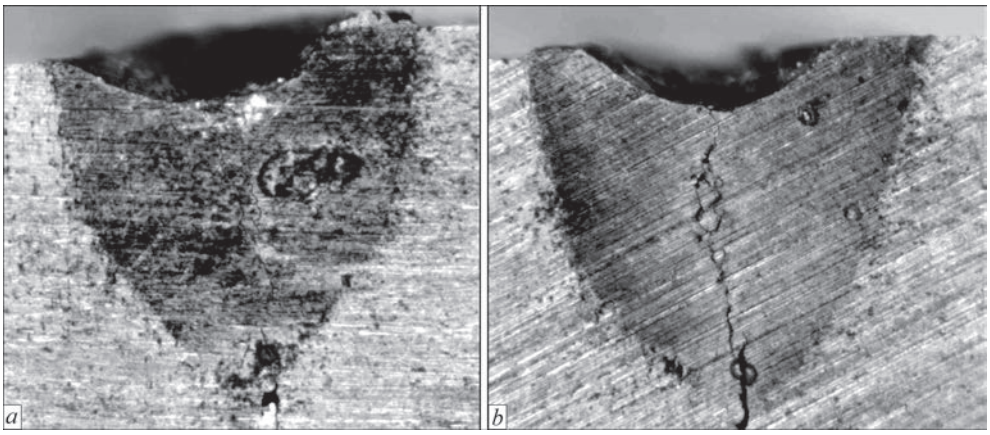

Figure 8. Transverse sections of laser-welded joints of 7075 alloy: *a* — $E \approx 25$ J/mm; *b* — 35

Table 4. Results of determination of the main element content by the method of scanning electron microscopy in laser-welded joint of 7075 alloy

Examined zone	Analysis type	Element content, wt.%					
		Al	Mg	Si	Mn	Cu	Zn
Weld metal	General analysis	89.79–90.17	1.04–1.11	0.47–0.49	0.08–0.14	1.83–2.02	6.05–6.61
	Analysis in the grain volume	89.33–90.27	0.97–1.01	0.42–0.65	0.12–0.17	1.74–2.04	6.17–7.11
HAZ	General analysis	88.79–89.91	1.05–1.16	0.27	0.12	1.2–2.29	6.78–7.38
	Analysis in the grain volume	89.53–89.54	1.13–1.24	0.5–0.71	0.05–0.16	1.72–1.84	6.73–6.84
Base metal	General analysis	89.84–90.66	0.91–1.1	0.45–0.62	0.13–0.27	1.53–1.86	6.02–6.45
	Analysis in the grain volume	89.84–90.41	1.04–1.12	0.55–0.56	0.12–0.17	1.46–1.63	6.41–6.74

of welding 7075 alloy is explained by penetration of air from the butt. Stringer precipitates of oxide film, which are observed in welding both the alloys, are attributable to penetration of fragments of this film into the weld pool, which were left or formed on the edges being welded.

Absence of hot cracks in the samples analyzed above, is attributable to the selected high-speed welding mode, where the heat input was equal to the order of $E = 5$ J/mm (Figure 3, *b*). In case of increase of the heat input up to values $E = 5$–30 J/mm the cracking susceptibility becomes higher. In this value range, variants of producing welds without cracks, for instance at $E \approx 20$ J/mm (Figure 3, *a*), or with crack initiation in the weld root at $E \approx 25$ J/mm (Figure 8, *a*). At heat input above ~ 30 J/mm in case of welding 7075 alloy, there is the risk of hot crack formation (Figure 8, *b*). Such cracks initiate in the weld root zone, also on root defects of pore type, and can extend for its entire height.

In order to remove the defects in the weld root part, it is rational to reduce and stabilize the vapour-gas channel pulsations, which lead to formation of the spike structure. In order to eliminate the risk of formation of stringer precipitates of oxide film, it is rational to break it up in the weld pool, for instance, using an electric arc of reverse polarity. It is known from work [10] that hybrid laser-arc processes promote stabilization of the spike structure of the weld root, and the cathodic cleaning effect at application of laser-plasma welding is known from work [11]. The laboratory stand, shown in Figure 2, *b*, was used to conduct preliminary studies on laser-microplasma welding of 7005 and 7075 alloys. No presence of stringer precipitates of oxide type (oxide film inclusions) in the remelted metal was revealed here. The proneness to porosity in the weld root part decreased. Thus, replacement of laser welding by hybrid laser-microplasma process can be regarded as one of the rather effective ways to eliminate the detected characteristic defects.

CONCLUSIONS

1. It was established that when producing welded joints of aluminium alloys of 7xxx series of 1.5 mm thick sheets by fiber laser welding with partial (nonthrough thickness) penetration to the depth of 0.5–0.7 mm, there is the risk of formation of pores, in particular, in the root zone, stringer precipitates of oxide film in the weld lower part, as well as hot cracks. Elimination of the latter is possible due to decrease of welding heat input below 25–30 J/mm.

2. Weld metal is characterized by an equiaxed fine structure with grain size of 10–15 μm for 7005 alloy and 15–25 μm for 7075 alloy. In the fusion zone the grains have an elongated shape with the coefficient from 2.5 to 3 for 7005 alloy and 2–5 for 7075 alloy. In

the HAZ the grain length is reduced, shape coefficient becomes 3–5 and 3.0–3.5 for 7005 and 7075 alloys, respectively.

3. During performance of laser welding with small (~5 J/mm) values of heat input the microhardness of the welds and HAZ become rather uniform, and close to that of base metal microhardness. For 7075 alloy in the region of the fusion zone a reduction of microhardness to 20 % was observed, which is due to formation of grains of an elongated shape with shape coefficient of 2–5.

4. Elimination of the found drawbacks can be achieved by reducing the vapour-gas channel pulsations with simultaneous improvement of the stability of its existence and introduction of cathode breaking of oxide film.

The work was performed with the support of the following projects:

1. The National Key Research and Development Program of China — in the framework of the strategy «One Belt — One Road» (grant number 2020YFE0205300);

2. Strategic project of the Academy of Sciences of Guangdong Province, (GDAS'Project of Science and Technology Development, 2020GDASYL-20200301001), China;

3. Project of the Guangzhou Economic and Technological Development Zone 2019GH19, China.

REFERENCES

1. Varshney, D., Kumar, K. (2021) Application and use of different aluminium alloys with respect to workability, strength and welding parameter optimization. *Ain Shams Engineering J.*, 12(**1**), 1143–1152. DOI: https://doi.org/10.1016/j.asej.2020.05.013
2. Kang, M., Kim, C. (2017) A review of joining processes for high strength 7xxx series aluminum alloys. *J. of Welding and Joining*, 35(**6**), 79–88. DOI: https://doi.org/10.5781/JWJ.2017.35.6.12
3. Löveborn, D., Larsson, J. K., Persson, K.-A. (2017) Weldability of aluminium alloys for automotive applications. *Physics Procedia*, **89**, 89–99. DOI: https://doi.org/10.1016/j.phpro.2017.08.011
4. Kang, M., Cheon, J., Kam, D.-H., Kim, C. (2021) The hot cracking susceptibility subjected the laser beam oscillation welding on 6XXX aluminum alloy with a partial penetration joint. *J. of Laser Applications*, **33**, 012032. DOI: https://doi.org/10.2351/7.0000319
5. Kim, C.-H., Ahn, Y.-N., Lim, H.-S. (2011) Laser welding of automotive aluminum alloys. *J. of Welding and J.*, 29(**4**), 21–26. DOI: https://doi.org/10.5781/KWJS.2011.29.4.383
6. Zhao, H., White, D.R., DebRoy, T. (1999) Current issues and problems in laser welding of automotive aluminium alloys. *International Materials Reviews*, 44(**6**), 238–266. DOI: https://doi.org/10.1179/095066099101528298
7. Korzhyk, V., Khaskin, V., Grynyuk, A. et al. (2022) Comparison of the features of the formation of joints of aluminum alloy 7075 (Al–Zn–Mg–Cu) by laser, microplasma, and laser-microplasma welding. *Eastern-European J. of Enterprise Technologies*, 115(**1/12**), 38–47. DOI: https://doi.org/10.15587/1729-4061.2022.253378
8. Holzer, M., Hofmann, K., Mann, V. et al. (2016) Change of hot cracking susceptibility in welding of high strength aluminum alloy AA 7075. *Physics Procedia*, **83**, 463–471. DOI: https://doi.org/10.1016/j.phpro.2016.08.048
9. Fetzer, F. (2018) Fundamental investigations on the spiking mechanism by means of laser beam welding of ice. *J. of Laser Applications*, 30(**1**), 012009-1–012009-9. DOI: https://doi.org/10.2351/1.4986641
10. Shelyagin, V.D., Khaskin, V.Yu., Garashchuk, V.P. et al. (2002) Hybrid CO_2-laser and CO_2 consumable-arc welding. *The Paton Welding J.*, **10**, 35–38.
11. Krivtsun, I.V., Shelyagin, V.D., Khaskin, V.Yu. et al. (2007) Hybrid laser-plasma welding of aluminium alloys. *The Paton Welding J.*, **5**, 36–40.

ORCID

V.M. Korzhyk: 0000-0001-9106-8593,
V.Yu. Khaskin: 0000-0003-3072-6761,
A.A. Grynyuk: 0000-0002-6088-7980,
S.I. Peleshenko: 0000-0001-6828-2110,
Yao Yuhui: 0000-0001-7196-1317,
S.G. Hrygorenko: 0000-0003-0625-7010,
V.O. Shcheretskyi: 0000-0002-8561-4444,
O.S. Kushnareva: 0000-0002-2125-1795

CONFLICT OF INTEREST

The Authors declare no conflict of interest

CORRESPONDING AUTHOR

V.M. Korzhyk
E.O. Paton Electric Welding Institute of the NASU
11 Kazymyr Malevych Str., 03150, Kyiv, Ukraine
E-mail: vnkorzhyk@gmail.com

SUGGESTED CITATION

V.M. Korzhyk, V.Yu. Khaskin, A.A. Grynyuk, S.I. Peleshenko, Yao Yuhui, S.G. Hrygorenko, V.O. Shcheretskyi, O.S. Kushnareva (2022) Fibre laser welding of aluminium alloys of 7xxx series (Al–Zn–Mg–Cu) by nonthrough thickness welds. *The Paton Welding J.*, **4**, 19–25.

JOURNAL HOME PAGE

https://pwj.com.ua/en

Received: 28.03.2022
Accepted: 30.06.2022

https://doi.org/10.37434/tpwj2022.04.05

FORMATION OF A JOINT BETWEEN DEPOSITED AND BASE METALS DURING LASER CLADDING OF A NICKEL-BASED POWDER ONTO A COPPER-BASED ALLOY

F. Bourahima[1,2], T. Baudin[2], M. Rege[1], V. Ji[2], F. Brisset[2], A. Zavdoveev[3], A.L. Helbert[2]

[1]Etablissements Chpolansky, 3 Rue Angiboust, 91 462 Marcoussis, France
[2]ICMMO, SP2M, Université Paris-Saclay, UMR CNRS 8182, bât.410, 91405 ORSAY, France
[3]E.O. Paton Electric Welding Institute of the NASU
11 Kazymyr Malevych Str., 03150, Kyiv, Ukraine

ABSTRACT

Laser cladding is an alternative method to other cladding techniques such as Plasma Transfer Arc (PTA) or blowtorch for surface treatment in the glass industry. It aims to produce dense, high-quality coatings on a non-planar surface without affecting its thermal and mechanical properties. In this study, Ni-based coatings were coated onto Cu–Ni–Al substrate using a 3 JET nozzle technique. During laser cladding, good metallurgical bonding is necessary to ensure the further surfacing process technique. A microstructural analysis was conducted, and the mechanical properties were then evaluated with microhardness analysis to link process parameters to coating bonding quality. A calculation of the power attenuation attempts to explain the impact of the powder distribution on the bonding. This work revealed that a chemical dilution zone exists between coating and substrate and is necessary for perfect metallurgical bonding. The heterogeneous bonding, observed through the section, along the curved interface coating/substrate, has been linked to the Gaussian distribution of the powder that attenuates the input power. The attenuated power was measured all along the interface.

KEYWORDS: laser cladding, power attenuation, powder distribution, dilution zone

INTRODUCTION

During glass bottle production, viscous glass is poured into Cupro–Nickel–Aluminum (Cu–Ni–Al) molds at temperatures ranging from 700 to 1200 °C. Cu–Ni–Al or cast-iron glass molds must absorb the high glass temperature to cool it homogeneously, playing the role of thermal exchangers [1]. However, during this process, corrosion or abrasion can appear on the molds' sensitive parts (neck ring and match). Also, thermal fatigue can be observed during the molding cycle. Therefore, it is important to modify the mold surface properties before the production to extend its lifespan. In order to do that, Ni-based or Co-based powder is cladded on those parts. The most famous cladding methods for glass industry are Plasma Transferred Arc (PTA) [2] and blowtorch [1]. But with these techniques, a high Heat Affected Zone (HAZ) is present. It corresponds to a zone belonging to the substrate that has not reached its fusion temperature but underwent a change in its structure due to the process. To avoid that, a pre-heating is operated with those techniques. In mold industry, the aim is to limit this Affected Zone to prevent changes in the substrate thermal properties. To be able to do that, laser cladding is operated instead of former techniques without mold pre-heating.

Laser cladding is an innovative surfacing technique, developed in the 90's [3,4]. It is used to obtain well-bonded high-quality materials, free of pores and cracks without affecting the substrate thermal properties (so, a low HAZ).

Some researchers have investigated the impact of laser cladding on the substrate microstructural change. In most of the studies, the HAZ is observed during laser cladding on cast iron substrates with the appearance of metastable phases like martensite or ledeburite [5, 6].

Balu et al. [7] have operated laser cladding with two kinds of Ni-based powder on Cu substrate with and without pre-heating. They observed that the grain size in the HAZ is high distanced from the interface. It has also been seen that this size increases at low laser scanning speed. Hardness is lower in the HAZ than distanced from the interface. They found that a substrate pre-heating leads to a better bonding due to a larger melting pool and HAZ.

Despite the limited HAZ, laser cladding often induces an area of local chemical dilution between the powder and the substrate. Authors explained that dilution is obtained at the interface when a fusion between the substrate and the coating occur [7–9]. This dilution, dependent on the input laser power [10], has to be restricted in order to avoid a large HAZ but seems necessary to ensure good metallurgical bond-

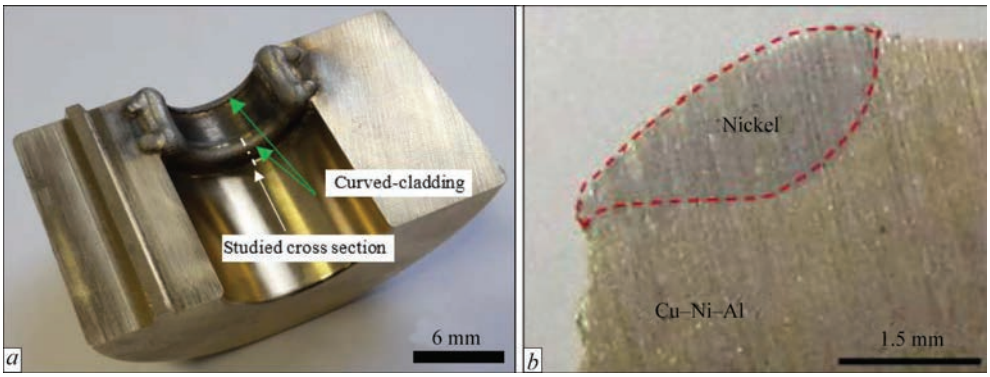

Figure 1. Half of the mold ring after Ni-laser cladding (*a*) and studied cross section (*b*)

ing. Many researches have observed that according to the powder nature, a high power attenuation can appear [11, 12]. There are two ways of describing the dilution (rate) [13]: in geometrical terms, it in calculating the ratio between the melted area (including the HAZ) and the coating area. The second is in metallurgical terms, which consists in measuring the depth of the chemical mixture between the coating and the substrate. Liu et al. [14] present a dilution rate by using the geometrical method during laser cladding of magnesium alloys. According to them, a very low dilution rate prevents from good metallurgical bonding. Using the same definition of the dilution rate, Luo et al. [15] present the same observation during laser cladding of NiCrBSi. Balu et al. [7] used the metallurgical method to measure the dilution rate during laser cladding of Ni-based powder on a Cu substrate. They found that a high dilution can lead to a high HAZ. Pereira et al. [16] observed that during laser cladding of NiCoCrBSi on stainless steel, a very low dilution zone (metallurgical method) at about 2 μm is enough to obtain a perfect bonding without affecting the substrate mechanical properties (no cracking behavior observed). Many authors [17, 18] presented an EDS analysis to measure the dilution between two materials and its components' chemical evolution.

The main challenge in laser cladding on a copper-based substrate is to obtain good bonding despite the low absorptivity of the substrate [19]. Zhang et al. [20] explained that it was impossible to obtain bonding without preheating, so they pre-heated the substrate to 300 °C. It appears that a compromise must be found to respect both the restricted HAZ and the dilution zone needed to guarantee the cohesion between the coating and the substrate. We should bear in mind that this cohesion is crucial to allow further machining of the repaired mold. Moreover, the coating has to be free of cracks and pores to retain a perfect glass surface.

The aim of this study is to obtain a perfect bonding with a limited or non-existent HAZ after cladding of nickel-based material on a Cu–Ni–Al substrate. The novelty in this process is the laser cladding performed without preheating on a curved surface. Also, the high thermal conductivity of the copper-based material is challenging because it can prevent from obtaining the perfect bonding. This can be achieved by identifying the relationship between the dilution zone (existence and thickness) and the bonding quality with regards to the laser process parameters. A microstructural and chemical analysis of the coating/substrate interface will be conducted. Also, microhardness measurements will be presented. The influence of the Gaussian distribution of Ni powder on the laser power attenuation, and thus on the bonding, will be discussed.

MATERIALS AND EXPERIMENTAL TECHNIQUES

Laser cladding consists in melting an injected powder with a very thin surface layer on the substrate by a laser beam to produce a metallurgical bonding. During this study, a 4KW Nd:YAG laser with a wavelength of 1030 nm was used. An optical fiber with a diameter of 600 μm was used for guiding the beam. Ni powder was injected coaxially into the laser beam [21]. A cross-section of the Cu–Ni–Al mold of the bottle ring is shown in Figure 1, *a* after cladding. Figure 1 *b* describes the typical cross-section that has been metallurgically studied.

During the process, the interaction distance, fs, between the laser and the powder is considered (Figure 2).

At the focal plane (position B), the powder flow follows a Gaussian distribution. This has been proved by many research studies [22–24]. In the present study, the Gaussian distribution has been centered at the midpoint of the mold curved surfaces of the samples.

The chemical compositions of the powder and the substrate are listed in Table 1.

The process parameters used during this study are presented in Table 2. These samples are extracted using Taguchi design of experiment. Only samples with a partial or perfect bonding have been selected.

To be characterized, samples were mechanically polished using SiC papers and then diamond polished

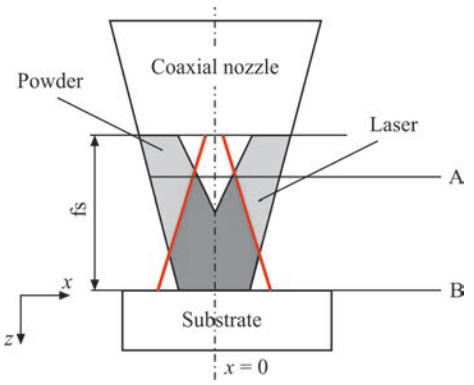

Figure 2. Powder distribution according to the focal position fs [19]

to 1 μm for Optical Microscopy (OM), Scanning Electron Microscopy (SEM) and Energy Dispersive Spectroscopy (EDS) analyses. To operate Electron Backscatter Diffraction (EBSD), an extra OPS polishing was done. Vickers hardness tests were performed on the cross-section, along a line perpendicular to the coating surface with a 10-gf load for 15 seconds. The measurements were taken from either side of the interface for all the 6 samples.

RESULTS AND DISCUSSION

MICROSTRUCTURE FEATURES AND ASSOCIATED CHEMICAL AND MECHANICAL PROPERTIES

Figure 3 describes the three different kinds of bonding behavior that can be observed after laser cladding of Ni-based powder on a Cu–Ni–Al substrate: perfect bonding (Figure 3, *a*), partial bonding (Figure 3, *b*) where the bonding is partially present at the interface and no bonding (Figure 3, *c*). A bonding is considered partial when 15 % bonding default is observed in the coating/substrate interface.

Figure 4 shows the SEM-BSE (Back-Scattered Electrons) analysis of the CNC 5 and CNC 6 samples (see Table 2). Figure 4*a* shows that CNC 5 presents perfect bonding (case of Figure 3, *c*) whereas Figure 4b shows a sample (CNC 6) with a discontinuous bonding (Figure 3, *b*). Indeed, in the curved center, there is a lack of bonding. No analyses have been performed on samples with no bonding (Figure 3, *a*) since the clad is easily separated from the substrate.

For both samples, the substrate is composed of a dendritic matrix. No heat affected zone (HAZ) seems to be present in the substrate because no microstructure modification is noticeable close to the interface. Concerning the Ni deposit, elongated grains are observed along solidification direction for both cases. Small grains can be seen in the coating close to the interface and at the extreme surface.

Figure 5 shows an EBSD analysis of the microstructure and texture around the interface (black squares in Figure 4, *a*, *b*) for both samples (perfect or partial bonding) in order to observe the differences according to the bonding quality.

It can be observed that microstructure is very similar in both cases (Figure 5, *a*, *b*).The solidification features are in accordance with the literature [25–28].

Table 1. Chemical compositions of the substrate and powder

Elements (wt.%)	Fe	Mn	Al	Ni	Zn	Pb	Sn	Si	Cu	B	Cr	C
Cu–Ni–Al	<1	0.5	8.5	15	8	<0.1	0.15	1	Bal	–	–	–
Ni powder	1	0.1	–	Bal	–	–	–	2.5	–	1.7	0.3	0.5

Table 2. Process parameters

Sample	Power, W	Speed, mm/s	Powder feeding rate, g/min	Spot diameter, mm
CNC 1	2400	6.5	26.5	4
CNC 2	2600	10	24.5	3
CNC 3	2800	6.5	32.5	3
CNC 4	2800	8.5	24.5	4
CNC 5	3200	8.5	28.5	3
CNC 6	3200	10	30.5	4

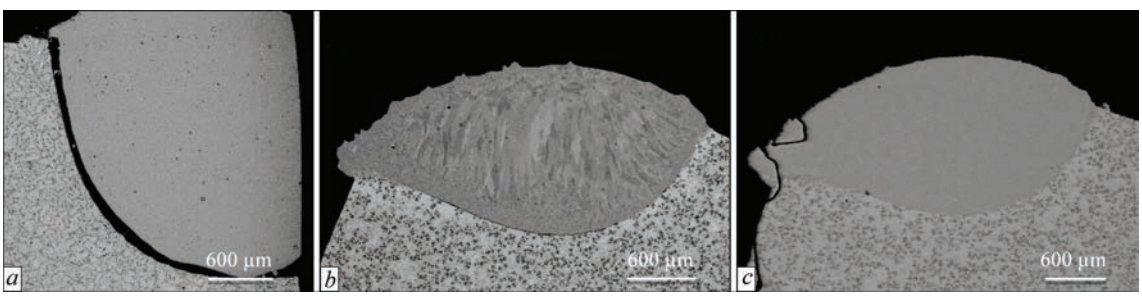

Figure 3. Three kinds of bonding behavior: *a* — no bonding; *b* — partial bonding; *c* — perfect bonding

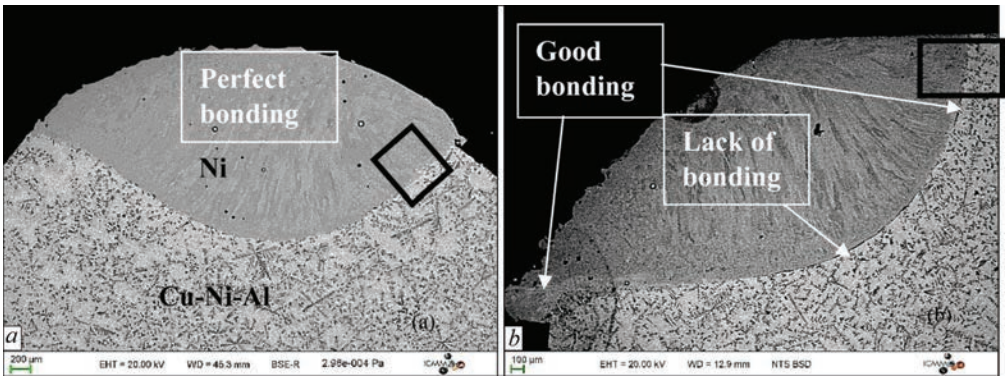

Figure 4. Typical microstructure of the cross-section of the samples: *a* — CNC 5 with good bonding; *b* — CNC 6 with partial bonding obtained by SEM-BSE

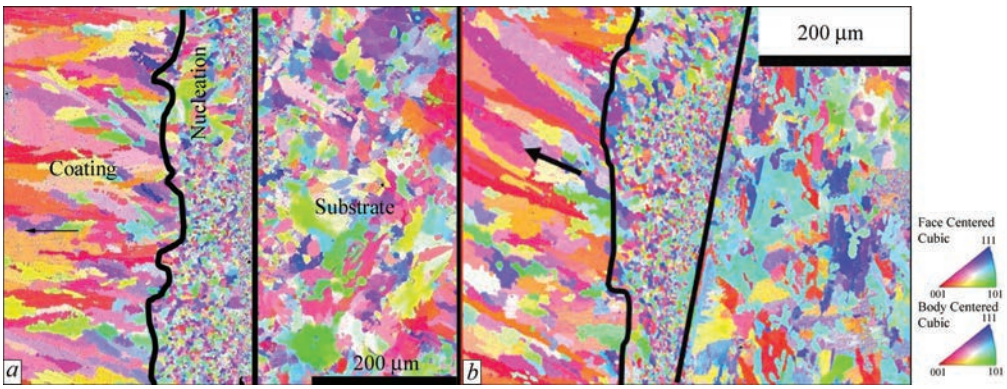

Figure 5. Crystallographic axes parallel to the solidification direction (black arrows): *a* — EBSD analysis of the black square area in Figure 4, *a*, *b*

A nucleation phase, characterized by small equiaxed grains, is evidenced at the interface, then a columnar growth directed mainly parallel to the <001> direction of the dendrites is observed (Figure 5, *a*). So, the bonding quality does not change the solidification behavior during laser cladding.

A SEM-EDS analysis is presented (Figure 6) to observe the chemical impact of the laser cladding at the interface nucleation/substrate.

In the Figure 6, *a*, *b*, deconstruct dendrites from the substrate are observed in a mixed zone at the coating/substrate interface delimited by white lines. Also, the Figure 6, *c* clearly shows a local chemical mixture where copper seems to be replaced by nickel over a thin layer of the substrate. This can be the consequence of a local fusion of the substrate and correspond to the dilution zone that has been reported in the literature [17, 26]. Apart from this area, there are no discernible chemical changes in the substrate or the Ni coating. So, no HAZ can be chemically observed in this study.

A measurement of the dilution zone thickness was made by chemical analysis from the coating to the substrate (Figure 7).

A diminution of the Ni element from the coating to the substrate can be observed. At the same time, the Cu composition progressively increases. Overall, Ni is at around 96 % in the coating, then decreases down to 40 % close to the interface and stays below 10 % in the substrate matrix except inside the dendrites where the Ni increases to 39 %. The dendrites also present a higher level of Al (the high concentration of Ni and Al inside the dendrites is in accordance with Figure 6).

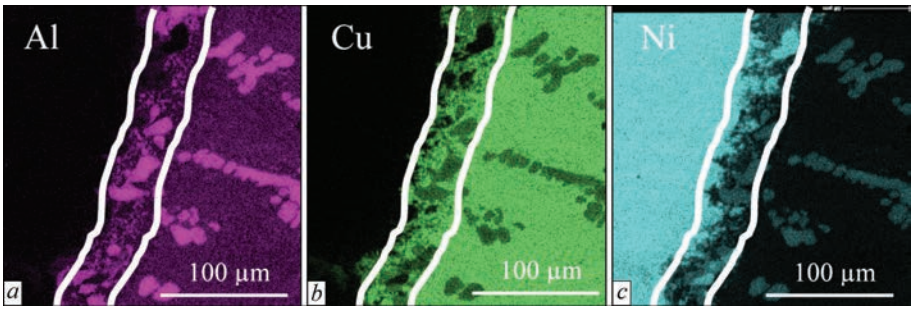

Figure 6. EDS maps of the principal chemical elements composing the deposit and the substrate of sample CNC6: *a* — Al; *b* — Cu; *c* — Ni

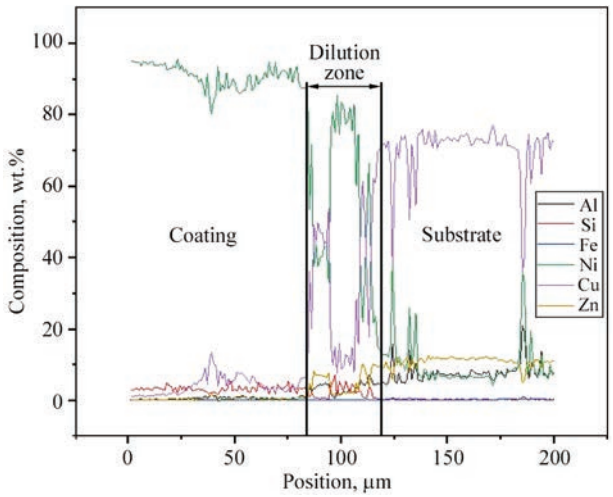

Figure 7. Chemical composition of the dilution zone from the coating to the substrate (sample CNC 6)

The dilution zone exhibits a chemical mixture over about 35 µm for this sample.

Figure 8 shows the hardness measurements through the interface for four typical features of the microstructure: the columnar zone of the coating, the nucleation zone, the dilution zone, and the substrate.

It can be observed from Figure 8 that the micro-hardness of the dilution zone increased to 618 *HV*. The similar results was observed by Pan et al. [27] when cladding Fe-based powder on a stainless steel substrate in their dilution zone. This high hardness in the dilution zone could be explained by the formation of an eutectic of Ni–Ni_3B due to the low ratio of Si/B (≈1.3) in this area as described by Hemmatie et al. [28]. Indeed, they mention that this compound is of high hardness. In the coating and the substrate, the values are not higher than 317 *HV*. This hardness does not indicate the presence of the HAZ in the substrate. No increase of the hardness is noticed in the nucleation area despite the presence of small grains. In fact, the Hall and Petch law which describes that the hardness is higher when the grain size is lower [29]. But this couldn't be verified is the present work.

Since the dilution zone can be quantified using the EDS analysis it could be interesting to observe its evolution along the curved interface in order to corroborate its existence/thickness with the metallurgical bonding quality.

DILUTION ZONE THICKNESS ALONG THE CURVED INTERFACE

To state if the discontinuous bonding along the interface in the studied section is linked to the chemical dilution presence or thickness, a protocol of systematic DZ quantification has been implemented across the section of all samples and is presented in Figure 9. Five lines separated from each other by an angle of 22.5° along which the chemical composition have been measured from the coating to the substrate within 400 µm, and where the DZ depth has been determined. This method allows to plot the DZ evolution along the curved interface (Figure 9).

Figure 9 reveals that the DZ evolution is the same across the section for all the samples studied. On the zones a and e (the edges), the DZ depth is maximum (from 25 to 175 µm according to the cladding parameters). It decreases at lower levels (b and d zones) to between 3 and 21 µm. Then at the center of the curve (c zone) this DZ is minimum (zero in the case of no bonding). Moreover, for all the studied samples, the bonding is lower at the center of the curved section. Therefore, it is possible to draw a direct connection between DZ depth and bonding quality. Indeed, the deeper the DZ, the better the bonding will be. The discontinuous bonding is well highlighted by the DZ evolution along the curve of the cross-section. It is important to understand what phenomenon leads systematically to a weaker chemical dilution at the section curve center during laser cladding, as a function of process parameters.

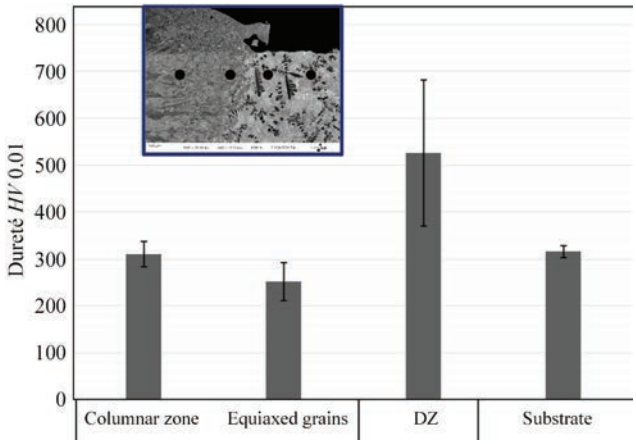

Figure 8. Hardness measurements corresponding to the characteristic features encountered from the coating to the substrate (black points)

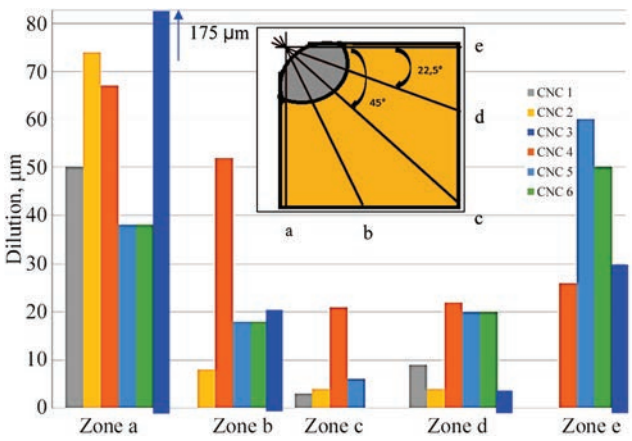

Figure 9. Measurement of the DZ depth over the entire cross-section and DZ depth along the five black lines for all the samples

POWER ATTENUATION

It is well known in the laser cladding process that powder particles contribute to attenuate the incident laser power. Obviously for full consideration it is necessary to calculate the total heat balance of laser surfacing using filler powder, the total amount of heat released by the laser is spent on heating and melting the filler powder, heating the base metal before melting and maintaining the weld pool in a liquid state (the useful part of the heat), as well as radiation into the surrounding space (including as a result of reflection from powder particles, depending on its reflectivity) and heat removal to the base metal (heat loss). The thermal efficiency of the laser surfacing process and the parameters of its regime depend on these indicators: laser power, the amount of powder supplied per unit time, its granulometric composition, etc. [30, 31]. This is complex calculation and for simplification of the description in current research we have considered only the effect of the powder particles (i.e. filler powder). Tabernero et al. [32] have described the impact of a shadow of particles during the interaction of the laser and the powder while cladding is in progress. They have assessed the attenuation undergone by the beam and characterized the density of energy that reaches the surface of the substrate. They were able to perform this calculation with a computational fluid dynamics (CFD) model, which has been experimentally validated. Moreover, the present authors used the calculation of the attenuated power to determine the minimum power necessary to ensure an accurate clad/substrate bonding [26]. Nevertheless, the local attenuation due to the Gaussian powder distribution has not been studied along the curve section.

El Cheikh et al. [23] have discovered that at the focal position, fs, presented in Figure 2, a Gaussian distribution of powder can be observed. Qi et al. [33] have proposed an equation of the powder distribution $N(x, y)$ depending on the radial distance x and the axial distance z in the case of a coaxial nozzle as shown:

$$N(x,z) = N_{\max}(z)\exp\left(-2x^2 / R^2\right), \quad (1)$$

where N_{max}, m^{-3} the peak concentration at the center of powder flow ($x = 0$); x, mm the radial distance; R, mm the powder stream.

To understand how the power is impacted, the Beer Lambert Law can be applied [33, 34]:

$$P'_z(x,z) = P_z(x)\exp(-\alpha SNz), \quad (2)$$

where P'_z W the power attenuated by the powder flow, P'_z W the initial input power during laser cladding; S mm^2 the particle section and α a factor which considers phenomena like the scattering effect, plasma generation. α was obtained from an experiment of the attenuated power during laser cladding. A power meter is placed under an optically neutral glass to protect it from the powder injected. During the test, an air flow was injected horizontally in order to deflect the projected powder. As an example, for an incident measured power of 1916 W, the measured attenuated power was 1498 W for a PFR of 28.5 g/min. This led to adjusting the α coefficient at a value of 6 (this result is in accordance with literature [32]). If α is equal to 1, the attenuation is only due to particle shadow. The present value of 6 indicates that other phenomena (scattering effect, plasma generation) also contribute to the power attenuation.

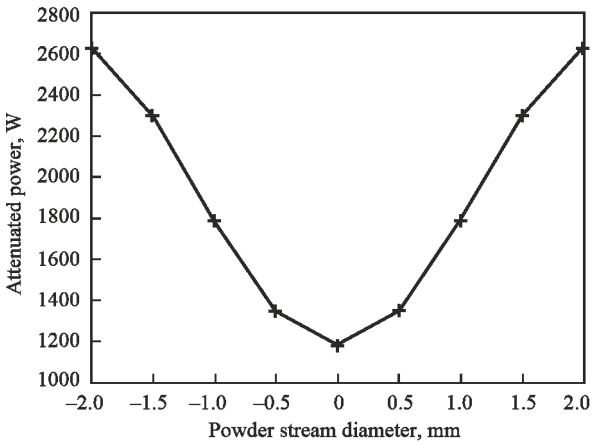

Figure 10. Distribution of the power attenuation on the substrate ($x = 0$ is the focal point) for an input laser power of 2800 W

By inputting the powder distribution on each position of x it is possible to observe the power attenuation on the radial distance for an incident power of 2800 W as an example (Figure 10).

Figure 10 indicates that, at the center of the powder flow (the focal point fs, Figure 2), the power is attenuated from 2800 to 1200 W. At the center of the powder flow ($x = 0$), 57 % of the power is lost due to the powder flow (absorbed or reflected). So, only 43 % is available for the fusion. Moreover, given that the absorptivity of Cu-based materials is about 0.06, only 72 W remains to reach the substrate (and probably melt it). Since the focal plane of the powder flow corresponds to the center of the mold curved surface, it can be assumed that this shadow effect explains the lack of dilution DZ observed at this position. Therefore, this phenomenon may be at the origin of the absence of bonding for some cladding conditions with too weak incident laser power.

A LINK BETWEEN POWER ATTENUATION, DILUTION AND HAZ

No HAZ was observed here when laser cladding on a Cu-based substrate. But the heterogeneous dilution in the mold's curved section can lead to a lack of bond-

ing at the curved center and induce the coating fall out during machining [1]. In the meantime, on the edges (according to the input laser power), less powder generates more power available for the interface fusion. According to the substrate composition, a high HAZ can be generated and induces a cracking behavior due to the high hardness as it was observed in previous researches conducted by the authors during laser cladding on cast iron [35].

CONCLUSION

Ni-based powder was deposited by laser cladding on a Cu-based substrate with a curved surface. The cladding process parameters were widely explored in order to verify the bonding quality of the clad to the substrate. Three kinds of metallurgical bonding have been noted: lack of bonding, partial bonding or perfect bonding. In addition, a constant lack of bonding is observed in the center of the substrate curved surface. Moreover, the chemical dilution depth between Ni and Cu was measured at the interface clad/substrate depending on process parameters. It appears that the dilution depth is also lower at the same location of the curved surface. This could be explained by the Gaussian distribution of the powder flow around this point. Indeed, at the curved center the powder density is at maximum, so the input laser power is significantly attenuated. Less energy is then available for the substrate to melt and to ensure a perfect metallurgical bonding. The attenuated power evolution moving away from this central point would explain the discontinuous bonding along the interface in the cross-section. As it was mentioned above, a compromise was found in the present work to ensure a minimal dilution (DZ) in the curved center without affecting the based material properties (limit the HAZ). This optimization can correspond for example to a laser power of 3200 W with a PFR of 28.5 g/min and a scanning speed of 8.5 mm/s.

ACKNOWLEDGMENTS

The authors wish to thank C. Aboud, N. Barbosa and C. Lafarge from the ETS CHPOLANSKY for their help in the sample elaboration by laser cladding and their great skill in the field of this technology applied to non-planar surfaces. This research was supported by the ANRT (French National Agency for Research and Technology) and ETS Chpolansky.

REFERENCES

1. Rege, M., Van Linden, S. (2016) *Stage de formation aux techniques de rechargement dans l'industrie verrière*, Marcoussis.
2. Oberländer, B.C., Lugscheider, E. (1992) Comparison of properties of coatings produced by laser cladding and conventional methods. *Mater. Sci. Technol. (United Kingdom)*, **8**, 657–665. DOI: https://doi.org/10.1179/mst.1992.8.8.657.
3. Steen, W.M., Mazumder, J. (2010) *Laser Material Processing*. 4th Ed., Springer.
4. Ryabtsev, I.A., Perepletchikov, E.F. (1992) *Properties of alloys based on Fe, Ni, Co, deposited by laser-powder method. Sat. on Deposited metal. Composition, structure and properties*. Kyiv, E.O. Paton Electric Welding Institute of the NASU, 23–26.
5. Arabi Jeshvaghani, R., Jaberzadeh, M., Zohdi, H., Shamanian, M. (2014) Microstructural study and wear behavior of ductile iron surface alloyed by Inconel 617. *Mater. Des*., **54**, 491–497. DOI: https://doi.org/10.1016/j.matdes.2013.08.059.
6. Liu, H., Hao, J., Han, Z. et al. (2016) Microstructural evolution and bonding characteristic in multi-layer laser cladding of NiCoCr alloy on compacted graphite cast iron. *J. Mater. Process. Technol*., **232**, 153–164. DOI: https://doi.org/10.1016/j.jmatprotec.2016.02.001.
7. Balu, P., Rea, E., Deng, J. (2015) Laser cladding of nickel-based alloy coatings on copper substrates. In: *Proc. of SPIE,* **9657**, 1–10. DOI: https://doi.org/10.1117/12.2175966
8. Saqib, S., Urbanic, R.J., Aggarwal, K. (2014) Analysis of laser cladding bead morphology for developing additive manufacturing travel paths. *Procedia CIRP*, **17**, 824–829. DOI: https://doi.org/10.1016/j.procir.2014.01.098.
9. Tao Y.F., Li J., Lv Y.H., Hu L.F. (2017) Effect of heat treatment on residual stress and wear behaviors of the TiNi/Ti-2Ni based laser cladding composite coatings. *Opt. Laser Technol.*, **97**, 379–389. DOI: https://doi.org/10.1016/j.optlastec.2017.07.029.
10. Kim, C.K., Choi, S.G., Kim, J.H. et al. (2020) Characterization of surface modification by laser cladding using low melting point metal. *J. Ind. Eng. Chem.*, **87**, 54–59. DOI: https://doi.org/10.1016/j.jiec.2020.03.010.
11. Kumar, S., Roy, S. (2006) The effect of Marangoni-Rayleigh-Benard convection on the process parameters in blown-powder laser cladding process-A numerical investigation, Numer. *Heat Transf. Pt A Appl.*, **50**, 689–704. DOI: https://doi.org/10.1080/10407780600605286.
12. Rienstra, S.W., Chandra, T. (2001) Analytical approximations to the viscous glass-flow problem in the mould-plunger pressing process, including an investigation of boundary conditions. *J. Eng., Math*. **39**, 241–259. DOI: https://doi.org/10.1023/A:1004883310709 CITATIONS.
13. Toyserkani, E., Amir, K., Stephen, C. (2006) *Laser Cladding, CRC PRESS.*
14. Liu, J., Yu H., Chen, C. et al. (2017) Research and development status of laser cladding on magnesium alloys: A review. *Opt. Lasers Eng.*, **93**, 195–210. DOI: https://doi.org/10.1016/j.matdes.2014.01.077.
15. Luo, X., Li, J., Li, G.J. (2015) Effect of NiCrBSi content on microstructural evolution, cracking susceptibility and wear behaviors of laser cladding WC/Ni–NiCrBSi composite coatings. *J. Alloys Compd*., **626**, 102–111. DOI: https://doi.org/10.1016/j.jallcom.2014.11.161.
16. Pereira, J.C., Zambrano, J.C., Rayón, E. et al. (2018) Mechanical and microstructural characterization of MCrAlY coatings produced by laser cladding: The influence of the Ni, Co and Al content. *Surf. Coatings Technol.*, **338**, 22–31. DOI: https://doi.org/10.1016/j.surfcoat.2018.01.073.
17. Adesina O.S., Obadele B.A., Farotade G.A. et al. (2020) Influence of phase composition and microstructure on corrosion behavior of laser based Ti–Co–Ni ternary coatings on Ti–6Al–4V alloy. *J. Alloys Compd.*, **827**, 1–11. DOI: https://doi.org/10.1016/j.jallcom.2020.154245.
18. Wang, S., Liu, C. (2019) Real-time monitoring of chemical composition in nickel-based laser cladding layer by emission spectroscopy analysis. *Materials (Basel)*, **12**, 1–15. DOI: https://doi.org/10.3390/ma12162637.

19. Babinets, A.A., Ryabtsev, I.O., Lentyugov, I.P. et al. (2020) Problems and prospects of surfacing of copper and copper parts by wear-resistant layers (Review). *The Paton Welding J.*, **5**, 15–23. DOI: https://doi.org/10.37434/tpwj2020.05.03
20. Zhang, Y., Tu, Y., Xi, M., Shi, L. (2008) Characterization on laser clad nickel based alloy coating on pure copper. *Surf. Coatings Technol.*, **202**, 5924–5928. DOI: https://doi.org/10.1016/j.surfcoat.2008.06.163
21. F. Bourahima, A. Helbert, M. Rege, V. Ji, D. Solas, et al. (2019) Laser cladding of Ni based powder on a Cu–Ni–Al glassmold: Influence of the process parameters on bonding quality and coating geometry. *J. of Alloys and Compounds*, Elsevier, **771**, 1018–1028. DOI: https://doi.org//10.1016/j.jallcom.2018.09.004
22. Ferreira, E., Dal, M., Colin, C. et al. (2020) Experimental and numerical analysis of gas/powder flow for different LMD nozzles. *Metals (Basel)*, **10**, 1–20. DOI: https://doi.org/10.3390/met10050667.
23. Cheikh, H. El, Courant, B., Branchu, S. et al. (2012) Analysis and prediction of single laser tracks geometrical characteristics in coaxial laser cladding process. *Opt. Lasers Eng.*, **50**, 413–422. DOI: https://doi.org/10.1016/j.optlaseng.2011.10.014.
24. Pouzet, S., Peyre, P., Gorny, C. et al. (2016) Additive layer manufacturing of titanium matrix composites using the direct metal deposition laser process. *Mater. Sci. Eng. A*, **677**, 171–181. DOI: https://doi.org/10.1016/j.msea.2016.09.002.
25. Song, B., Yu, T., Jiang, X. et al. (2020) The relationship between convection mechanism and solidification structure of the iron-based molten pool in metal laser direct deposition. *Int. J. Mech. Sci.*, **165**, 1–14. DOI: https://doi.org/10.1016/j.ijmecsci.2019.105207.
26. Pereira, J.C., Zambrano, J.C., Tobar, M.J. et al. (2015) High temperature oxidation behavior of laser cladding MCrAlY coatings on austenitic stainless steel. *Surf. Coatings Technol.*, **270**, 243–248. DOI: https://doi.org/10.1016/j.surfcoat.2015.02.050.
27. Pan, C., Li, X., Zhang, R. et al. (2021) Research on microstructural and property evolution in laser cladded HAZ. *Surf. Eng.*, **37**, 1514–1522. DOI: https://doi.org/10.1080/02670844.2021.1929737.
28. Hemmati, I., Ocelík, V., De Hosson, J.T.M. (2013) Effects of the alloy composition on phase constitution and properties of laser deposited Ni–Cr–B–Si coatings. *Phys. Procedia.*, **41**, 302–311. DOI: https://doi.org/10.1016/j.phpro.2013.03.082.
29. Gourges-Lorenzon, A.-F. (1972) Durcissement et renforcement des materiaux. *Matériaux Pour l'ingénieur*, 159–170.
30. Gladkiy, P.V., Perepletchikov, E.F., Ryabtsev, I.A. (2007) *Plasma welding*. Kyiv.
31. Kuskov, Yu.M., Ryabtsev, I.A., Kuzmenko, O.G., Lentyugov, I.P. (2020) *Electroslag technologies for surfacing and recycling of metal and metal-containing wastes*. Kyiv.
32. Tabernero, I., Lamikiz, A., Martínez, S. et al. (2012) Modelling of energy attenuation due to powder flow-laser beam interaction during laser cladding process. *J. Mater. Process. Technol.*, **212**, 516–522. DOI: https://doi.org/10.1016/j.jmatprotec.2011.10.019.
33. Qi, H., Mazumder, J., Ki, H. (2006) Numerical simulation of heat transfer and fluid flow in coaxial laser cladding process for direct metal deposition. *J. Appl. Phys.*, **100**, 1–11. DOI: https://doi.org/10.1063/1.2209807.
34. Peyre, P., Aubry, P., Fabbro, R. et al. (2008) Analytical and numerical modelling of the direct metal deposition laser process. *J. Phys. D. Appl. Phys.*, **41**, 1–10. DOI: https://doi.org/10.1088/0022-3727/41/2/025403.
35. Bourahima, F., Helbert, A., Ott, F. et al. (2021) *Multi-scale characterization by neutronography and electron diffraction of Ni coating on Cu–Ni–Al or cast-iron glass molds after laser cladding*. Trans Tech Publ. Ltd., **1016**, 297–302.

ORCID

F. Bourahima: 0000-0003-2459-7799,
T. Baudin: 0000-0002-6765-360X,
V. Ji: 0000-0003-1979-7323
F. Brisset: 0000-0003-0952-2748,
A. Zavdoveev: 0000-0003-2811-0765
A.L. Helbert: 0000-0003-1679-9569

CONFLICT OF INTEREST

The Authors declare no conflict of interest

CONFLICT OF INTEREST

The Authors declare no conflict of interest

CORRESPONDING AUTHOR

A. Zavdoveev
E.O. Paton Electric Welding Institute of the NASU
11 Kazymyr Malevych Str., 03150, Kyiv, Ukraine.
E-mail: paton39@ukr.net

SUGGESTED CITATION

F. Bourahima, T. Baudin, M. Rege, V. Ji, F. Brisset, A. Zavdoveev, A.L. Helbert (2022) Formation of a joint between deposited and base metals during laser cladding of a nickel-based powder onto a copper-based alloy. *The Paton Welding J.*, **4**, 26–33.

JOURNAL HOME PAGE

https://pwj.com.ua/en

Received: 22.03.2022
Accepted: 30.06.2022

APRIL 24, 2014 A sculptor under the pseudonym of TEJN installed one of his latest sculptures — «Reaching for Freedom». TJEN is the pseudonym of a contemporary Danish artist, who began his artistic work as a street artist in 2007. Making his works from metal and using welding, he became famous owing to unsanctioned creation of sculptures. Without permission of the authorities, the artist welds or chains the monument, wherever he wants. Later on the sculptures began to be returned to their places as architectural monuments. In his work the sculptor uses welding, cutting, surfacing and other methods of metal treatment. Today his works are often displayed at prestigious exhibitions.

https://doi.org/10.37434/tpwj2022.04.06

ANALYSIS OF MODERN EXPERIENCE IN DEVELOPMENT OF SEALING COATINGS FOR PARTS OF GAS TURBINE ENGINES (REVIEW)

Yu.S. Borysov, N.V. Vihilianska, O.M. Burlachenko, L.P. Olevska, V.M. Lopata

E.O. Paton Electric Welding Institute of the NASU
11 Kazymyr Malevych Str., 03150, Kyiv, Ukraine

ABSTRACT

In the work, the experience in development of sealing thermal coatings for parts of gas turbine engines was analyzed. It was found that the tasks of developing compositions and technologies of thermal spraying of sealing coatings intended to provide the optimal radial clearance between components of stator and rotor in order to reduce the consumption of technological fuel and improve the efficiency coefficient of engines, are relevant. The principles of optimizing the composition of sealing coating material were described. They consist mainly in the combination of ease of plunging a blade into coating with resistance to erosion wear, which provides the operation efficiency of coating with its fatigue life. The temperature modes of operation of sealing coatings in different sections of gas turbine engine were determined. For spraying of sealing coatings applying thermal methods, composite powders are used, the composition of which corresponds to the concept of metal solid lubricant. As a metal component, Ni, AlSi, Ni- and Co-alloys are used and as a solid lubricant, graphite, hexagonal boron nitride, betonite and polyester are used. For high-temperature sections of turbines, a combination of a stabilized zirconium oxide with hexagonal boron nitride and polyester is used. The composition of these combinations determines the temperature zone of their use, related to the working conditions of compressor or turbine.

KEYWORDS: sealing coating, thermal spraying, matrix, solid lubricant, abrasion, erosion resistance, compressor, turbine

INTRODUCTION

Gas turbine engines (GTE) are the main primary engines of powerful compressor and pumping units, the reliability and efficiency of which is paid special attention. Increasing the efficiency of modern GTE is one of the important tasks of modern engine construction. During their manufacture, special attention has always been paid to increasing the efficiency and, accordingly, reduction in fuel consumption. One of the basic parameters of an engine affecting its efficiency, are radial clearances between working blades of turbine (compressor) and stator parts (super rotor inserts) [1]. According to the carried out studies, an increase in relative radial clearance by 1 % leads to a decrease in engine efficiency by about 3 % and fuel consumption by almost 10 % [2]. Since the size of radial clearance between rotor and stator significantly affects the efficiency of turbine, its reduction allows solving this problem in the least expensive way.

This can be achieved by creating a minimal, close to zero radial clearance between the ends of blades and the engine casing and keeping it at a set level throughout the whole engine operating life. However, during operation as a result of the action of gas flow temperatures, deformation of the casing and blades, vibrations of rotor and casing during operation under off-design conditions, twisting of rotor, etc., often a contact of the end part of blades with the engine casing arises. As a result, a significant wear of blades appears, which results in an increase in a radial clearance of the flow tract during operation of the engine, which leads to a decrease in efficiency, reduction in the operating life of blades and sometimes to fracture of parts being in contact [3].

One of the ways of solving the problems of reducing the radial clearance between rotor and stator and increasing the efficiency of GTE turbine are measures based on the modernization of designs of turbomachines, blades, preliminary planned creation of an initial radial clearance, which allows avoiding touching the ends of blades and turbine casing in the operation process. At the same time, the problem of minimizing gas leakage is solved by reducing the residual rotor imbalance, the use of brush seals and compensators. Such measures allow increasing the efficiency of engines, but require new design and technological studies. This leads to a change in GTE design, increasing its cost and cannot be implemented in already designed engines in operation [4].

The most rational method of reducing the size of radial clearance is to use various kinds of sealing run-in coatings, which are easily abrased in the course of operation when interacting with the tips of blades or crests of labyrinths without their further fracture. Sealing or abradable coatings are used in GTE in aircraft, power engineering and gas-pumping units.

Thermal spraying methods allow depositing sealing coatings (instead of inserts from sealing mate-

rials), that are so pliable that the edge of a blade or a labyrinth can easily cut into their layer, but at the same time strong enough to withstand the pressure of the gas flow, including at high temperatures.

The aim of the work is to analyze literature data on the conditions of the work, the requirements for the properties of materials, experience in development of compositions of sealing thermal coatings on GTE parts.

FUNCTIONAL PURPOSE OF SEALING COATINGS

The need in creating new sealing materials for GTE is caused by the requirements to reduce the specific fuel consumption. One of the most important tasks set before the developers of challenging GTE, is providing minimum admissible clearances between blades and casings of compressor and turbine to reduce working gas leaks. However, reducing the size of a radial clearance is associated with an increase in wear of blades at the ends and the risk of their breakage as a result of contact with stator.

To avoid breakage and wear of blades, special sealing coatings are developed, which have a number of physical-mechanical and tribotechnical characteristics. The scheme of using sealing coating to adjust clearances in GTE is shown in Figure 1 [5].

The efficiency of using sealing coatings is characterized by contact interaction of rotor and stator of GTE. Ideally, when as a result of interaction of rotor parts with an abradable coating, only the latter is worn, when rotor is shifted, a clearance with an area that is 3 times smaller than in the case of using wear-resistant coating is formed. Since gas consumption is directly proportional to the leakage area, it is obvious that the leakage of gas in the case of using abradable sealing coatings will be approximately 3 times lower than in the case of non-abradable (wear-resistant) coatings [6].

REQUIREMENTS FOR SEALING COATINGS

Based on the functional purpose of run-in sealing coatings, abradability is one of the basic requirements for sealing materials. To satisfy this requirement, it is necessary that the strength of the sealing material was much lower than the strength of the material of blades or crests of a labyrinth. However, the strength of the sealing material determines its erosion resistance, which should be high enough to guarantee operation of the engine during a set life. Since there are two such contradictory requirements set forth to the strength of the sealing material, the choice of its value is the most responsible moment in the development and application of coating.

The effect of the strength of the sealing material on its abrasion and erosion resistance is shown in Figure 2 [7]. The nature of these dependencies is similar for different materials, but quantitative ratios are different. When constructing these curves, it is implied that the composition of the coating material is maintained and the strength is regulated by changing the structure of the material.

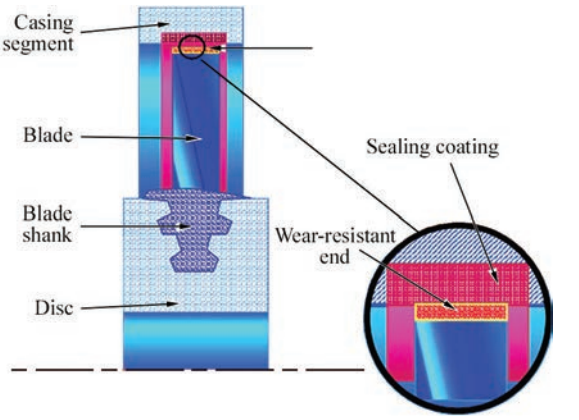

Figure 1. Scheme of application of sealing coating in GTE

Sealing coatings are used in different areas of GTE, as is shown in Figure 3, and the main criterion for choosing coating material is the operating temperature of the area, on which it is deposited [8].

General requirements (ideally) that abradable sealing coatings should meet, depending on working conditions, are the following [8, 9]:

- running-in of components being in contact;
- sufficient strength but significantly lower than the strength of rotor parts (blades);
- low friction coefficient, which reduces wear in the contact process;
- providing the minimum wear of compressor rotor parts (due to a high abrasion);
- absence of overheating and ignition of parts of titanium alloys as a result of friction (cutting) of rotor with stator;
- high erosion resistance of sealing in the conditions of gas flow with solid particles;
- resistance to cyclic temperature drops;

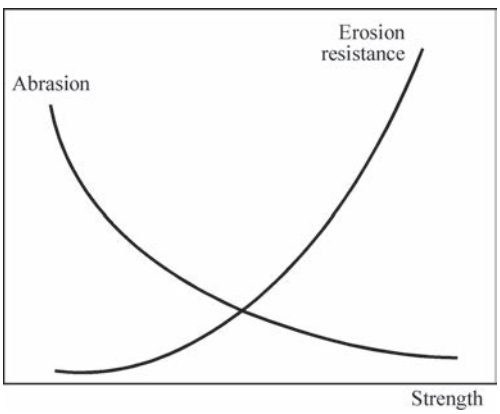

Figure 2. Impact of strength of sealing material on its abrasion and erosion resistance

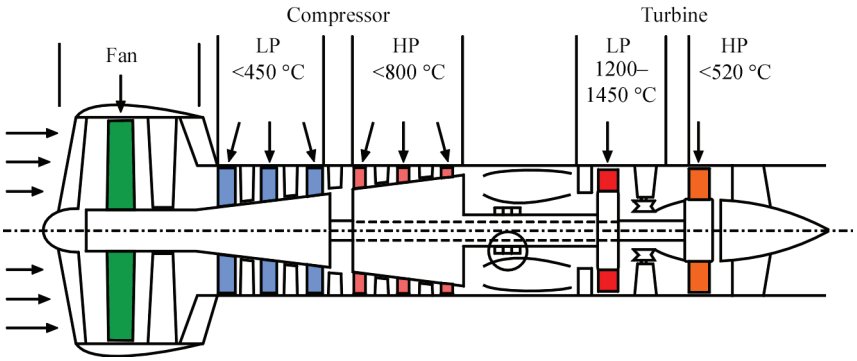

Figure 3. Model of modern turbine with temperature mode of operation of sealing coatings (LP — low pressure; HP — high pressure)

● the coefficient of thermal expansion that provides a reliable joining of abradable material (coating), with stator;

● stability of properties for a long time at operating temperatures;

● chemical resistance to salty water (corrosion), engine fuel, lubricant for hydraulic systems, engine flushing liquids;

● low plunging or contact friction energy;

● lack of transition of material from the surface of abradable seal on the end of blades and vice versa;

● lack of gas leaks due to open porosity in the material;

● low cost and repairability.

Since abradable material is cut by the ends of blades, it is also important that the formed products of wear do not exceed a certain size (0.2–0.3 mm). Larger particles getting into clearances between a rotating part and a sealing material can cause its additional fracture.

An effective operation of sealing coating is provided at the ratio of wear of coating to wear of blade, which is equal to 10:1. But at the ratio of 5:1, the operation of sealing coating is considered quite satisfactory.

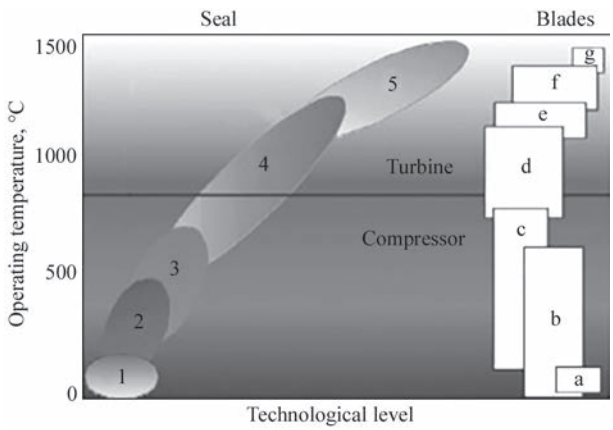

Figure 4. Types of materials for manufacture of seals and blades of GTE, depending on operating temperature: 1 — polymer; 2 — AlSi-polymer; 3 — metal matrix with solid lubricant; 4 — MCrAlY-materials; 5 — ceramics (a — fibrous polymer composites; b —titanium; c — stainless steel; d — super alloys; e — blades produced by directed crystallization; f —monocrystalline blades; g — heat-resistant alloys)

MATERIALS AND METHODS OF DEPOSITION OF SEALING COATINGS

Development and selection of sealing material consists in providing strength characteristics at which abrasion and erosion resistance of material meet the requirements specified under the set working conditions throughout the whole life. As strengthening coatings for GTE parts mostly composite coatings are used, consisting of matrix and fillers (solid lubricants).

The matrix in the coating provides its strength and resistance without leading to excessive wear of blades. As a matrix material in sealing coatings, the following materials are usually used:

● aluminum-silicon materials for low-temperature sections;

● MCrAlY (M = cobalt, nickel or cobalt/nickel) for medium temperatures of compressor sections;

● yttrium-stabilized zirconium (high-temperature ceramic material) for high-temperature turbine sections.

All of them have a strength, lower than in traditional materials (stainless steel, titanium, nickel alloys, etc.) used for the manufacture of GTE blades (Figure 4 [10]).

Depending on the hardness of the matrix material, the mechanism of coatings abrasion during plunging of blades can be of two types: wear with shear and wear with chipping of coating particles (Figure 5) [5]. The first type of wear is typical for coatings, where relatively soft alloys are used as the matrix material, that are subject to shear, such as Al-alloys (Figure 5, *a*). The second type of wear is characteristic of coatings, where, harder alloys are used as a matrix and to remove particles during a contact with a blade, the presence of porosity in the coating is required (Figure 5, *b*).

Solid lubricant or dislocation phase serves as a source of crack formation and propagation, providing the coating with the necessary brittleness, while ensuring that wear products are small enough and can not block cooling channels or provoke further wear of parts [11]. Graphite and hexagonal boron nitride are the materials, that are the most frequently used as a solid lubricant.

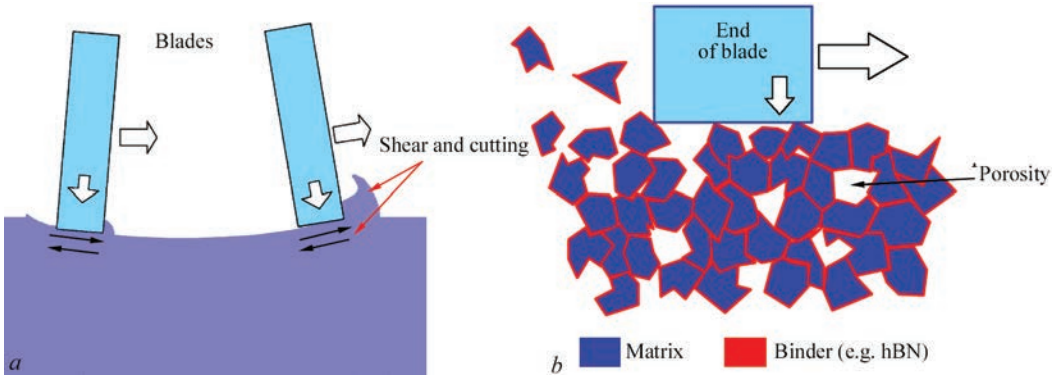

Figure 5. Schemes of wear mechanisms of coatings in contact with blades: *a* — wear with shear and cutting; *b* — wear with chipping

Sealing coatings should also have a certain level of porosity to achieve the desired abrasion. The controlled level of porosity can be achieved by adding the optimal amount of polyester to the sprayed material [12]. During further heat treatment, the polyester evaporates and the desired level of porosity is formed in the coating. Heat treatment of coating is carried out by heating to a temperature of 453–500 °C in air [11, 12]. The number and size of pores determine the abrasion and erosion resistance of coatings. Erosion resistance decreases with increasing porosity, and abrasion increases [12]. Pores and voids are microcrack nuclei between the particles of coating when touching the end of a blade. Due to these microcracks, a clean cut of coating with a minimal transfer of the coating material to the end of a blade occurs [11].

In some cases, sealing coatings require a preliminary spraying of the intermediate layer (sublayer) on the base to increase the adhesion strength. As the sublayer material, 9 5 % Ni–5 % Al is mainly used [8].

As the ranges of operating temperatures and pressures in GTE are very large, different materials and types of abradable coatings are used in them, depending on operating conditions of engine parts, on which they are deposited. The choice of a particular type of abradable coating primarily depends on the operating temperature of the section in which it will be used. Coating systems which are used depending on the operating temperature are shown in Figure 6 [5].

To form sealing coatings on GTE parts, thermal spraying technologies are the most promising and in demand today [13]. For this purpose, compositions of composite powders and flux-cored wires are developed. Coatings of composite powders are sprayed by oxyfuel and plasma spraying methods. The process of plasma spraying is a process with higher temperatures than that of oxyfuel spraying, which means that materials with higher melting temperatures can be deposited using the plasma spraying process. Flux-cored wire coatings are sprayed by oxyfuel and electric arc spraying methods.

By adjusting the thermal spraying modes, it is possbile to control the structure and, accordingly, the properties of produced coatings. Due to this, it is possible to produce sealing coatings with the following types of structures [14]:

- very porous, with many unmelted particles, produced by very careful selection of spraying parameters to achieve the desired degree of abrasion. An accurate reproduction of such coatings can be difficult, and they require a strict control;
- dense and homogeneous coating structures with such additives as polymers, graphite, bentonite and boron nitride (hBN). Abrasion is regulated mainly by the concentration of additives, not by changing spraying parameters, which helps to produce denser coatings with the desired properties.

SEALING COATINGS FOR COMPRESSOR SECTION

AlSi-polyester is a typical sealing coating that is widely used in GTE due to its good abrasion, self-lubrication and thermal conductivity and is the most common coating used in low pressure compressors at low temperatures [15]. The coatings are deposited by the method of plasma spraying of a mixture of powders of aluminum-silicon alloy (Al–12Si) and polyester. The content of aluminum-silicon alloy, which provides structural strength and resistance of the coating to erosion, amounts to about 52 %, and polyester

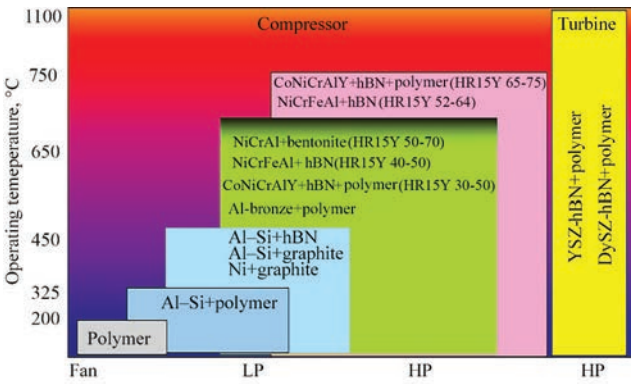

Figure 6. Systems of sealing coatings used for GTE parts depending on the operating temperature

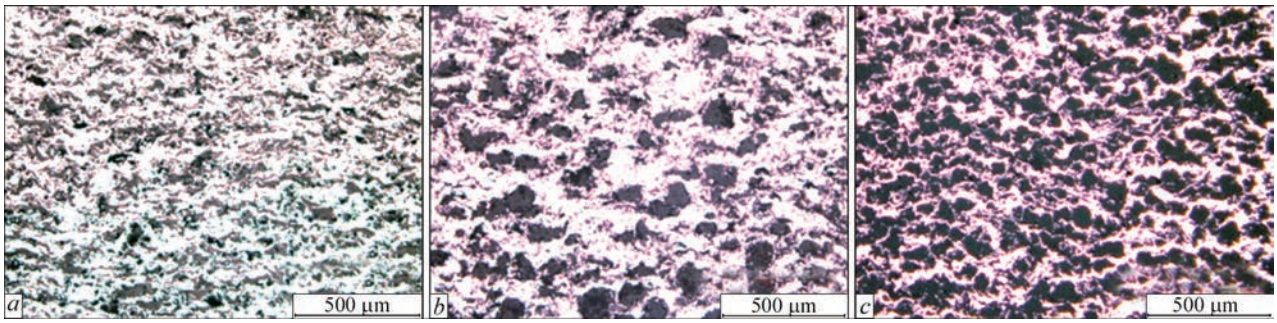

Figure 7. Microstructure of AlSi alloy based coatings with solid lubricant additives: *a* — graphite; *b* — hexagonal boron nitride; *c* — polyester

with self-lubricating characteristics amounts to about 40 %, the rest is a binder. AlSi-polyester sealing coating is mainly used for sealing the casing in the lower and middle parts of compressor with a temperature of up to 350 °C (as a result of temperature limitation of polymer in the coating) [16]. The desired level of porosity of coatings amounts to 2 % with a corresponding Rockwell surface hardness HR15Y 40-50. According to Sulzer Metco [17], coatings of 60Al–12Si–40 polyester, deposited by plasma method, have a hardness HR15Y 65–80 and porosity of 3–5 %.

As fillers, hexagonal boron nitride and graphite are also used. Coatings of Al–8Si-hBN (20 %) + organic binder (8 %) and Al5Si (Al6Si, Al7Si) — graphite (22, 24, 45 %) + organic binder (7, 9, 8 %) are upplied at operating temperatures up to 450–480 °C (due to the temperature limitation of aluminum in the material). The desired level of porosity amounts to 15–20 % with the corresponding Rockwell surface hardness HR15Y 40–50 (40–70 according to Sulzer Metco) [15]. The content of hexagonal boron nitride in the coatings can amount to 40–50 % [9].

Al-bronze alloy is also used [18] as a matrix instead of AlSi alloy. The operating temperature of the coating, taking into account Al (7.5–8.5 %)–Cu (75–85 %) alloy with the addition of polymer (5.0–14.5 %) is up to 650 °C. At operating temperatures above 350 °C, it is necessary to carry out heat treatment of the coating to remove polyester in order to prevent an uncontrolled flash. The coatings are deposited by plasma method. Hardness of coatings amounts to HR15Y 60–70 and the porosity is 6–10 %.

The microstructure of coatings based on AlSi alloy with the addition of polyester, hexagonal boron nitride and graphite is shown in Figure 7 [5].

When using metal matrices with higher melting point and shear strength than in aluminum or its alloys, the coating structure is usually porous to provide its abrasion. Such coatings include coatings of the nickel-graphite system, the structure of which represents a nickel matrix in which lamellar graphite is randomly distributed (Figure 8) [19]. Due to the content of graphite, nickel-graphite composite coatings are also limited in temperature to about 450 °C. The hardness of the nickel-graphite coating varies depending on the ratio of nickel and graphite in it. The content of graphite in the coatings can vary from 15 to 40 %.

For higher operating temperatures, it is advisable to use alloyed Ni in combination with ceramic fillers. An example of coating used in compressor at operating temperatures up to 700 °C is shown in Figure 9 [20]. The structure of the coating consists of NiCrAl matrix, thermostable ceramic dislocation particles and porosity.

NiCrAl-bentonite coatings (Ni–4Cr–4Al–21 % bentonite) have higher heat resistance than AlSi-polyester, AlSi-hBN, AlSi-graphite or Ni-graphite coatings and are successfully used in the high-temperature section of high-pressure compressors at a temperature higher than 500 °C [21]. HR15Y hardness of coatings is 30–60.

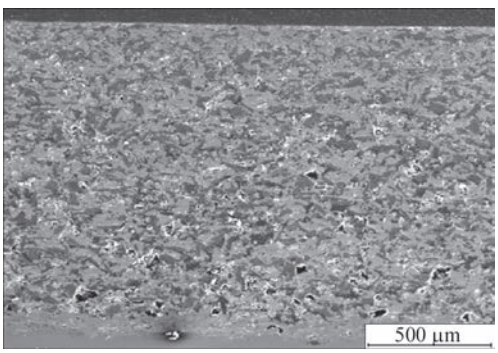

Figure 8. Microstructure of Ni-graphite coating

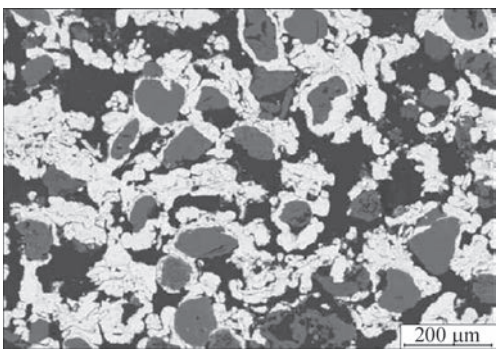

Figure 9. Microstructure of NiCrAl-ceramics coating

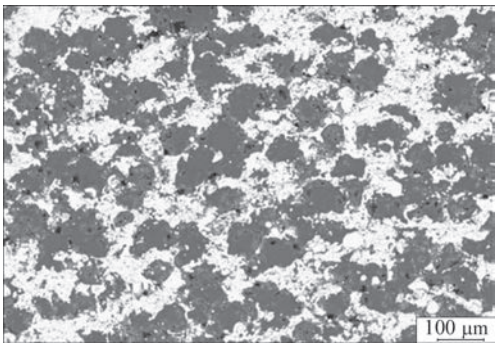

Figure 10. Microstructure of plasma CoNiCrAlY-hBN-polyester coating

During operation of coatings at higher temperatures, it is necessary that the coatings have resistance to erosion and high-temperature oxidation at corresponding operating temperatures. As a metal matrix, in these cases MCrAlY (M = Ni and/or Co) materials are used.

As far as solid lubricant/dislocator should withstand high temperatures hexagonal boron nitride (hBN) is used as a solid lubricant. Coatings are usually produced by the method of plasma spraying. The porosity in the coatings is formed by introducing polyester particles, which are removed from the coating by heat treatment, resulting in formation of porosity in the coating. Figure 10 shows a typical microstructure of plasma coating CoNiCrAlY-hBN-polyester [12].

The content of the components in the coatings is Co(29–30 %)–Ni(24–25 %)–Cr(16 %)–Al(6 %)–Y(0.3 %)-hBN(4, 7 %) + polyester (14–15 %) + organic binder (3 %).

It is strongly recommended that these coatings are subjected to heat treatment after spraying to remove the polymer component and create porosity in the coating structure, improving abrasion. Usually, such coatings have a porosity from 35 to 60 % and a hardness from 65 to 75 when measuring on the Rockwell HR15Y scale. The coating is recommended to be used at temperatures up to 850 °C.

SEALING COATINGS FOR TURBINE SECTION

Similarly to CoNiCrAlY-based coatings described above, modern ceramic sealing coatings consist of three phases: the phase of ceramic matrix, usually zirconium oxide, stabilized by yttrium oxide or dysprosium, polymer and solid lubricant [5, 20, 22]. The polymer can be removed from the coating in the process of heat treatment to create porosity in the coating. As a solid lubricant, hexagonal boron nitride is used. Typical thermal protection coatings have the following composition: 94.5 % YSZ (or DySZ) — 4.7 % polyester — 0.8 % hBN. To protect the metal base from high-temperature corrosion and oxidation, as well as to reduce the difference of the coefficients of thermal expansion between the base and the ceramic layer, a metal MCrAlY sublayer is used. Microstructure of typical sealing coatings based on ceramics with different level of porosity is shown in Figure 11 [5].

Today, at aircraft engineering enterprises of Ukraine, KNA-82 nickel-based coatings with satisfactory service properties at temperatures of 900–950 °C are widely used. A further increase in the temperature of gases to 1100–1200 °C can lead to catastrophic development of gas corrosion and destruction of coating. In this connection, to solve the problem of increasing the resistance of sealing coatings, it was suggested to perform an additional alloying of KNA-82 coating with different kinds of yttrium-contained master alloys: with monocomponent yttrium (Y), Ni–Y composition and multi-component composition of Co–Ni–Cr–Al–Y [23–25]. Figure 12 shows the microstructure of the developed coatings deposited by oxyfuel method [25].

METHODS OF STUDYING THE PROPERTIES OF SEALING COATINGS

As was mentioned earlier, the basic properties of sealing coatings are abrasion and erosion resistance.

The mechanisms of coatings abrasion are very complex, as during contact of the coating with the blade, a combination of cutting, heating, plastic deformation and wear occurs. Therefore, it is extremely difficult to model the service conditions of sealing coating in the laboratory. There are a number of highly specialized installations to determine abrasion used by engine manufacturers and developers of coatings.

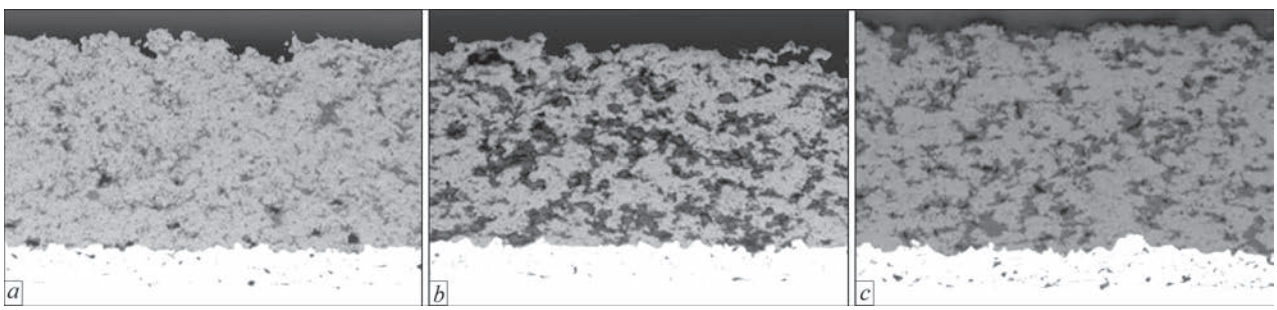

Figure 11. Microstructure (×50) of coatings based on ZrO_2–Y_2O_2 (*a*, *b*) and ZrO_2–Dy_2O_3 (*c*) with different level of porosity, %: *a* — 24; *b* — 43; *c* —30

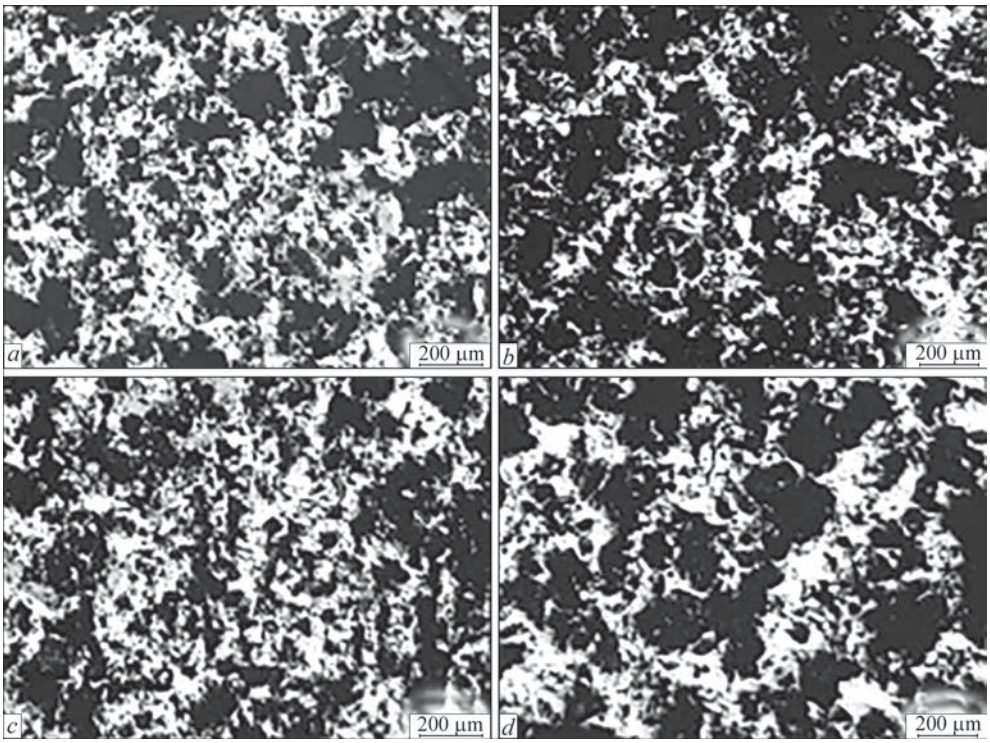

Figure 12. Microstructure of sealing coatings produced by oxyfuel method of spraying: *a* — KNA-82 + master alloy; *b* — KNA-82 + pure yttrium; *c* — KNA-82 + master alloy Co–Ni–Cr–Al–Y; *d* — KNA-82: KNA+VKNA powder (serial technology)

In particular, Sulzer Metco company has one of the installations for testing materials for abrasion (Figure 13), which has proven itself well and is constantly used by manufacturers of engines and companies producing coatings around the world [9].

There are also many self-made testing installations to test coatings abrasion. However, there is still no standardized method to test coatings abrasion and therefore, the results obtained during testing in different installations cannot be compared.

HR15Y hardness tests are to some extent an alternative to a bench test abrasion [26]. To determine the hardness of high-porosity coatings, the used method should have an averaging effect and allow measuring very low hardness. The Rockwell resistance hardness test (HR15Y) is suitable for taking into account these two conditions and is used to measure the hardness of sealing abradable coatings.

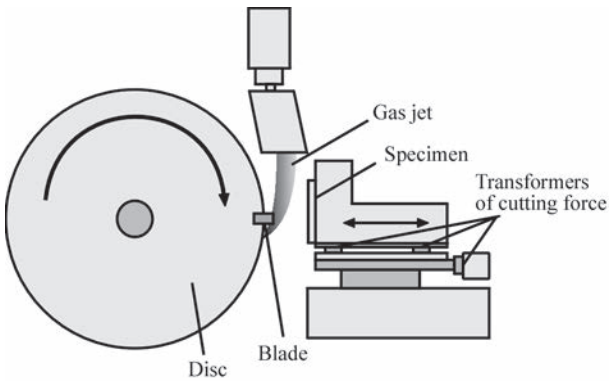

Figure 13. Scheme of installation for high-temperature tests of sealing materials and coatings for abrasion

Erosion tests are carried out according to the standard procedure of quantitative evaluation of the surface of coatings to erosion with the use of a shot blasting machine. The specimen is located 100 mm from the nozzle of the shot blasting machine at an angle of 20°; aluminum oxide with 50 μm particles is used as abrasive [9].

The properties of abradable sealing coatings are determined by their chemical composition, as well as their microstructure. Two coatings with the same chemical composition, but with a very different microstructure, will not behave equally under the same operating conditions. Several studies emphasize the influence of the microstructure of the coating on the effective thermomechanical properties and general characteristics [27, 28]. For example, it is reported that pores and cracks reduce the thermal conductivity of coatings. Determination of the volume content of different structural components of the coating is performed by using the method of image analysis.

The adhesion strength of sealing coatings with the base is determined by the method of tear (ASTM C633) or bending (ASTM B571).

In addition to a good abrasion, heat impact and thermal cycling resistance is another important requirement for sealing coating of compressors and turbines. For strengthening the parts of compressor, the coatings are subjected to tests on thermal cycling

by heating to 470 °C with subsequent water cooling. Thermal resistance of the coating under these conditions is resistance determined by the change in the adhesion strength of coatings with the base. As a reference, the adhesion strength of sprayed coating before thermocycling is taken [29].

For ceramic coatings, thermal cycling is carried out in the conditions of furnace heating up to 1150 °C with the subsequent air cooling to 50 °C. The test temperature and the period of coatings exposure during heating may vary depending on the desired condition of application. Thermal resistance of coating can also be determined relative to the change in adhesion strength of coating, but the most common approach is visual inspection of coating for cracking or delamination from the base.

The tests of sealing coatings for corrosion resistance are performed by immersing the specimens in a saturated saline solution in the furnace at a set temperature, which is higher than the room temperature and lower than 100 °C. The specimens are maintained in these conditions for several hours and then visual inspection for the presence of corrosion traces is carried out [9]. After tests in this case, the results are only qualitative, so it is difficult to compare the results of different tests.

CONCLUSIONS

1. Based on the analysis of literature data on operating conditions of GTE, it was established that one of the methods to increase the efficiency of engines is to create an effective system of sealing the flow path of compressor and turbine by thermal deposition of abradable coatings on the stator surface.

2. The basic requirements for the properties of sealing coatings, which include a tendency to abrasion and erosion resistance, were identified.

3. It was established that the main materials for deposition of sealing coatings on the casing of a compressor part of GTE, where temperature mode does not exceed 500 °C, are materials based on aluminum; for sections of compressor with an operating temperature of up to 800 °C — McrAlY-based materials (M = = Co, Ni or Co/Ni); for high-temperature sections of turbines ceramic materials based on zirconium oxide are used. As a dislocation phase in thermal sealing coatings, solid lubricants and polymers are used.

REFERENCES

1. Koval, V.A., Mikhailov, V.E., Romanov, V.V., Kovalyova, E.A. (2013) *Features of operation processes in gas-turbine and steam-gas power plants and their components*. Kharkov, Kontrast [in Russian].
2. Inozemtsev, A.A., Bazhin, S.V., Snitko, M.A. (2012) Problems of optimization of turboprop radial clearances of aircraft gas-turbine engine. *Vestnik Dvigatelestroyeniya*, **2**, 149–154.
3. Nalimov, Yu.S. (2014) Analysis of damage of gas-turbine engine blades. *Metall i Litiyo Ukrainy*, **12**, 17–22 [in Russian].
4. Berezkin, S.V., Greshta, V.L., Lekhovitser, Z.V., Olshanetskiy, V.E. (2019) Improvement of batch produced and prospective coatings of labyrinth seals of hot section parts of gas-turbine engine. *Novi Materialy i Tekhnologii v Metalurgii ta Mashynobuduvanni*, **2**, 91–94 [in Russian].
5. Wilson, S. (2011) Overview of sulzer metco compressor and turbine abradable technology. In: *Proc. of 8th Int. Charles Parsons Turbine Conf., University of Portsmouth, Portsmouth, UK*. URL: http://www.iom3.org/sites/default/files/iom3-corp/wed%200940%20s%20Wilson.pdf
6. Siddiqui, S.M., Joshi, P., Nayak, N., Vidyasagar, K. (2014) Thermal spraying, optimization and characterization of abradable seal coating for gas turbine for service temperature up to 750 °C. *Adv. Mat. Lett*., 5(**9**), 506–510.
7. Aussavy, D. (2016) *Processing characterization and modeling of thermomechanical properties of three abradable coatings: NiCrAl-bentonite, CoNiCrAlY–BN-polyester, and YSZ-polyester*. *Materials*. Université de Technologie de Belfort-Montbeliard.
8. Mohammad, F., Kashif, A. (2021) Criteria for abradable coatings to enhance the performance of gas turbine engines. *J. Mater. Sci. Metall*., **2**, 101.
9. Hopkins, N.P. (2007) *Abradable coatings — From black art, to materials science*: Engineering Doctorate. Swansea University.
10. Kutz, M. (2018) *Handbook of environmental degradation of materials*. Third edition. DOI: https://doi.org/10.1016/C2016-0-02081-8
11. Fois, N., Watson, M., Marshall, M. (2016) The influence of material properties on the wear of abradable materials. In: *Proc. of the Institution of Mechanical Engineers*, Pt J: J. of Engineering Tribology, 231(**2**), 240–253. DOI: https://doi:10.1177/1350650116649528
12. Irissou, E., Dadouche, A., Lima, R.S. (2013) Tribological characterization of plasma-sprayed CoNiCrAlY–BN abradable coatings. *J. of Thermal Spray Technology*, 23(**1–2**), 252–261. doi:10.1007/s11666-013-9998-4
13. *Thermally sprayed abradable coating technology for sealing in gas turbines. Oerlikon Metco*. https://www.oerlikon.com/ecomaXL/files/oerlikon_ThermallySprayedAbradableCoatings_2012.10.pdf&download=1
14. *There are a number of different abradable coating types*. JINHU COLOR POWDER COATING CO.LTD. DOI: https://www.chinapowdercoating.com/abradable-coating/
15. Rajendran, R. (2012) Gas turbine coatings: An overview. Engineering *Failure Analysis*, **26**, 355–369. DOI: https://doi.org/10.1016/j.engfailanal.2012.07.007
16. Zhang, N., Shen, J., Xuan, H. et al. (2015) Evaluation of an AlSi-polyester abradable seal coating performance using high-temperature and high-velocity abrasion tests. In: Proc. of the Institution of Mechanical Engineers, Pt J. *J. of Engineering Tribology*, 230(**7**), 842–851. DOI: https://doi.org/10.1177/1350650115619150
17. Aluminum-polyester powder. *Technical Bulletin*, **10–141**. Metco601NS. DOI: https://www.gordonengland.co.uk/sef/attachment.php?aid=309
18. *Oerlikon Metco material product data sheet aluminium bronze/polyester abradable powders. Oerlikon Metco*. https://www.oerlikon.com/ecoma/files/DSMTS-0012.3_Al_Bronze_Poly.pdf?download=true
19. Gao, S., Xue, W., Duan, D., Li, S. (2016). Tribological behaviors of turbofan seal couples from friction heat perspective under high-speed rubbing condition. *Friction*, 4(**2**), 176–190. DOI: https://doi:10.1007/s40544-016-0114-x

20. Sporer, D., Wilson, S., Giovannetti, I. et al. (2007) On the potential of metal and ceramic based abradables in turbine seal applications. In: *Proc. of the Thirty-Sixth Turbomachinery Symp*., 79–86. DOI: https://doi: 10.21423/R1336H
21. Johnston, R.E. (2011) Mechanical characterisation of Al-Si-hBN, NiCrAl-bentonite, and NiCrAl-bentonite-hBN free-standing abradable coatings. *Surface and Coatings Technology*, 205(**10**), 3268–3273. DOI: https://doi:10.1016/j.surfcoat.2010.11.044
22. Cheng, X., Yueguang Y., Jianming L. et al. (2022) Mesoscale simulation and evaluation of the mechanical properties of ceramic seal coatings. *Coatings*, 12(**4**), 438. DOI: https://doi.org/10.3390/coatings12040438-
23. Sotnikov, E.G., Lekhovitzer, Z.V., Greshta, V.L. et al. (2015) Development of composition of heat-resistant coating on parts of gas-turbine engines operating under high temperatures conditions. *Aviatsionno-Kosmicheskaya Tekhnika i Tekhnologiya*, 10(**12**), 6–10 [in Russian].
24. Greshta, V.L., Pavlenko, D.V., Dvirnyk, Ya.V., Tkach, D.V. (2019) Experiment and calculation procedure for determination of dynamic modulus of elasticity of running-in sealing coatings of GTE turbines. *Aviatsionno-Kosmicheskaya Tekhnika i Tekhnologiya*, 160(**8**), 105–113. DOI: https://doi: 10.32620/aktt.2019.8.16
25. Greshta, V., Tkach, D., Sotnikov, E. et al. (2018) Studying and designing improved coatings for labyrinth seals of gas-turbine engine turbines. *Eastern-European J. of Enterprise Technologies*, 4(12, 94), 56–63. DOI: https://doi: 10.15587/1729-4061.2018.140912
26. Peyraut, F., Seichepine, J.-L., Coddet, C., Hertter, M. (2008) Finite element modeling of abradable materials: Identification of plastic parameters and issues on minimum hardness against coatings thickness. *Int. J. for Simulation and Multidisciplinary Design Optimization*, 2(**3**), 209–215. DOI: https://doi.org/10.1051/ijsmdo:2008028
27. Faraoun, H.I., Grosdidier, T., Seichepine, J.-L. et al. (2006) Improvement of thermally sprayed abradable coating by microstructure control. *Surf. and Coat. Technol*., 201(**6**), 2303–2312. DOI: https://doi.org/10.1016/j.surfcoat.2006.03.047
28. Karthikeyan, S., Balasubramanian, V., Rajendran, R. (2014) Developing empirical relationships to estimate porosity and Young's modulus of plasma sprayed YSZ coatings. *Applied Surface Sci*., **296**, 31–46. DOI: https://doi.org/10.1016/j.apsusc.2014.01.021
29. (2012) *Thermally sprayed abradable coating technology for sealing in gas turbines. Oerlikon Metco*. doi: 10.15587/1729-4061.2018.140912]. DOI: https://www.oerlikon.com/ecomaXL/files/oerlikon_ThermallySprayedAbradableCoatings_2012.10.pdf&download=1

ORCID
Yu.S. Borysov: 0000-0002-6019-8464,
N.V. Vihilianska: 0000-0001-8576-2095,
O.M. Burlachenko: 0000-0003-2277-4202
L.P. Olevska: 0000-0002-9043-2397,
V.M. Lopata: 0000-0002-1578-1298

CONFLICT OF INTEREST
The Authors declare no conflict of interest

CORRESPONDING AUTHOR
L.P. Olevska
E.O. Paton Electric Welding Institute of the NASU
11 Kazymyr Malevych Str., 03150, Kyiv, Ukraine
E-mail: olevska@paton.kiev.ua

SUGGESTED CITATION
Yu.S. Borysov, N.V. Vihilianska, O.M. Burlachenko, L.P. Olevska, V.M. Lopata (2022) Analysis of modern experience in development of sealing coatings for parts of gas turbine engines (Review). *The Paton Welding J*., **4**, 34–42.

JOURNAL HOME PAGE
https://pwj.com.ua/en

Received: 30.03.2022
Accepted: 30.06.2022

https://doi.org/10.37434/tpwj2022.04.07

INFLUENCE OF MICROSTRUCTURE OF MULTILAYER Al/Ni FOILS ON PHASE TRANSFORMATIONS INITIATED BY HEATING

A.I. Ustinov, S.O. Demchenkov

E.O. Paton Electric Welding Institute of the NASU
11 Kazymyr Malevych Str., 03150, Kyiv, Ukraine

ABSTRACT

At heating of multilayer Al/Ni foil the component interdiffusion is accompanied by phase transformations, which can occur by a two-channel multistage or single-channel one-stage schemes. It is shown that the type of the scheme by which the phase transformations develop in the studied multilayer foils, is related to the process of formation of a metastable Al_9Ni_2-phase on the layer interfaces. The work is a study of the influence of multilayer foil microstructure on formation of a metastable Al_9Ni_2-phase. It is found that the thickness of Al_9Ni_2-phase layers is determined by the thickness of aluminium layers in the initial multilayer foil. At the thickness of Al layers of 70–80 nm and greater, the thickness of Al_9Ni_2-phase layers practically does not change, and is equal to approximately 30–35 nm; at reduction of Al layer thickness, the thickness of Al_9Ni_2-phase layers decreases abruptly, and at A1 thickness less than 10–12 nm, the layers of a metastable Al_9Ni_2-phase do not form. The process of formation of metastable Al_9Ni_2-phase layers is characterized by a high rate and incubation time. Proceeding from the obtained results, a structural-kinetic diagram was proposed, which allows determination of the conditions for prevention of the multistage process of achievement of the foil equilibrium state during its heating.

KEYWORDS: multilayer foils; electron beam deposition; phase transformations; intermetallics; SHS reaction

INTRODUCTION

It is known that multilayer foils (MF) consisting of Al and Ni layers can be used as intermediate layers when producing permanent joints. The process of joining materials with the use of MF is realized either by initiating the reaction of self-propagating high-temperature synthesis (SHS), which provides local heating of the joint zone, or due to the development of solid-phase reactions in MF initiated by continuous heating, which activate diffusion processes in the joint zone [1, 2]. Therefore, the possibility of predicting the kinetics of the development of phase transformations in MF, depending on their chemical composition and modulation period both in the process of continuous heating and also as a result of SHS reaction is a necessary condition for their effective practical use.

The phenomenological models, describing the propagation of the SHS reaction front in MF are based on the assumption that on the interface of the layers, a thin intermediate layer with the intermetallic structure exists, which forms in the process of MF preparation. Calculations based on these models show that the thickness of the layer of several nanometers can significantly affect the characteristics of the SHS reaction [3]. Based on this fact, it is assumed that it predetermines a high sensitivity of the SHS reaction characteristics to the method of MF preparation.

On the other hand, a number of works show that the method of MF preparation affects the initial stages of phase transformations initiated by continuous heating. For example, during heating of MF produced by the methods of magnetron [4] or electron beam deposition, instead of a stable Al_3Ni phase, first a metastable Al_9Ni_2-phase is formed [5], whereas during heating of MF produced by the methods of cold rolling of laminates [6], first, the formation of a stable Al_3Ni phase is observed intermetallic formation. A number of authors [4] associate this difference in phase formation during continuous heating of MF with a different structure of interfaces between the layers of the components, which depends on the method of foil preparation.

In [5], on the example of Al/Ni MF produced by the method of electron beam deposition with different ratios of original components and modulation periods from 50 to 500 nm, it was shown that initial stages of phase transformations with continuous heating are characterized by the formation of Al_9Ni_2-phase in the range of temperatures of 200–250 °C. At a further increase in temperature, phase transformations in MF are realized according to the two-channel scheme:

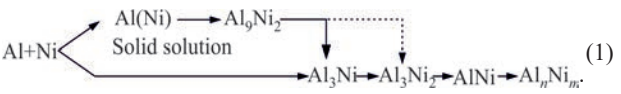

(1)

In addition, the formation of a metastable Al_9Ni_2 phase can also be significantly affected by the modulation period of layers [7]. Thus, at a continuous heating of Al/Ni foils produced by the methods of magnetron deposition, the formation of Al_9Ni_2-phase was observed only in the case of foils with a modulation period of more than 20–25 nm, and in MF with a modulation period of less than 20–25 nm intermetal-

lic formation, that corresponds to the foil steichiometry without the formation of intermediate phases:

$$Al + Ni \rightarrow Al_nNi_m. \quad (2)$$

A similar single-channel scheme of transformations in MF, as the authors of the work [8] assume, is also realized during initiation in the SHS reaction.

Thus, the results of the conducted studies show that the sequence of phase transformations in MF depends on a number of factors that can be conditionally divided into three groups: method of MF manufacturing, characteristics of MF microstructure (chemical composition, period of layers alternation, etc.), mode of the synthesis reaction development (heating rate).

However, there are still no works in the literature aimed at establishing parameters that determine the change in the modes of the synthesis reaction depending on the characteristics of the MF microstructure and the nature of this phenomenon.

In connection with the above-mentioned, the study of the effects of Al/Ni MF microstructure on the regularities of phase transformations initiated in them by heating was conducted in order to establish the factors that determine the change in the scheme of phase transformations from the two-channel multi-stage into a single-channel one-stage.

EXPERIMENTAL STUDIES

Multilayer foils were produced by the method of electron beam evaporation of elements in vacuum with their layer-by-layer deposition on the substrate, which is described in detail in [9]. The source components were ingots of Al (99.95 %) and Ni (99.98 %). The substrate temperature in the process of deposition was 150–170 °C, the deposition rate was about 2–5 nm/s. The choice of a certain ratio between the density of the vapor flow and the rotation speed of the substrate allowed producing foils with different ratios of elements and different thicknesses of Al and Ni layers. The total thickness of foils ranged from 30 to 150 μm, and the period of alternation (λ) of layers of Al and Ni was from 25 to 600 nm. The chemical composition of foils varied from $Al_{25}Ni_{75}$ to $Al_{75}Ni_{25}$ (at.%).

The temperature intervals of phase transformations during heating of MF were studied by the DTA method in the VDTA-8 installation at a heating rate of foils of 0.8 degrees/s. To quantify thermal effects, differential scanning calorimeter (DSC) DuPont 1090 Thermal Analyser was used in the work. X-ray measurements were carried out in 0–2θ geometry in the Dron-4-07 diffractometer in the Cu–K_α radiation. The microstructure of the samples was investigated using the Camscan-4 scanning electron microscope equipped with the energy dispersive spectrometer Energy200 to determine the chemical composition.

RESEARCH RESULTS AND THEIR DISCUSSION

The study of the process of formation of a metastable Al_9Ni_2-phase was carried out by X-ray structural analysis after isothermal annealing of MF ($Al_{50}Ni_{50}$, λ = 110 nm) depending on time. It was established that the formation of Al_9Ni_2-phase occurs during heating of MF to the temperature of 250 °C (Figure 1). Exposure at a set temperature in the first moments of time leads to a slight increase in the volume fraction

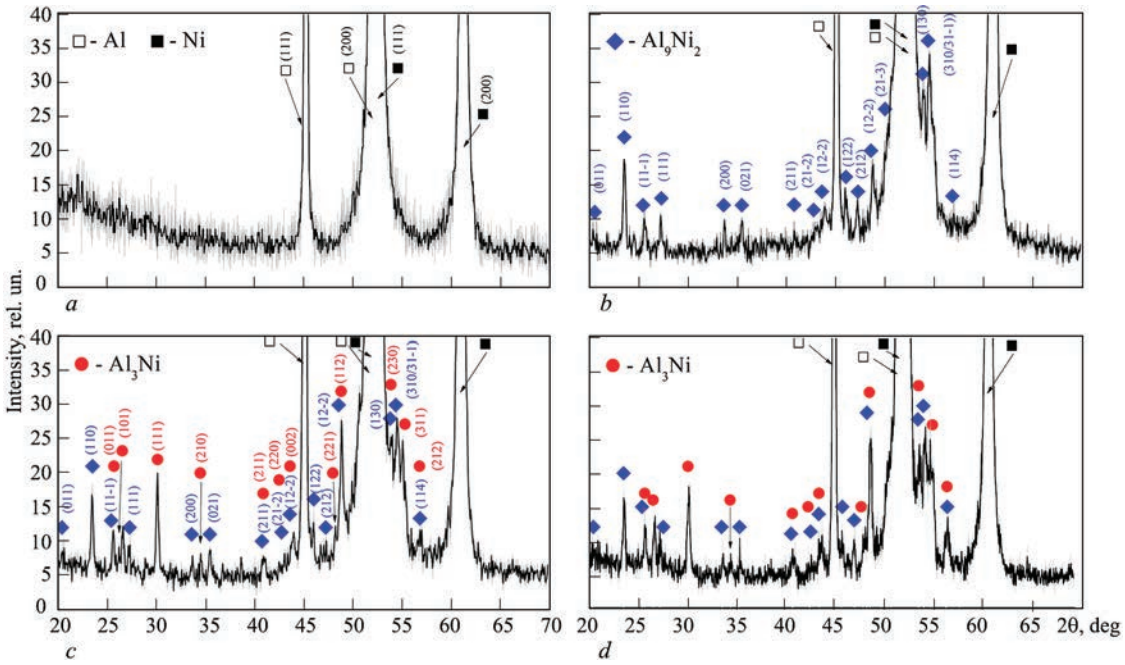

Figure 1. Diffractograms of Al/Ni MF in the initial state (*a*), after heating to the temperature, °C: 250 (*b*), 250 and exposure for 30 min (*c*), 300 (*d*): □ — Al; ■ — Ni; ◆ — Al_9Ni_2; ● — Al_3Ni

of Al_9Ni_2-phase. With the further increase in annealing time, the formation of Al_3Ni phase is observed, accompanied by a decrease in the intensity of diffraction peaks of Al and Ni. In this case, the formation of Al_3Ni-phase does not reduce the intensity of diffraction peaks (volume fraction) of Al_9Ni_2-phase. An increase in the annealing temperature of MF to 300 °C also does not lead to a further increase in the volume fraction of Al_9Ni_2-phase.

The time interval of the process of Al_9Ni_2-phase formation was evaluated by the method of in-situ X-ray diffractometry at a continuous heating of MF at 20 degrees/min. From the data of diffractograms in Figure 2, one can see that the characteristic diffraction peaks of Al_9Ni_2-phase appear for about 1 min after reaching the temperature of 250 °C, and at a further increase in temperature, their intensity remains almost unchanged. This indicates a high rate of Al_9Ni_2-phase formation and a discrete nature of transformation.

The similar results were obtained earlier in [10] while studying the kinetics of forming Al_9Ni_2-phase in the process of isothermal annealing of MF at a temperature of 200 °C, which was manufactured by magnetron deposition (Figure 3). It was found, that formation of Al_9Ni_2-phase is preceded by some delay period (incubation time). At the end of the incubation time, the formation of Al_9Ni_2-phase begins, but this process occurs only in some limited interval of time, the duration of which depends on the annealing temperature (with an increase in annealing temperature, the time of Al_9Ni_2-phase formation is reduced). According to the diagram presented in Figure 3, at annealing temperatures of about 250 °C, the transformation time should be about 1 min, which is satisfactory consistent with the obtained results. The dashed lines indicate the temperature and time interval of Al_9Ni_2-phase formation, found in this work in Al/Ni MF produced by the method of electron beam deposition (dashed lines, applied above on the diagram).

The authors of [10] believe that the presence of an incubation period in the formation of Al_9Ni_2-phase in the process of isothermal annealing of MF, the low energy of activation of the transformation process and a high rate of its developing are predetermined by the fact that Al_9Ni_2-phase formation is preceded by the process of forming of Al(Ni) solid solution on the interphase boundaries. To confirm this, the authors provide DSC data, according to which, before a low-temperature peak of the heat removal appears, characteristic of Al_9Ni_2-phase formation, a blurred peak is observed, which may be associated with the heat removal caused by the formation of a solid solution of nickel in aluminum.

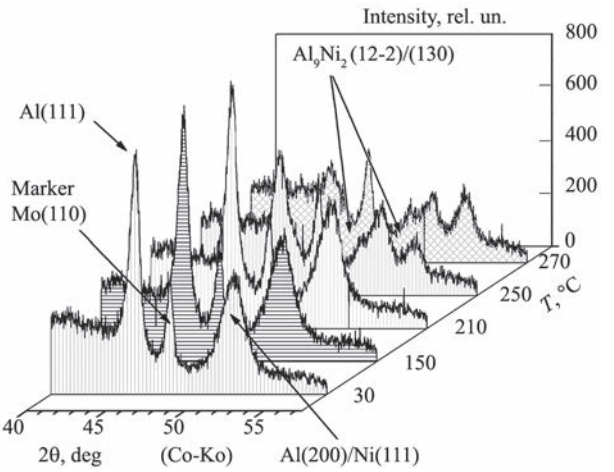

Figure 2. Fragments of diffractograms obtained directly in the process of heating Al/Ni MF (3Al:1 Ni, λ = 120 nm) at a rate of 20 °C/min (shooting frequency is 1 min^{-1})

It can be assumed that the formation of a solid solution of nickel in aluminum is possible if thermodynamic factors exist that prevent the nucleation of Al_9Ni_2-phase in the initial stages of annealing, and diffusion mobility of nickel atoms is high enough at so low temperatures.

Delay in the nucleation of Al_9Ni_2-phase may be predetermined by the presence of a significant concentration gradient on the interfaces between the layers of nickel and aluminum in MF in its original state. According to [11] in such conditions, the formation of phase nuclei becomes thermodynamically disadvantageous. On the example of a layered Al/Co system, it was shown that the nucleation of Al_9Co_2-phase occurs only at the moment, when the concentration profile on the elements interface becomes more gentle (after annealing at 300 °C for 5 min).

Thus, the presence of a significant concentration gradient on the elements interface can interfere with

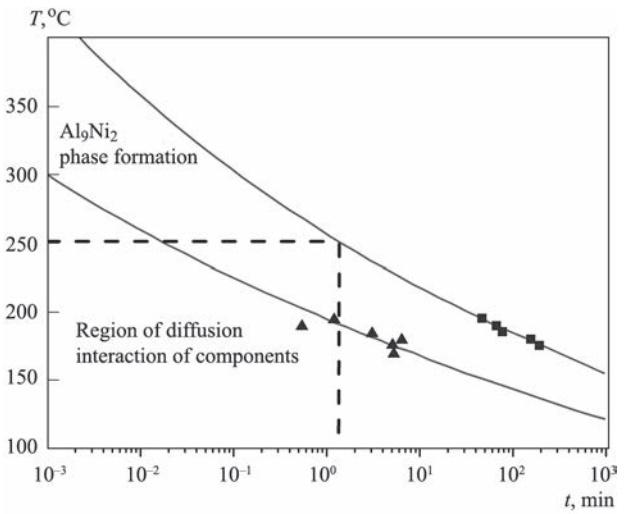

Figure 3. Temperature and time diagram of Al_9Ni_2 phase formation (solid lines and experimental points) at isothermal exposure of Al/Ni MF (the period of layers alternation λ = 80 nm) produced by magnetron deposition [10]

the formation of nuclei of the new phase at the initial stages of annealing and will promote a diffusion redistribution of elements, provided that diffusion mobility of atoms will be quite high at such low temperatures.

Taking into account that such phenomena are observed only in MF produced by the methods of physical deposition of elements at relatively low temperatures, it was suggested that their abnormally high diffusion mobility may be predetermined by the presence of a large number of non-equilibrium (excessive) vacancies. According to numerical modeling carried out in [12], the concentration of excessive vacancies in metal condensates depends on the temperature and rate of their deposition and may exceed their equilibrium value by 5–10 orders of magnitude. Considering that the concentration of vacancies significantly affects the coefficient of atoms diffusion [13], it can be assumed that the presence of a significant number of excessive vacancies in MF produced by the mehods of physical deposition, provides the process of forming of a layer of a solid solution of nickel in aluminium at the interfaces of these elements in a short time and at relatively low temperatures.

The work [5] shows the possibility of realizing the process of Al_9Ni_2-phase formation from the solid solution of Al(Ni) by the shear mechanism. Such a transformation mechanism provides the orientation ratios between the crystallographic lattices of aluminum and Al_9Ni_2-phase, whereas the transformation proper does not require a high energy of activation and can be carried out at relatively low temperatures.

From the comparison of crystalline lattices of aluminum and Al_9Ni_2-phase, it follows that during realization of this type of phase transformation, in addition to the presence of a shear component of deformation in the transformed volume, there will also be a component of deformation associated with a change in the volume, which with an increase in the thickness of Al_9Ni_2-phase layer will be accumulated. Considering that the diffusion of Al–Ni pair is characterized by the presence of significant asymmetry of diffusion flows with the predominance of nickel atoms movement into aluminum layers [14], the growth of the thickness of Al_9Ni_2-phase layer will cause significant elastic distortions in the areas of aluminum that do not participate in the transformation. As a result, when a certain value of Al_9Ni_2-phase layer is achieved, its further growth can be energetically disadvantageous. This can explain the found discrete nature of the process of Al_9Ni_2-phase formation and growth.

In addition, from the abovementioned assumptions, it follows that the growth of the thickness of Al_9Ni_2-phase layer can be influenced by both the elastic fields created by it in the matrix (aluminum), as well as by the elastic fields of adjacent Al_9Ni_2-phase layers, as when the thickness of the aluminum layers is decreased, the distance between the adjacent Al_9Ni_2-phase layers will also decrease.

While studying the microstructure of the hardened Al–Ni melt, it was found that as a result of decomposition of the oversaturated solid solution of nickel in aluminum, Al_9Ni_2-phases may precipitate in the form of plates, which are less than 30 nm thick and about 100–150 nm long [15]. Electron microscopic examinations of the morphology of Al_9Ni_2-phase, which is formed in MF in the process of its annealing, showed that in this case Al_9Ni_2-phase has a shape close to laminar one and is located mainly along the interface of the aluminum and nickel layers [7].

If we assume that Al_9Ni_2-phase is formed in MF on the boundaries between aluminum and nickel layers (Figure 4) and has a shape of plates, we can calculate the total amount of heat (Q_{teor}), which is formed by this phase transformation, proceeding from the volume of Al_9Ni_2-phase and the specific heat of its formation ΔH as:

$$Q_{theor} = Sd\rho_{Al_9Ni_2}\Delta H\frac{2d}{\lambda}, \qquad (3)$$

where S and d are the surface area and the thickness of MF, respectively; λ is the period of alternation of MF layers; $\rho_{Al_9Ni_2}$ is the density of Al_9Ni_2-phase.

Figure 5 shows a characteristic diagram of heat release, obtained by the DSC method at a continious

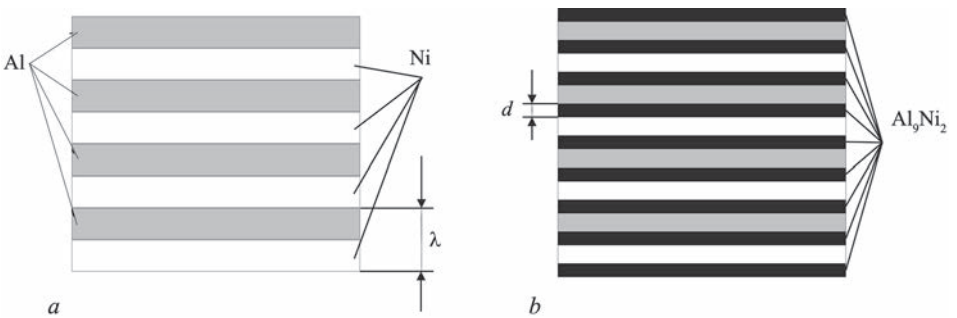

Figure 4. Scheme of microstructure of MF cross-section with the period of layers alternation λ in the initial state (*a*) and after the formation of layers of Al_9Ni_2-phase of *d* thickness (*b*)

heating of Al/Ni MF with the period of layers alternation of 110 nm and an equitatomical ratio of components. According to previously conducted studies, the first peak of heat release in the DSC diagram corresponds to the formation of Al_9Ni_2-phase. The area under the first peak (described, for example, using Gauss function) corresponds to the heat of the formation of Al_9Ni_2-phase layers.

Then the total amount of heat, released in MF at the first stage of phase transformation (Q_{exp}) during its heating, is possible to be evaluated according to DSC as:

$$Q_{exp} = ESd\rho_{MF}, \quad (4)$$

where E is the specific heat, that falls on the 1st peak of the DSC diagram (Al_9Ni_2-phase formation) during heating of MF; ρ_{MF} is the densityof MF.

Neglecting the temperature dependence of the value ΔH, which is the heat of Al_9Ni_2-phase formation in [7], let us suppose that $Q_{theor} = Q_{exp}$ and evaluate the thickness of the layer of Al_9Ni_2-phase, which is formed in the process of continuous heating of MF as:

$$d = \frac{E\rho_{MF}\lambda}{2\rho_{Al_9Ni_2}\Delta H}. \quad (5)$$

The results of the calculation of the specific value of the heat release, which falls for the 1st peak of the DSC curve, and the values of the thickness of the layer of this phase, calculated for the foils with a close chemical composition and different modulation periods, are presented in Table 1.

It is necessary to draw attention to the fact, that the thickness of Al_9Ni_2-phase layers decreases with a decrease in the thickness of aluminum layers (Figure 6). Moreover, this dependence has a significantly nonlinear nature. Thus, reducing the thickness of Al layers to 70–80 nm has almost no effect on the thickness of Al_9Ni_2-phase layers, which is about 30–35 nm, whereas at the thicknesses of the aluminum layers smaller than 70 nm, a sharp decrease in the

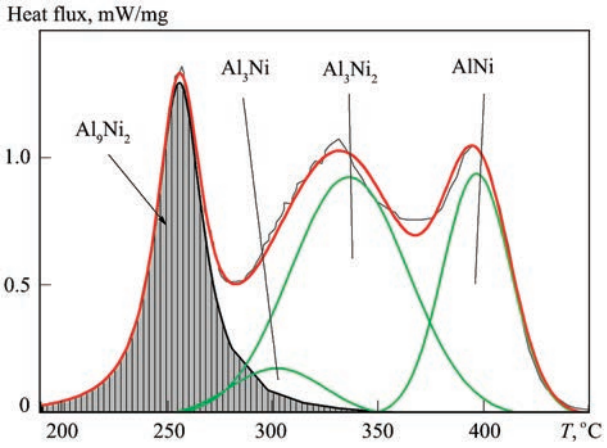

Figure 5. DSC diagram obtained during continuous heating of Al/Ni MF of equatomic composition with a period of 110 nm

thickness of Al_9Ni_2-phase layers is observed, which at the values of the thickness of the aluminum layers of about 12 nm reaches the value of the order of 2 nm. Obviously, when the thickness of aluminum layers is reduced, the distance between the adjacent Al_9Ni_2-phase layers will also decrease. In view of this, it can be assumed that when some critical value of the thicknesses of aluminum layers is reached (of the order of 10–12 nm), elastic distortions that will occur in the aluminum matrix as a result of Al_9Ni_2-phase layers formation will suppress their further growth. In the case of equatomic composition of MF, these conditions are reached during a modulation period of about 20–25 nm.

Previously, a number of studies showed that in MF with a modulation period of less than 25 nm, Al_9Ni_2-phase is not formed [7], and transformations occur under a single-channel one-stage scheme (2).

Therefore, it can be assumed that the thickness of aluminum layers can affect the sequence of phase transformations in MF during their continuous heating. If the thickness of the aluminum layer of MF is larger than some critical value, then the phase transformation will develop according to a two-channel multistage scheme (1), and if the thickness of the alu-

Table 1. Characteristics of MF microstructure and thickness of layers of Al_9Ni_2 phase formed in it during heating

Number	Chemical composition of MF, at.%	Specific heat release which falls on the 1st peak (E), J/g	Period of layers alteration, nm	Thickness, nm	
				of Al layers	of Al_9Ni_2 phase layers
1	$Al_{86.5}$–$Ni_{13.5}$	+261	266	230	37.5
2	Al_{51}–Ni_{49}	+208	200	137	34.5
3	$Al_{61.2}$–$Ni_{38.8}$	+192	135	95	27.5
4	Al_{67}–Ni_{32}	+294	140	93	33.0
5	Al_{63}–Ni_{37}	+332	110	69	29.0
6	$Al_{86.5}$–$Ni_{13.5}$	+445	63	55	14.8
7	Al_{42}–Ni_{58}	+107	106	44	10.4
8	Al_{49}–Ni_{51}	+103	26	13	2.5

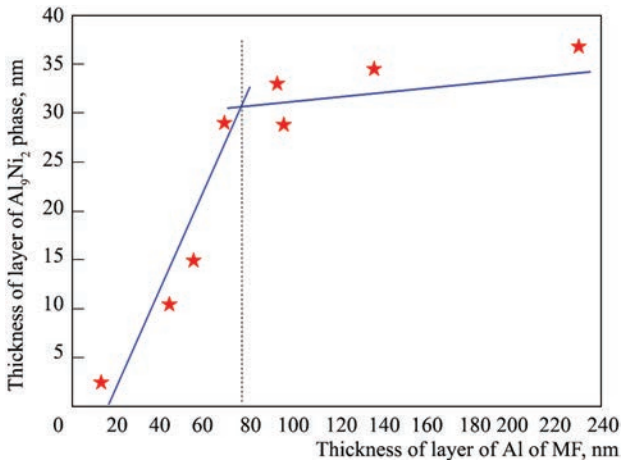

Figure 6. Dependence of thickness of the plate of Al_9Ni_2-phase formed in MF during its heating on the thickness of aluminum layers

minum layer is less than this value, it will develop according to a one-stage scheme (2).

To study the sequence of structural changes in the foils of this type, MF with the ratio of components 2Al:3Ni were produced, in which the thickness of aluminum layers was about 10 nm, which, according to the evaluation, is commesurable with a critical value. From X-ray studies it is seen (Figure 7) that during heating of MF to the temperature of 240 °C, a diffraction peak (111) from aluminum disappears. However, the diffraction peaks inherent in Al_9Ni_2-phase do not appear. Moreover, even heating to a higher temperature (300 °C) also does not lead to the appearance of diffraction signs of forming of either Al_9Ni_2-phase nor other intermetallides inherent in the mentioned system. Only heating above 300 °C is accompanied by the appearance of enlarged diffraction peaks in the positions, characteristic of AlNi phase (reaction product).

Thus, within the framework of the abovementioned model of phase transformations in MF, initiated by heating, in the case of MF with the thickness of the aluminum layer which is less than a critical one, the phase transformations develop by a single-channel one-stage scheme (1).

From the comparison of the results of X-ray-structural studies obtained in the process of continuous (slow) heating of MF with a thickness of the aluminum layer, which is less than a critical value (this work), with the results obtained in-situ at a high-rate heating of MF with the thickness of the aluminum layers greater than the critical value (in the process of developing SHS reaction front) in [8], it is possible to note the similarity of changes in diffraction patterns for both cases. Thus, in MF where the thickness of the aluminum layer is larger than a critical one (λ = 100 nm) due to a high heating rate during the SHS reaction (of the order of 10^5 °/s), the formation of Al_9Ni_2-phase is not observed, but the formation of AlNi intermetallic occurs by a single-channel one-stage scheme. Moreover, in both cases, the disappearance of diffraction peaks from aluminum is accompanied by the appearance of a wide diffuse peak (halo), which may indicate the formation of an oversaturated solid solution of nickel in aluminum, the appearance of which precedes the formation of the intermetallic phase.

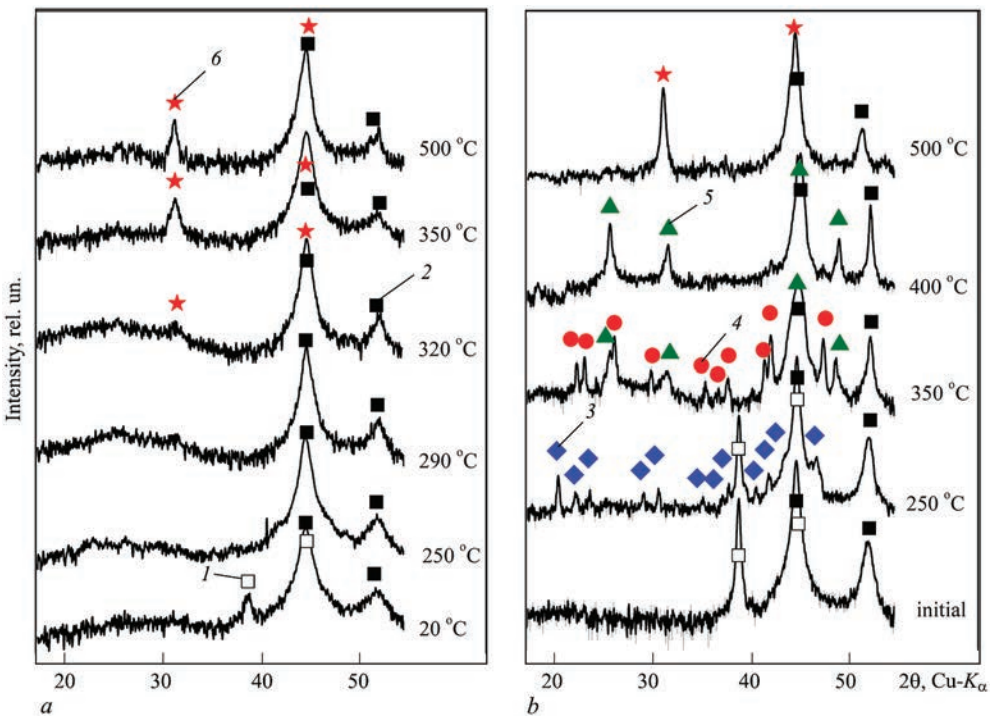

Figure 7. Diffractograms of MF with the elements ratio of 2A1:3Ni and the period of layers alternation of 25 nm (*a*) and 140 nm (*b*) in the initial state and after their heating to the temperature indicated in the pattern of temperatures: *1* — Al; *2* — Ni; *3* — Al_9Ni_2; *4* — Al_3Ni; *5* — Al_3Ni_2; *6* — AlNi

Thus, summarizing the obtained results, the patterns of developing phase transformations in Al/Ni MF can be represented in the form of a scheme shown in Figure 8. According to this scheme, the factors that affect the change in the mode of developing phase transformations from a multi-stage into a one-stage character, in the case of MF of equiatomic composition, are the period of layers alternation (thickness of the aluminum layer) and heating rate. For MF with the period of alternation of components layers smaller than 25 nm, regardless of heating rate, the phase transformation occurs by a single-channel one-stage scheme, whereas with an increase in the period of layers alternation, the realization of such a scheme is possible on the condition of high heating rates (at the level of SHS reaction or higher).

The latter is predetermined by the fact that aluminum in the initial stages is transformed into a solid solution of nickel in aluminum, which at a further increase in temperature will be transformed into an intermetallic phase inherent in this chemical composition of MF, bypassing the formation of intermediate intermetallics.

Indeed, from the kinetic diagram of Al_9Ni_2-phase formation (Figure 3), it is seen that at heating rates higher than 10^4 °C/s, the temperature of the beginning of Al_9Ni_2-phase formation becomes commeasurable with the temperature at which this phase loses its stability because, as is shown in [5], during heating of Al/Ni MF of equiatomic composition to more than 350 °C, Al_9Ni_2-phase decomposes. These model notions about the effect of heating rate on the sequence of phase transformations in MF are consistent with the results of in-situ X-ray studies of phase transformations during the SHS reaction (the rate of heating MF of the order of 10^5 °C/s), which showed that the synthesis of interametallic (reaction product) occurs without the formation of intermetallic phases [8].

CONCLUSIONS

1. For Al/Ni MF produced by the method of physical deposition (magnetron spraying or electron beam evaporation of components), the scheme of developing phase transformations (two-channel multi-stage or single-channel one-stage) is determined by the possibility of formation of the foil of a metastable Al_9Ni_2-phase in the initial stages of heating.

2. The dependence of the sequence of phase transformations on the conditions of producing MF is associated with the oversaturation of the foil with non-equilibrium vacancies that accelerate the diffusion of nickel into layers of aluminum at relatively low temperatures, which provides the formation of a solid solution of nickel in aluminum.

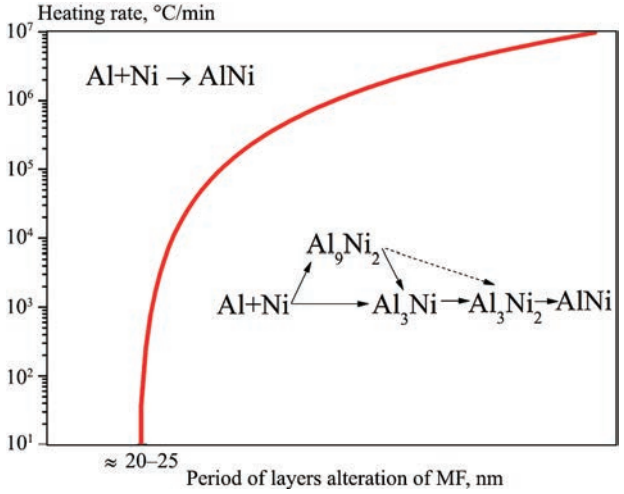

Figure 8. Scheme of effect of the modulation period of Al/Ni MF of equatomic composition on the sequence of phase transformations depending on heating rate

3. It is shown that transformation of a solid solution of nickel in aluminum into Al_9Ni_2-phase is only possible when the thickness of aluminum layers is larger than some critical value (about 10–12 nm) and the heating rate is less than 10^4 °C/s.

4. The scheme of influence of the period of layers alternation of MF and heating rate was proposed, which allows determining the scheme of realization of phase transformations initiated by heating.

REFERENCES

1. Ramos, A.S., Vieira, M.T., Simões, S. et al. (2010) Reaction-assisted diffusion bonding of advanced materials. *Defect and Diffusion Forum*, **297–301**, 972–977.
2. Duckham, A., Spey, S.J., Wang, J. et al. (2004) Reactive nanostructured foil used as a heat source for joining titanium. *J. of Applied Physics*, **96**, 2336–2342.
3. Zaporozhets, T.V., Gusak, A.M., Ustinov, A.I. (2010) SHS reactions in nanosized multilayers: Analytical model versus numerical one. *Intern. J. of Self-Propagating High-Temperature Synthesis*, 19(**4**), 227–236.
4. Grapes, M.D., LaGrange, T., Woll, K. et al. (2014) In situ transmission electron microscopy investigation of the interfacial reaction between Ni and Al during rapid heating in a nanocalorimeter. *APL Materials*, **2**, 116102-1–116102-7.
5. Ustinov, A., Demchenkov, S. (2017) Influence of metastable Al_9Ni_2 phase on the sequence of phase transformations initiated by heating of Al/Ni multilayer foils produced by EBPVD method. *Intermetallics*, **84**, 82–91.
6. Sauvage, X., Dindab, G.P., Wildeb, G. (2007) Non-equilibrium intermixing and phase transformation in severely deformed Al/Ni multilayers. *Scripta Materialia*, **56**, 181–184.
7. Blobaum, K.J., Van Heerden, D., Gavens, A.J., Weihs, T.P. (2003) Al/Ni formation reactions: Characterization of the metastable Al_9Ni_2 phase and analysis of its formation. *Acta Materialia*, **51**, 3871–3884.
8. Trenkle, J.C., Koerner, L.J., Tate, M.W. et al. (2010) Time-resolved X-ray microdiffraction studies of phase transformations during rapidly propagating reactions in Al/Ni and Zr/Ni multilayer foils. *J. of Applied Physics*, **107**, 113511.
9. Ishchenko, A.Ya., Falchenko, Yu.V., Ustinov, A.I. et al. (2007) Diffusion welding of finely-dispersed AMg5/27%Al_2O_3 com-

posite with application of nanolayered Ni/Al foil. *The Paton Welding J.*, 5(**7**), 2–5.
10. *Da Silva* Bassani, M.H., Perepezko, J.H., Edelstein, A.S., Everett, R.K. (1997) Initial phase evolution during interdiffusion reactions. *Scripta Materialia*, 37(**2**), 227–232.
11. Pasichnyy, M.O., Schmitz, G., Gusak, A.M., Vovk, V. (2005) Application of the critical concentration gradient to the nucleation of the first product phase in Co/Al thin films. *Physical Review B,* 72(**1**), 014118-1–014118-7.
12. Zhou, X.W., Johnson, R.A., Wadley, H.N.G. (1997) Vacancy formation during vapor deposition. *Acta Materialia,* 45(**11**), 4441–4452.
13. Gusak, A.M., Zaporozhets, T.V., Lyashenko, Yu.O. et al. (2010) *Diffusion-controlled solid state reactions*: *Alloys, Thin-films and Nanosystems*, Wiley-VCH, Berlin.
14. Petrantoni, M., Hémeryck, A., Ducéré, J. et al. (2010) Asymmetric diffusion as a key mechanism in Ni/Al energetic multilayer processing: A first principles study. *J. of Vacuum Sci. and Technology*, 28(**6**), 15–17.
15. Yücelen, E. (2011) *Characterization of Low-dimensional structures by Advanced Transmission Electron Microscopy*. PhD thesis, Delft University of Technology.

ORCID
A.I. Ustinov: 0000-0002-8855-3499,
S.O. Demchenkov: 0000-0002-2412-4214

CONFLICT OF INTEREST
The Authors declare no conflict of interest

CONFLICT OF INTEREST
The Authors declare no conflict of interest

CORRESPONDING AUTHOR
A.I. Ustinov
E.O. Paton Electric Welding Institute of the NASU
11 Kazymyr Malevych Str., 03150, Kyiv, Ukraine.
E-mail: ustinov3g@gmail.com

SUGGESTED CITATION
A.I. Ustinov, S.O. Demchenkov (2022) Influence of microstructure of multilayer Al/Ni foils on phase transformations initiated by heating. *The Paton Welding J.*, **4**, 43–50.

JOURNAL HOME PAGE
https://pwj.com.ua/en

Received: 24.11.2021
Accepted: 30.06.2022

https://doi.org/10.37434/tpwj2022.04.08

APPLICATION OF FRACTAL ANALYSIS IN DIAGNOSTICS OF TECHNICAL CONDITION OF METAL STRUCTURE ELEMENTS

V.V. Usov[1], M.D. Rabkina[2], N.M. Shkatulyak[1], N.I. Rybak[1], O.O. Stofel[3]

[1]K.D. Ushinskyi South-Ukraine National Pedagogical University
26 Staroportofrankivska Str., 65020, Odessa, Ukraine
[2]E.O. Paton Electric Welding Institute of the NASU
11 Kazymyr Malevych Str., 03150, Kyiv, Ukraine
[3]National Technical University of Ukraine «Igor Sikorsky Kyiv Polytechnic Institute»
37 Peremohy Ave., 03056, Kyiv, Ukraine

ABSTRACT

It is shown that fractal analysis, as an additional tool of technical diagnostics and nondestructive testing, allows determination of the most important features of the condition and behaviour of metal structure elements during their operation and failure. Examples of application of fractal dimension of the fractures are presented, in order to assess the critical dimension of brittle cracks and to determine its effect on impact toughness, yield limit, ultimate strength, and failure pressure at hydraulic testing, and to detect the interrelation of fractal dimension with fatigue life after low-cycle fatigue fracture of metal of pipeline welded joints. It is found that the nature of fractal dimensions of the fractures and diagrams of time dependence of the applied load at impact loading is due to the direction of cutting and temperature of testing the specimens. It is shown that the main component of {001} <110> texture of low-alloyed steel promotes an increase of fractal dimension of the fractures and development of brittle fracture at impact testing.

KEYWORDS: impact testing, fractal dimension, brittle crack, destruction

INTRODUCTION

Reliability of long-term application of metal structures largely depends on the approaches to determination of their technical condition, primarily, by nondestructive testing techniques. However, premature failure of structures may be due to presence of invisible defects, which promote degradation of physico-mechanical properties of the materials proper. It requires conducting mechanical testing of the specimens, in particular, on the selected samples.

Fractal analysis of the structure of metal and parts of metal structures for prediction of their failure at this stage has the role of an additional method of service life diagnostic. For instance, safe operation of oil and gas pipeline systems can be ensured, primarily, by studying the causes of pipeline failure, based on laboratory studies of base metal (BM) and metal of the characteristic zones of the welded joints (WJ).

Steel fracture is associated with such characteristics of steels as crystallographic texture, macro- and microstructure, ferrite-pearlite banding, structural component fraction, etc. [1, 2]. Experimental studies of the influence of the above structural characteristics on the regularities of elasto-plastic deformation, low-cycle fatigue fracture with involvement of physical methods of investigation (X-ray and fractographic analyses) are relevant. Therefore, the use of fractal analysis which shedying fracture surfaces is urgent [3].

The name ‘fractal’ comes from Latin “Fractus”, which means “fractional”. “broken”. When measuring the coast line length, it turned out that its length L depends on selection of measurement scale ℓ by the following relationship (in logarithmic coordinates):

$$L \infty \ell^{1-D}, \quad (1)$$

where D is the fractal dimension (FD) [4], which does not coincide with topological dimension d, is the fractional quantity and exceeds topological dimension d_i ($D > d$). For instance, for British coast line $D \approx 1.3$, and for Norwegian one $D \approx 1.5$. D value is the larger, the more rugged is the coast line [4]. It turned out that the structure of grain boundaries in metal polycrystals has a strong effect on the mechanical properties [5]. It is known that brittleness of metallic materials is often accompanied by intergranular fracture [6]. Avoiding intergranular fracture requires strengthening the grain boundaries by increasing their waviness [7]. The fractal dimension is the characteristic of grain boundary waviness.

EXPERIMENTAL PROCEDURE

DETERMINATION OF FRACTAL DIMENSION

One of the direct methods of determination of FD of two-dimensional images (microphotographs) of the

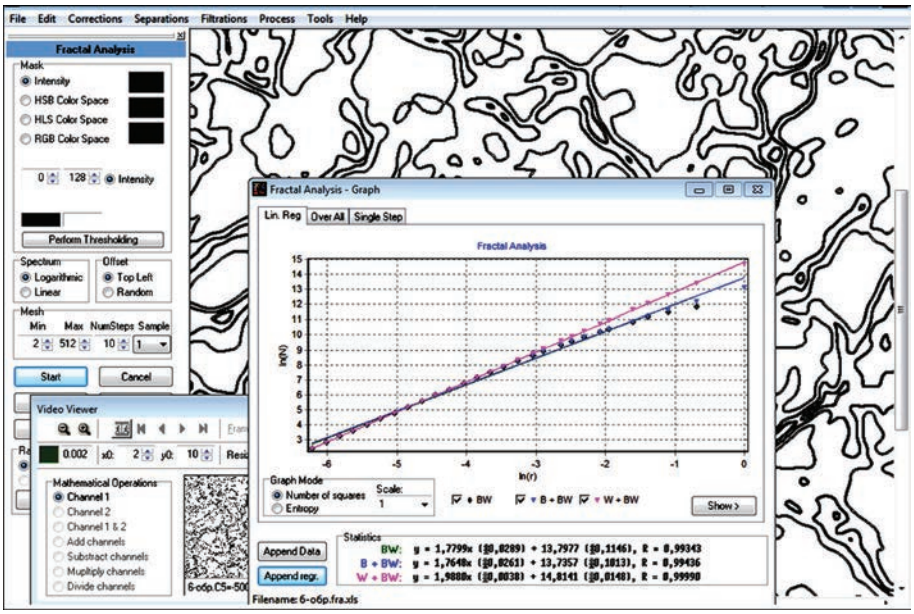

Figure 1. Example of determination of FD of a specimen of 20K grade steel after Charpy impact testing, using HarFa and ACDSee-PhotoStudioSoftware

fracture surface is the method of covering a plane curve with square grids, the dimensions of which are reduced a certain number of times (box-counting method) [8].

This method does not introduce distortions into the studied object. Here, fractal analysis of flat boundaries of fracture surface fragments is performed. A wide application of this method is due to the fact that it can be applied to any flat configuration [9]. For a mathematical fractal curve, FD coincides with Hausdorff dimension (HD). However, FD analytical calculation is rather labour-consuming and it is only possible in some cases. It is shown that fractal dimension, found using box-counting method in the case of dynamic systems, has the same values, as Hausdorff dimension [9].

In order to determine the fractal dimension, it is necessary to cover the image by elementary square grids with sides ℓ_i [9]. At each stage one and the same curve is covered by cells of a reduced scale. The smaller the square size, the more accurately is the curve reproduced. At the same time, the number of squares $N(\ell_i)$, crossed by the curve, is calculated. Then, the size of grid window ℓ_i is changed. The number of squares, crossed by the curve $N(\ell_2)$, $N(\ell_3)$ … $N(\ell_n)$. is calculated again. The number of squares $N(\ell_i)$, crossed by the curve, is related to the size of grid window ℓ_i by dependence [9]:

$$N(\ell) = \alpha^{\ell - D}, \qquad (2)$$

where $\lg N(\ell_i) = f(\lg \ell_i)$, $D = \lim\limits_{\ell \to 0} \dfrac{\lg N(\ell)}{\lg(1/\ell)}$ by definition is usually called fractal dimension or Hausdorff–Besicovich dimension [9]. Practically, D is determined by tangent of the angle of inclination of graphic dependence $\lg N(\ell_i) = f(\lg \ell_i)$ [9]. In order to determine the fractal dimension, it is convenient to apply HArFa software (Harmonic and Fractal Image Analysis), which is freely available [10]. Before determination of fractal dimension, fracture photos are usually cleared from the background, for instance, using ACDSee-PhotoStudioSoftware [11], in order to obtain only the lines of fracture fragment boundaries (Figure 1).

FRACTAL ANALYSIS OF BRITTLE FRACTURES

Fractal dimension of specimens from controlled rolled steel (Fe, 0.11 % C, 1.58 % Mn, 0.38 % Si) 20 mm thick after impact bend tests at temperatures from room to –110 °C was studied, and FD of wire from AD1 aluminium alloy after fatigue testing for symmetric bending was also determined at room temperature and at –10 °C.

Fracture surfaces were studied at the microlevel by microfractograms, obtained in scanning electron microscope REM-200 at 20000 magnification, and at the mezolevel — by optical microphotographs (MIM-7, 350 magnification).

On steel specimen fractures the fraction of the surface with brittle fracture was equal to 35 % at room temperature and 55 % at –70 °C. In aluminium fractures the "brittle" fraction increased up to 50 to 65 % at temperature lowering from 20 to –10 °C. Typical microphotograph of brittle fracture is shown in Figure 2. Fractal dimension of numbered section boundaries was determined.

It was found that the fractions after brittle fracture have average FD values of 1.20 ± 0.06 and 1.15 ± 0.06 for steel and aluminium, respectively. Proceeding from the assumption that in keeping with Griffit's cri-

terion at crack size increase by ΔR elastic energy is released, which is equal to increment of surface energy of the cut [13], the following dependence was derived for evaluation of critical dimensions of brittle cracks:

$$R^{2-D} \approx \frac{2\gamma DE}{\sigma^2}, \quad (3)$$

where E is the material modulus of elasticity, and $\gamma \approx 1$ is the specific surface energy [14].

Substitution into (3) of the data of studied steel testing at –70 °C (D_{av} = 1.2; E = 220 GPa [14], $\sigma \approx$ ≈ 100 MPa) yielded the value of critical size of fractal crack $R \approx 4.5$ μm, that corresponds to average size of cellular dislocation structure of steel [1] and agrees well with layered-brittle fracture by the mechanism of brittle transcrystalline cleavage (Figure 2).

A similar evaluation for brittle fracture of aluminium at $D_{av} \approx 1.15$, E = 70 GPa [15] and $\sigma \approx 20$ MPa (by impact toughness) yielded $R \approx 6.75$ μm.

FRACTAL DIMENSION OF GRAIN BOUNDARIES AND MECHANICAL PROPERTIES OF OXYGEN CYLINDER METAL

40 l oxygen cylinders from Dc steel (GOST 949–73) with different service life were studied at working pressure of 14.7 MPa.

Fractal dimension of grain boundaries of Dc steel of oxygen cylinders with different service life from 18 to 52 years varies from 1.10 to 1.14. Correlations of fractal dimension of grain boundaries with impact toughness, bursting pressure and yield limit with correlation coefficient R of not less than 0.80 were established (Figure 3).

Curves in Figure 3 correspond to regression equations with a high degree of correlation R:

$$KCV(-10\ ^\circ\text{C}) = (-1.14\cdot10^4 + 26.03\, D_{av}^{93.98})/(32.14 + D_{av}^{93.98}); \quad R = 0.92; \quad (4)$$

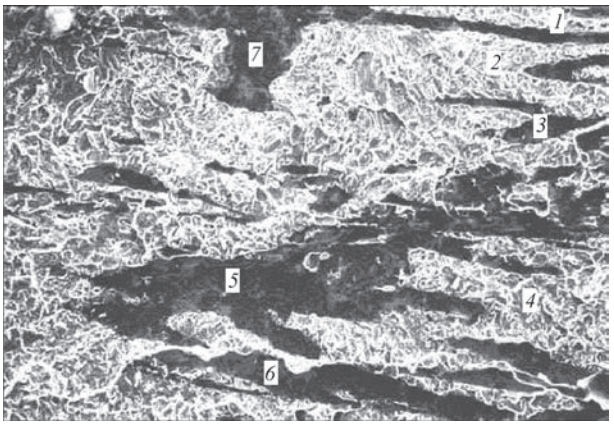

Figure 2. Electron microfractogram of layered-brittle fracture of steel after impact bend testing

$$KCV(20\ ^\circ\text{C}) = (-1.30\cdot10^5 + 38.29\, D_{av}^{164.73})/(820.64 + D_{av}^{164.73}); \quad R = 0.96; \quad (5)$$

$$P(20\ ^\circ\text{C}) = (5.34\cdot10^{-3} + 2.28\cdot10^4\, D_{av}^{184.77})/(1.10\cdot10^{-4} + D_{av}^{184.77}); \quad R = 0.80; \quad (6)$$

$$\sigma_{0.2} = (-1.53\cdot10^8 + 5.18\cdot10^2\, D_{av}^{152.92})/(8.09\cdot10^2 + D_{av}^{152.92}); \quad R = 0.80. \quad (7)$$

Correlation analysis of ultimate strength σ_t of cylinder metal indicates the absence of its connection with FD of the grain boundaries. The regression equation has the following form:

$$\sigma_t = 710.28; \quad R = 0.02. \quad (8)$$

FRACTAL FEATURES OF LOW-CYCLE FATIGUE FRACTURE (LCF) OF METAL OF PIPELINE WELDED JOINTS

Laboratory specimens for experimental determination of the main regularities of cyclic elasto-plastic deformation of base metal (BM) and metal of the characteristic welded joint zones, namely heat-affected zone (HAZ) and weld metal (WM), were cut out in the transverse direction from 530×8 mm pipe of the main pipeline from 17G1S-U steel after prolonged service

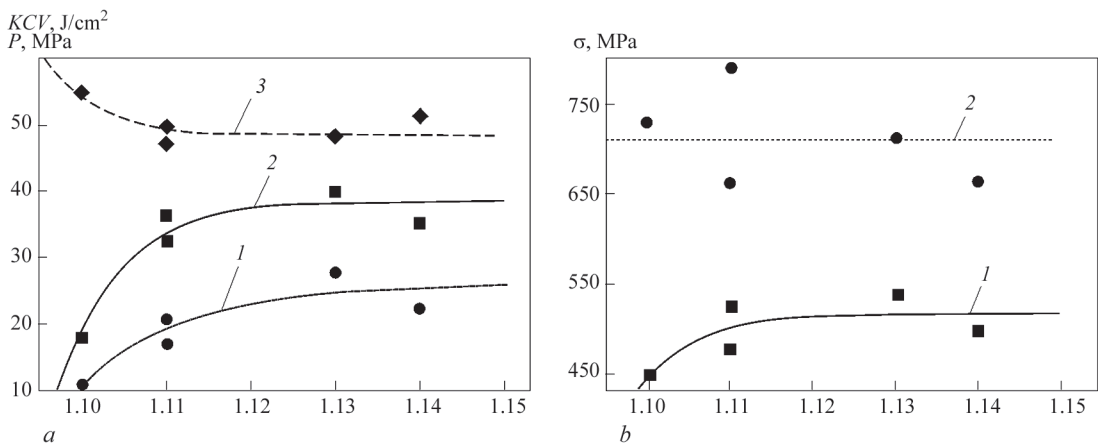

Figure 3. Correlation ties of average FD D_{av} of the grain boundaries: *a* — with *KCV* impact toughness at –10 °C (curve *1*) and 20 °C (curve *2*), bursting pressure (curve *3*); *b* — with yield limit $\sigma_{0.2}$ (curve *1*) and ultimate strength σ_t (curve *2*)

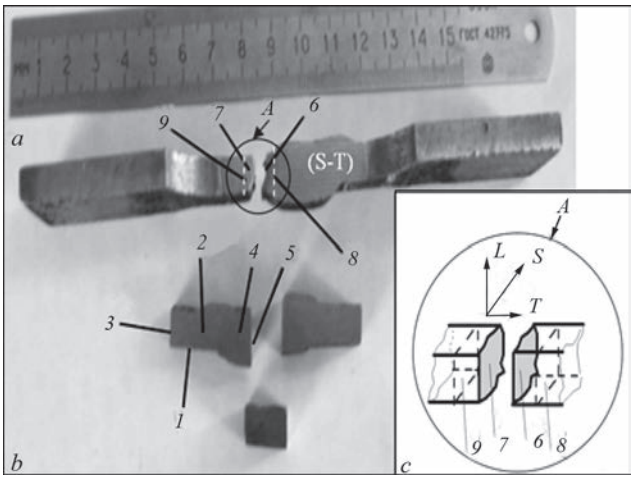

Figure 4. Studied texture sections: *a* — undeformed section (*1* — BM in *LT* rolling plane; *2*, *3* — BM in *ST* and *SL* planes; *4*, *5* — WM crossing in *ST* and *SL* planes); *b* — after fracture (*6*, *7* — bonded WM fracture surfaces; *8*, *9* — WM crossing in *SL* plane under the fractures); *c* — scheme of fragment *A* from Figure 3, *b*; *L* — longitudinal direction; *T* — transverse direction; *S* — direction, normal to *L* and *T* directions

[17]. Figure 4 presents a broken specimen after tensile testing, showing sections of the studied texture.

Figures 5–7 show the photos of fractures of the samples, BM, WM and HAZ respectively, after LCF tests. Conducted fractographic analysis revealed the differences in fracture mechanisms of the specimens cut out of BM (Figure 5) and of metal of the characteristic WJ zones after LCF tests.

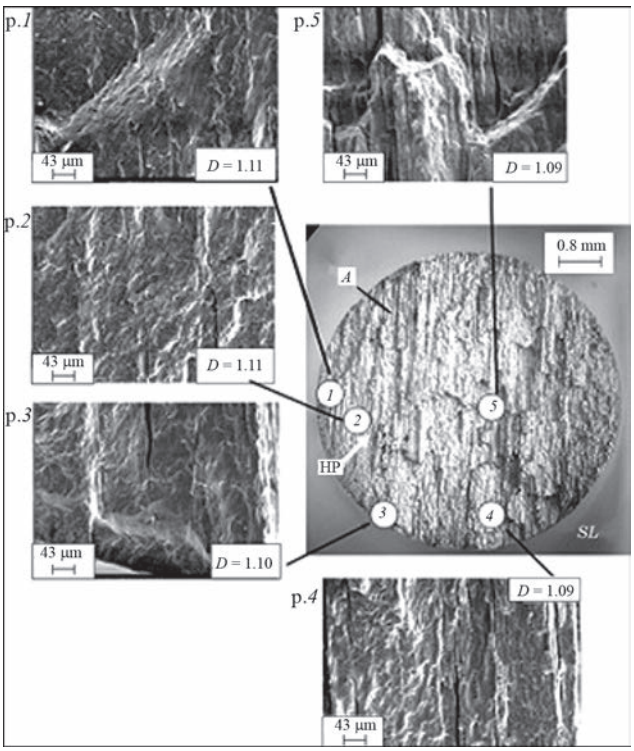

Figure 5. Fracture of BM specimen after LCF testing; *a*, *b* — view of a fragment of a broken specimen in (*L*–*T*) and (*L*–*S*) plane, respectively; *c* — fracture with typical macro- and microrelief (pp. *1*–*5*) of fracture; *HP* — fracture direction; *D* — fractal dimension

For specimens cut out of BM, quasibrittle fracture takes place with formation of secondary delamination cracks. This is promoted by BM {001} <110> crystallographic texture. Delamination can occur along the cleavage planes {001}.

Specimens, cut out of WM (Figure 6), fail by the pitting mechanism (ductile fracture). This is promoted by WM shear texture of {110} <001> type, which is the main one. It is reflected in decrease of FD value, compared to BM fracture (Figure 5).

Quasibrittle fracture is observed for HAZ specimens, but to a smaller extent, compared with BM, as a tensile-compressive crystallographic texture <001>–<110 > forms, which is due to slip deformation by {110} <110> and {110} <111> systems [17]. Here, grooved sections are observed on the HAZ microfractograms. FD value is close to its values for BM fracture specimen (Figure 5).

Figure 5 shows that the fractal dimension in different BM fracture sections changes from 1.09 to 1.11, average value of fractal dimension of base metal fracture surface was equal to $D_{av} = 1.10 \pm 0.01$. Similar results were demonstrated by analysis of fractal dimension of HAZ metal specimen. One can see from Figure 7, *c* that the fractal dimension in different HAZ fracture sections changes from 1.07 to 1.15, so that the average value of fractal dimension of fracture surface of the HAZ metal specimen was equal to $D_{av} = 1.11 \pm 0.01$.

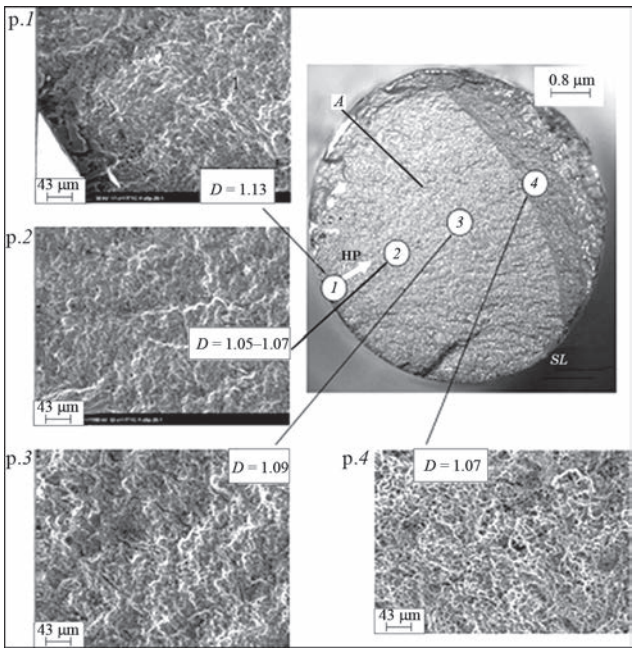

Figure 6. Fracture of a specimen from WM section after LCF testing: *a*, *b* — view of a fragment of the destroyed specimen in (*L*–*T*) and (*L*–*S*) plane, respectively; *c* — fracture with typical macro- (*A*) and microrelief (pp. *1*–*4*) of fracture; *HP* — fracture direction; *D* — fractal dimension

A more ductile fracture pattern of WM specimen follows from analysis of Figure 5 and texture. Here, fractal dimension in different sections of WM specimen fracture changed from 1.05 to 1.13 (Figure 6, *c*), and average value of WM fractal dimension was equal to $D_{av} = 1.08 \pm 0.01$.

It can be stated with 0.95 probability that the average value when taking a larger sample will not go beyond the above-mentioned ranges.

Thus, a tendency of fractal dimension increase during transition from the ductile (WM) to quasi-brittle facture pattern (BM and HAZ) is observed, that corresponds to lowering of the respective values of strength and ductility at static testing and shortening of the fatigue life. Increase of fractal dimension at quasibrittle fracture may mean that at quasiductile fracture the surface is "stretched" more due to presence of wider and deeper micropores. At the microscopic level the surface becomes smoother [18].

Increase of fractal dimension of the studied steel fractures at transition from the ductile to quasibrittle fracture agrees with the results of work [18] and other earlier studies. In [18] it is reported that the steel shows a decrease of fractal dimension at toughness increase. So, when studying [18] 24 series of specimens of AISI 4340 steel, it was shown that the fractal dimension of fracture of a steel specimen with 36 % fraction of the surface with ductile fracture was equal to $D \approx 1.28$. At increase of the ductile component fraction in the fracture to 50 % $D \approx 1.25$. At 77 % fraction of the ductile component in the fracture $D \approx 1.20$. At 100 % ductile fracture $D \approx 1.10$–1.09.

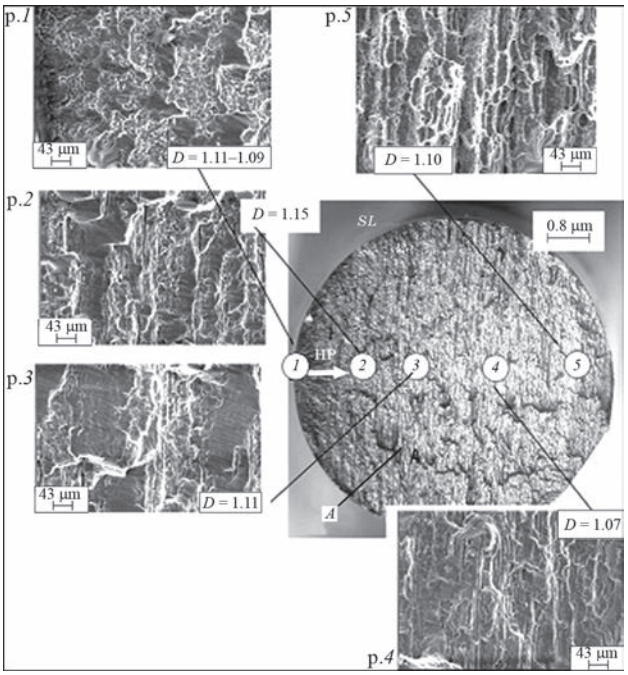

Figure 7. Fracture of a specimen from HAZ section after LCF testing: *a*, *b* — view of a fragment of broken specimen in (*L*–*T*) and (*L*–*S*) plane, respectively; *c* — fracture with typical macro- (*A*) and microrelief (pp. *1*–*5*) of fracture; *HP* — fracture direction; *D* — fractal dimension

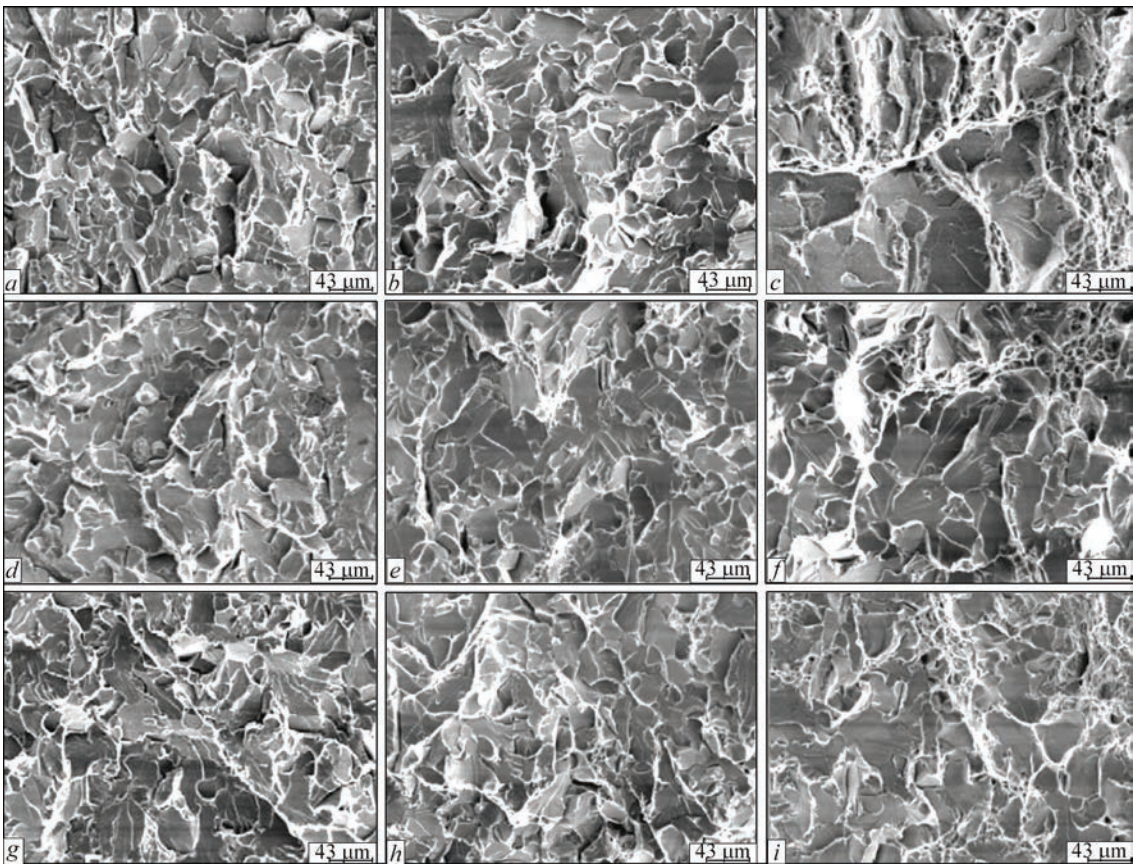

Figure 8. SEM photos of fractures after impact testing of specimens from 20 K grade steel. Scale bar length of 43 μm

Table 1. Chemical composition of metal of the studied cylinders, wt.%

Number	Service life, years	C	Mn	Si	S	P	Cr	Ni	C_{eq}
B1	45	0.513	1.01	0.319	0.023	0.023	0.14	0.11	0.72
B2	52	0.467	0.85	0.247	0.023	0.022	0.11	0.07	0.64
B3	18	0.490	0.88	0.255	0.019	0.026	0.23	0.10	0.69
B4	36	0.442	0.90	0.366	0.014	0.017	0.11	0.11	0.62
B5	49	0.482	0.72	0.257	0.026	0.019	0.10	0.08	0.63

Table 2. Fractal dimension (D_f) of fractures (Figure 8)

T, °C	LD	TD	DD	Average D_f
–50	1.59 ± 0.01	1.60 ± 0.01	1.64 ± 0.01	1.61 ± 0.01
20	1.55 ± 0.01	1.56 ± 0.01	1.59 ± 0.01	1.57 ± 0.01
50	1.52 ± 0.01	1.54 ± 0.01	1.55 ± 0.01	1.54 ± 0.01

Table 3. Fractal dimension (D_c) of P(t) diagrams (Figure 9)

T, °C	LD	TD	DD	Average D_f
–50	1.27 ± 0.01	1.23 ± 0.01	1.31 ± 0.01	1.27 ± 0.01
20	1.23 ± 0.01	1.17 ± 0.01	1.26 ± 0.01	1.22 ± 0.01
50	1.12 ± 0.01	1.13 ± 0.01	1.16 ± 0.01	1.14 ± 0.01

It should be noted that characterization of the fracture surfaces, using the above-mentioned average values of BM, HAZ and WM fractal dimensions is simplified. Presence of different values of fractal dimensions in different sections of corresponding fractures shows that the studied surfaces are multifractals, which can be interpreted as inseparable mixtures of simple fractals [17]. Each of them is characterized by its fractal dimension, and the entire respective fracture is described by an infinite set of fragments of destruction, associated with different probability of realization of different fragments in the set. Probability P_i of realization of each fragment is determined by the following relationship:

$$P_i = \ell_i^{\alpha}, \tag{9}$$

where α is the scaling parameter, $i = 1, 2, \ldots, N_n$ is the number of fragments in the set [17].

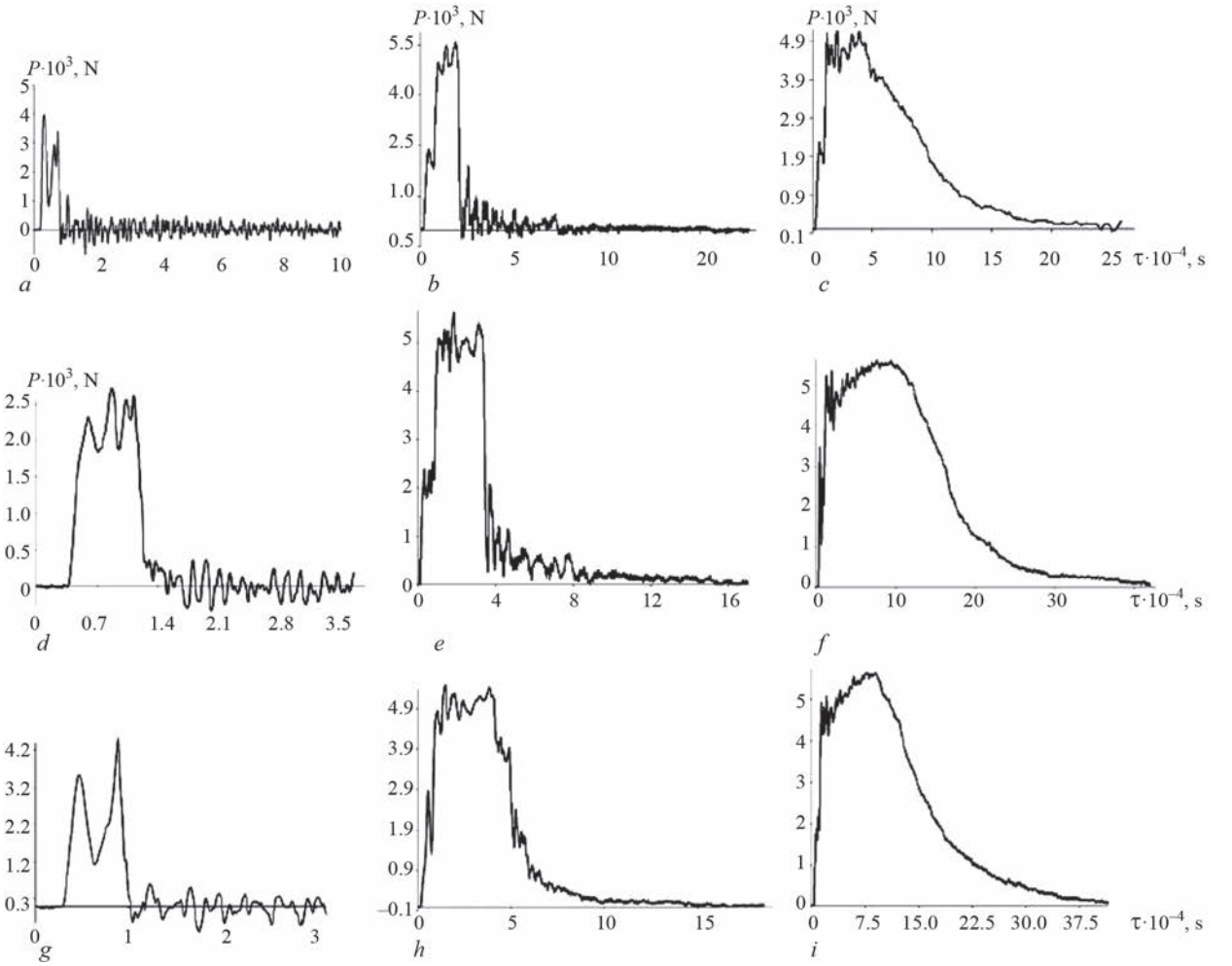

Figure 9. Diagrams of dependence of applied load P on time t at impact bend testing

Table 4. Specific fracture energy (J/m^2) at impact testing

Specimen number	–50 °C	20 °C	50 °C
Longitudinal direction LD			
1	0.83	5.04	22.87
2	0.73	4.31	20.82
Average value	0.78	4.67	21.84
Transverse direction TD			
1	0.97	9.88	47.95
2	0.95	10.91	57.95
Average value	0.96	10.39	52.95
Diagonal direction DD (LD + 45º)			
1	0.85	13.33	47.24
2	0.91	17.70	54.65
Average value	0.88	15.51	50.94

A detailed description of such fracture surfaces requires application of a multifractal approach [17, 19, 20] that may be the subject of future studies.

ANISOTROPY OF FRACTURE ENERGY AT IMPACT TESTING AND FRACTAL DIMENSION

Impact toughness parameters and fractal dimensions of load curves were determined, depending on testing time and respective fractures at impact bend testing of V-Charpy specimens, cut out in different directions from sheets of 20K steel in the temperature range from –50 to 50 °C [21]. Impact testing was conducted in a specialized vertical impact tester, fitted with a high-speed system for recording the deformations and forces [22]. Standard specimens with a V-shaped notch were cut out in three directions: longitudinal, transverse and at 45° angle to the longitudinal direction. Testing was conducted for three temperatures: –50 °C, 50 °C and room temperature, three specimens of each direction for each temperature. Test results were used to plot the diagrams of the change of the force in time $P(t)$ and the value of impact toughness was calculated by the procedure given in ISO 14556–2000 standard [23]. Figure 8 shows the microfractograms of fractures obtained in scanning electron microscope REM-200. The results of determination of fractal dimension D_f of the respective fractures are shown in Table 2. Figure 9 shows $P(t)$ diagrams of the change of the force with the time of impact bending testing of the specimens. The results of determination of fractal dimension D_c of the respective diagrams are shown in Table 3.

As one can see from Tables 2, 3 the behaviours of fractal dimensions D_f and D_c are similar. Both the FD values are maximal in the diagonal direction. Minimal values are observed at elevated testing temperature of +50 °C (Tables 2, 3).

At the same time, impact toughness at testing temperature of +50 °C is maximal (Table 4).

This is indicative of the ductile fracture pattern. Maximal values of fractal dimensions are in place at low testing temperature of –50 °C (Tables 2, 3). Impact toughness value is minimal at the same temperature (Table 1), which corresponds to brittle fracture pattern of the studied specimens at –50 °C.

Maximal values of fractal dimensions are observed for specimens, cut out in the diagonal direction (DD), i.e. FD anisotropy is in place (Tables 2, 3). This anisotropy can be caused by texture. It is found that the main component of the studied steel texture is {001} <110>. This is a typical component of rolling texture of BCC-steels [24]. In this case, crystallographic planes {001}, which are brittle cleavage planes in BCC-metals [27], are located normal to the diagonal direction. Cleavage can take place along these crystallographic planes that promotes a more brittle pattern of diagonal specimen fracture and is manifested in increase of the fractal dimension.

CONCLUSIONS

1. Configurations of brittle cracks in controlled rolled steel and AD1 aluminium are fractal, and brittle fracture shows a fractal pattern. Fractal model of the brittle crack was used to assess its critical dimensions R. For the studied steel, $R \approx 4.5$ μm, which corresponds to average size of cells of its dislocation structure. For AD1 aluminium critical size of brittle cracks is $R \approx 6.75$ μm.

2. At hydraulic testing of oxygen cylinders from Dc steel close correlation ties are in place between the fractal dimension of cylinder metal grains boundaries on the one hand, and impact toughness, bursting pressure at hydraulic testing and conditional yield limit with not lower than 0.80 correlation coefficients on the other hand. Low fractal dimension of grain boundaries corresponds to larger grain size, low values of impact toughness and yield limit, but high bursting pressure at hydraulic testing. Increase of fractal dimension of grain boundaries is accompanied by increase of im-

pact toughness, yield limit and lowering of bursting pressure. Respective correlation dependencies have the form of curves, reaching saturation with increase of fractal dimension of the boundaries. A transition from brittle transcrystalline cleavage to quasicleavage and ductile-brittle fracture pattern takes place with increase of fractal dimension.

3. Increase of the fraction of plastic deformation of the metal in the HAZ in the overall deformation amplitude at low-cycle fatigue testing of specimens of the characteristic zones of welded joint of a pipeline from 17G1S-U steel after its prolonged service leads to an essential lowering of cyclic fatigue life of the base and weld metal. There are significant differences in the fracture mechanisms: weld metal specimens fail by the pitting mechanism (ductile fracture), unlike quasibrittle fracture with formation of secondary delamination cracks, characteristic for base metal, and, to a smaller extent, for the heat-affected zone. This is accompanied by increase of average fractal dimension from 1.08 ± 0.01 for ductile fracture of the weld metal to 1.10 ± 0.01 for the base metal and to 1.11 ± 0.01 for the HAZ at quasibrittle fracture pattern. A connection can be traced between the fractal dimension of the fractures and fatigue life of the tested specimens. The fractal dimension value increases with fatigue life decrease.

4. Fractal dimensions of D_c diagram of $P(t)$ testing, which reflect the dependence of applied load P on time t, and fractal dimensions of fractures D_f after impact testing of specimens from 20K steel in the temperature range from –50 to 50 °C are of a similar nature. Maximum average values of both the fractal dimensions correspond to brittle fracture pattern and minimum impact toughness. Minimum average values of both the fractal dimensions correspond to ductile nature of fracture, and maximum impact toughness. The largest values of fractal dimension were found for specimens, cut out at 45° angle to the longitudinal direction, which are due to the influence of {001} <110> texture component, which is the main component of the low-alloyed texture of steel with BCC lattice. The presented results can be used for evaluation of the steel proneness to brittle fracture by analysis of fracture energy and fractal dimension of the diagrams of load dependence on time at impact toughness testing.

REFERENCES

1. Usov, V.V., Girenko, V.S., Rabkina, M.D. et al. (1993) Effect of the crystallographic texture on the anisotropy of fracture characteristics of control-rolled low-alloy steel. *Materials Sci.*, 29(**2**), 146–150. http://lib.gen.in/d55dae53541a8dc954b7f4d30d0a34cf.pdf
2. Lyakishev, N.P., Egiz, I.V., Shamraj, V.M. (2000) Texture and crystallographic peculiarities of fracture of steel X70 pipe material. *Metally*, **2**, 68–72 [in Russian]. http://www.imet.ac.ru/metally/nambers.htm
3. Ivanova, V.S., Balankin, A.S., Bunin, I.Zh., Oksagoev, A.A. (1994) *Synergy and fractals in materials science.* Moscow, Nauka [in Russian]. https://www.researchgate.net/publication/268999858_Sinergetika_i_fraktaly_v_materialovedenii
4. Mandelbrot, B. (2002) *Fractal geometry of nature.* Moscow, Institute for Computer Research. https://ruwapa.net/book/benua-mandelbrot-fraktalnaya-geometriya-prirody/
5. Watanabe, T., Tsurekawa, S. (2004) Toughening of brittle materials by grain boundary engineering. *Mater. Sci. Engng. A.*, **387–389**, 447–455. https://www.researchgate.net/publication/222146139_Toughening_of_Brittle_Materials_by_Grain_Boundary_Engineering
6. Vitek, V., Chen, S.P., Voter, A.F. et al. (1989) Grain boundary structure and intergranular fracture in L12 ordered alloys. *Mater. Sci. Forum,* **46**, 237–252. https://www.scientific.net/MSF.46.23
7. Watanabe, T. (1993) Grain boundary design and control for high temperature materials. *Mater. Sci. Engng. A.*, **166**, 11–28. https://www.sciencedirect.com/science/article/abs/pii/092150939390306Y
8. Zhou, H.W., Xie, H. (2003) Direct estimation of the fractal dimensions of a fracture surface of rock. *Surface Review and Letters*, 10(**5**), 751–762. https://paperzz.com/doc/9119828/direct-estimation-of-the-fractal-dimensions-of-a
9. Lucas, M.A. (2012) *Foundations of measurement fractal theory for the fracture mechanics applied. in fracture mechanics*. Edited by Alexander Belov. https://www.intechopen.com/chapters/41469
10. *Harfa: download*. http://www.fch.vut.cz/lectures/imagesci/includes/harfa_download.inc.php
11. *ACDSee Professional 2019*. https://www.acdsee.com/en/products/photo-studio-professional
12. Usov, V.V., Shkatulyak, N.M. (2005) Fractal nature of the brittle fracture surfaces of metal. *Materials Sci.*, 41(**1**), 62–66. https://www.researchgate.net/publication/226818869_Fractal_Nature_of_the_Brittle_Fracture_Surfaces_of_Metal
13. Mosolov, A.B. (1991) Fractal Griffith crack. *Zhurn. Tekh. Fiz.*, 64(**7**), 57–60 [in Russian]. http://journals.ioffe.ru/articles/viewPDF/24666
14. Honeycomb, R. (1962) *Plastic deformation of metals*. Moscow, IL [in Russian]. https://ua1lib.org/book/2433166/2721d7
15. Bernshtejn, M.L., Zajmovsky, M.A. (1979) *Mechanical properties of metals*. Moscow, Metallurgiya [in Russian]. https://ua1lib.org/book/2720875/410310
16. Usov, V.V., Rabkina, M.D., Shkatulyak, N.M., Cherneva, T.S. (2015) Fractal dimension of grain boundaries and mechanical properties of the metal of oxygen cylinder. *Material Sci.*, 50(**4**), 612–620. https://www.researchgate.net/publication/276456141_Fractal_Dimension_of_Grain_Boundaries_and_Mechanical_Properties_of_the_Metal_of_Oxygen_Cylinders
17. Usov, V.V., Gopkalo, E.E., Shkatulyak, N.M. et al. (2015) Texture, microstructure, and fractal features of the low cycle fatigue failure of the metal in pipeline welded joints. *Russian Metallurgy (Metally)*, **9**, 759–770. https://www.researchgate.net/publication/289569432_Texture_microstructure_and_fractal_features_of_the_low-cycle_fatigue_failure_of_the_metal_in_pipeline_welded_joints
18. Carney, L.R., Mecholsky, J.J. (2013) Relationship between fracture toughness and fracture surface fractal dimension in AISI 4340 steel. *Mater. Sci. Applicat*., 4(**4**), 258–267. DOI: http://dx.doi.org/10.4236/msa.2013.44032
19. Glushkov, A., Khetselius, O., Brusentseva, S., Duborez, A. (2014) Modeling chaotic dynamics of complex systems with

using chaos theory, geometric attractors, quantum neural networks. *Proc. Int. Geom. Center*, 7(**3**), 87–94, http://eprints.library.odeku.edu.ua/id/eprint/2938/1/%D0%93%D0%BB%D1%83%D0%A5%D0%B5%D1%86%D0%91%D1%80%D1%83%D0%94%D1%83%D0%B1Pmgc_2014_7_3_13%20(1).pdf
20. Glushkov, A.V., Buyadzhi, V.V., Ternovsky, V.B. et al. (2018) A chaos-dynamical approach to analysis, processing and forecasting measurements data of the chaotic quantum and laser systems and sensors. *Sensor Electronics and Microsystem Technologies*, 15(**4**) 41–49, http://eprints.library.odeku.edu.ua/id/eprint/4481/1/2018%20T15%20%234%20CEMST.pdf
21. Usov, V., Rabkina, M., Shkatulyak, N. et al. (2020) Anisotropy of Fractal Dimensions of Fractures and Loading Curves of Steel Samples During Impact Bending. *Material Sci.* 17(**4**), 142–151. http://ijmse.iust.ac.ir/article-1-1680-en.pdf
22. Kondryakov, E.A., Zhmaka, V.N., Kharchenko, V.V. et al. (2005) System of Strain and Load Measurement in Dynamic Testing of Materials. *Strength Mater.*, **37**, 331–335. https://doi.org/10.1007/s11223-005-0046-6
23. *Steel. Charpy impact V-notch test. Instrumental test method* [in Russian]. http://rossert.narod.ru/alldoc/info/2z77/g39315.html
24. (2015) *Oil and Gas Pipelines: Integrity and Safety*: Handbook. Winston R. by Ed. https://www.worldcat.org/title/oil-and-gas-pipelines-integrity-and-safety-handbook/oclc/904715784
25. Pineau, A., Benzerga, A.A., Pardoen, T. (2016) Failure of metals I: Brittle and ductile fracture. *Acta Materialia*, **107**, 424–483. https://par.nsf.gov/servlets/purl/10019128Pineau

ORCID
V.V. Usov: 0000-0001-7855-5370,
M.D. Rabkina: 0000-0003-3498-0716,
N.M. Shkatulyak: 000-0003-4905-001X,
N.I. Rybak: 0000-0003-2061-0642,
O.O. Stofel: 0000-0002-0315-5484

CONFLICT OF INTEREST
The Authors declare no conflict of interest

CORRESPONDING AUTHOR
V.V. Usov
E.O. Paton Electric Welding Institute of the NASU
11 Kazymyr Malevych Str., 03150, Kyiv, Ukraine
E-mail: valentinusov67@gmail.com

SUGGESTED CITATION
V.V. Usov, M.D. Rabkina, N.M. Shkatulyak, N.I. Rybak, O.O. Stofel (2022) Application of fractal analysis in diagnostics of technical condition of metal structure elements. *The Paton Welding J.*, **4**, 51–60.

JOURNAL HOME PAGE
https://pwj.com.ua/en

Received: 16.12.2021
Accepted: 30.06.2022

SUBSCRIPTION–2022

«The Paton Welding Journal» is Published Monthly Since 2000 in English, ISSN 0957-798X, doi.org/10.37434/tpwj.

«The Paton Welding Journal» can be also subscribed worldwide from catalogues subscription agency EBSCO.

If You are interested in making subscription directly via Editorial Board, fill, please, the coupon and send application by Fax or E-mail.

12 issues per year, back issues available.

$384, subscriptions for the printed (hard copy) version, air postage and packaging included.

$312, subscriptions for the electronic version (sending issues of Journal in pdf format or providing access to IP addresses).

Institutions with current subscriptions on printed version can purchase online access to the electronic versions of any back issues that they have not subscribed to. Issues of the Journal (more than two years old) are available at a substantially reduced price.

SUBSCRIPTION COUPON

Address for journal delivery _____

_____

Term of subscription since _____ **20** **till** _____ **20** _____

Name, initials _____

Affiliation _____

Position _____

Tel., Fax, E-mail _____

The archives for 2009–2020 are free of charge on www://patonpublishinghouse.com/eng/journals/tpwj

ADVERTISING

in «The Paton Welding Journal»

External cover, fully-colored:
First page of cover (200×200 mm) — $700
Second page of cover (200×290 mm) — $550
Third page of cover (200×290 mm) — $500
Fourth page of cover (200×290 mm) — $600

Internal cover, fully-colored:
First/second/third/fourth page (200×290 mm) — $400

Internal insert:
(200×290 mm) — $340
(400×290 mm) — $500

- Article in the form of advertising is 50 % of the cost of advertising area
- When the sum of advertising contracts exceeds $1001, a flexible system of discounts is envisaged
- Size of Journal after cutting is 200×290 mm

Address
11 Kazymyr Malevych Str. (former Bozhenko Str.), 03150, Kyiv, Ukraine
Tel.: (38044) 205 23 90
Fax: (38044) 205 23 90
E-mail: journal@paton.kiev.ua
www://patonpublishinghouse.com/eng/journals/tpwj